

Towards modeling of electron-impact ionization in warm dense matter

Dissertation
zur Erlangung des Doktorgrades
an der Fakultät für Mathematik, Informatik und
Naturwissenschaften
Fachbereich Physik
der Universität Hamburg

vorgelegt von
John Jasper Bekx

Hamburg
2020

Gutachter der Dissertation: Prof. Dr. Alexander Lichtenstein
Prof. Dr. Robin Santra

Zusammensetzung der Prüfungskommission: Prof. Dr. Alexander Lichtenstein
Prof. Dr. Daniela Pfannkuche
Prof. Dr. Robin Santra
Dr. Ulf Zastrau
Prof. Dr. Beata Ziaja-Motyka

Vorsitzende der Prüfungskommission: Prof. Dr. Daniela Pfannkuche

Datum der Disputation: 13th November 2020

Vorsitzender Fach-Promotionsausschusses PHYSIK: Prof. Dr. Günter Hans Walter Sigl

Leiter des Fachbereichs PHYSIK: Prof. Dr. Wolfgang Hansen

Dekan der Fakultät MIN: Prof. Dr. Heinrich Graener

Eidesstattliche Versicherung / Declaration on oath

Hiermit versichere ich an Eides statt, die vorliegende Dissertationsschrift selbst verfasst und keine anderen als die angegebenen Hilfsmittel und Quellen benutzt zu haben.

Die eingereichte schriftliche Fassung entspricht der auf dem elektronischen Speichermedium.

Die Dissertation wurde in der vorgelegten oder einer ähnlichen Form nicht schon einmal in einem früheren Promotionsverfahren angenommen oder als ungenügend beurteilt.

Hamburg, den

Unterschrift des Doktoranden

Abstract

The unique properties of x-ray free-electron lasers (XFELs), such as their immense brilliance, ultrashort pulse duration, and high photon energies, make XFELs an incredibly useful tool in a plethora of different scientific fields. Their applications include unique imaging techniques used in structural biology and bio-engineering, the study of new effects in nanophysics, and the creation and probing of exotic states of matter used to investigate astrophysical objects and phenomena. Due to the development of XFELs over the last few decades, there has been an increasing need to theoretically describe the x-ray-matter interactions, and subsequent radiation-induced interactions, that are prevalent in various kinds of irradiated systems. This dissertation is dedicated to the theoretical modeling of electron-impact ionization in warm dense matter (WDM). Electron-impact ionization is a predominant contributor to radiation damage induced by an XFEL pulse in dense materials.

The first part considers the process of electron-impact ionization for an isolated atom. Specifically, I consider how the cross section for this process changes for different electronic configurations of the same ion. I find that this change may be quite substantial. It depends on the charge state of the ion, the energy of the ionizing electron, and on how much the two electronic configurations being compared differ from each other.

The second part revolves around the theoretical description of warm dense matter states. I develop a novel toolkit called XCRYSTAL, which calculates electronic states present in a transient state of nonisothermal WDM from first principles. With XCRYSTAL, I calculate the electronic energies for these WDM states, which allows for predictions of the ionization potential depression caused by the presence of a dense and charged environment. In addition, I investigate the temperature dependence of the band structure of a WDM system and provide physical justifications for the observed trends.

The third and final part uses the results of the previous two parts to model electron-impact ionization in the warm dense matter states described by XCRYSTAL. Here, I develop the theory to calculate the cross section in this system and provide an in-depth discussion on its practical implementation.

Zusammenfassung

Die einzigartigen Eigenschaften von Röntgen-Freie-Elektronen-Lasern (XFELs), ihre immense Brillanz, ultrakurze Pulsdauer und hohe Photonenenergien, machen XFELs zu einem unglaublich nützlichen Werkzeug für eine Vielzahl verschiedener wissenschaftlicher Bereiche. Zu den Anwendungen gehören einzigartige Bildgebungsverfahren für die Strukturbiologie und Biotechnik, Untersuchung neuer Effekte in der Nanophysik sowie die Erzeugung und Untersuchung exotischer Materiezustände zur Erforschung astrophysikalischer Objekte und Phänomene. Durch die Entwicklung von XFELs in den letzten Jahrzehnten besteht ein zunehmender Bedarf an theoretischen Beschreibungen der Wechselwirkungen zwischen Röntgenstrahlung und Materie und den nachfolgenden strahlungsinduzierten Wechselwirkungen, die in verschiedenen Arten von bestrahlten Systemen vorherrschen. Diese Dissertation widmet sich der theoretischen Modellierung der Elektronenstoß-Ionisation in warmer, dichter Materie (WDM). Die Elektronenstoßionisation trägt hauptsächlich zu Strahlenschäden bei, die durch einen XFEL-Puls in dichten Materialien verursacht werden.

Der erste Teil befasst sich mit dem Prozess der Elektronenstoßionisation für ein isoliertes Atom. Insbesondere betrachte ich, wie sich der Querschnitt für diesen Prozess bei verschiedenen elektronischen Konfigurationen desselben Ions ändert. Es stellt sich heraus, dass diese Änderung ziemlich erheblich sein kann. Der Ladungszustand des Ions, die Energie des ionisierenden Elektrons und die spezifische elektronischen Konfigurationen ergeben hierbei unterschiedliche Stoßquerschnitte.

Der zweite Teil behandelt die theoretische Beschreibung warmer Zustände in dichter Materie. Ich beschreibe hier die Entwicklung eines neuartigen Toolkits namens XCRYSTAL, das elektronische Zustände, die in einem Übergangszustand von nichtisothermer WDM vorliegen, *ab-initio* berechnet. Mit XCRYSTAL betrachte ich die elektronischen Energien für diese WDM-Zustände, was Vorhersagen für die Verringerung des Ionisationspotentials ermöglicht, die durch das Vorhandensein einer dichten und geladenen Umgebung verursacht wird. Zusätzlich untersuche ich die Temperaturabhängigkeit der Bandstruktur eines WDM-Systems und gebe physikalische Begründungen für die beobachteten Trends.

Aufbauend auf den beiden vorangegangenen Teilen behandelt der dritte und letzte Teil die Modellierung der Ionisierung durch Elektronen in warmen Zuständen dichter Materie mittels XCRYSTAL. Ich entwickle hier eine Theorie, um den Stoßquerschnitt zu berechnen, und diskutiere dessen praktische Umsetzung.

List of publications

1. AB INITIO CALCULATION OF ELECTRON-IMPACT-IONIZATION CROSS SECTIONS FOR IONS IN EXOTIC ELECTRON CONFIGURATIONS [1]
J.J. Bekx, S.-K. Son, R. Santra, and B. Ziaja
Phys. Rev. A **98**, 022701 (2018).
2. HARD X-RAY INDUCED FAST SECONDARY ELECTRON CASCADING PROCESSES IN SOLIDS [2]
K. Mecseki, H. Höppner, M. Büscher, V. Tkachenko, N. Medvedev, J.J. Bekx, V. Lipp, P. Piekarz, M. Windeler, J.W.G. Tisch, D.J. Walke, M. Nakatsutsumi, M.J. Prandolini, J.M. Glowina, T. Sato, M. Sikorski, M. Chollet, U. Teubner, J. Robinson, S. Toleikis, B. Ziaja, and F. Tavella
Appl. Phys. Lett. **113**, 114102 (2018).
3. ELECTRONIC-STRUCTURE CALCULATIONS FOR NONISOTHERMAL WARM DENSE MATTER [3]
J.J. Bekx, S.-K. Son, B. Ziaja, and R. Santra
Phys. Rev. Res. **2**, 033061 (2020).

Contents

1	Introduction	1
2	Theory framework	5
2.1	Principle of stationary action	6
2.2	Quantum theory	9
2.2.1	First quantization and the Schrödinger equation . . .	9
2.2.2	Second quantization and quantizing the electromag- netic field	11
2.3	Many-electron system	16
2.3.1	Quantizing the electron field	17
2.3.2	Hartree-Fock-Slater equations	21
2.4	Transition rates	27
2.4.1	Time-dependent perturbation theory	27
2.4.2	Fermi's golden rule	29
2.4.3	Electron-impact ionization cross section	31
2.5	Temperature and environment	36
2.5.1	Temperature in quantum mechanics	36
2.5.2	Bloch's theorem	39
3	<i>Ab initio</i> calculation of electron-impact-ionization cross sec- tions for ions in exotic electron configurations	43
3.1	Introduction	44
3.2	Theoretical and numerical framework	46
3.2.1	xATOM toolkit	46
3.2.2	Doubly differential electron-impact-ionization cross sec- tion	47
3.2.3	Implementation of pseudocontinuum for DDCS calcu- lation	50
3.2.4	BEB and Lotz models	51
3.3	Results	53
3.3.1	Doubly and singly differential electron-impact-ionization cross section	53
3.3.2	Total electron-impact-ionization cross section	55

3.3.3	Discussion	57
3.4	Conclusion and outlook	60
4	Electronic-structure calculations for nonisothermal warm dense matter	63
4.1	Introduction	64
4.2	Methodology	66
4.2.1	Schrödinger equation for a periodic system	66
4.2.2	Hybrid basis	67
4.2.3	Calculation of atomic orbitals	71
4.2.4	Construction of the crystal potential	73
4.2.5	Electronic density at finite temperature	75
4.2.6	Self-consistent-field method	75
4.2.7	Numerical parameters for crystal calculations	76
4.3	Results	77
4.3.1	K -shell thresholds and ionization potential depression	79
4.3.2	Band structure at WDM temperatures	83
4.4	Conclusion and outlook	87
4.A	Normalization of core Bloch waves	88
4.B	Accelerating SCF convergence	90
5	Electron-impact-ionization cross section for nonisothermal warm dense matter	93
5.1	Theoretical derivation	93
5.2	Towards practical implementation	97
5.2.1	Pseudocontinuum in XCRYSTAL	98
5.2.2	Structure factor on the coarse-grained (\mathbf{Q}, ω) -grid	99
5.2.3	Optimization of the algorithm	102
5.2.4	Cross section	105
6	Summary and outlook	107

Chapter 1

Introduction

X-ray free-electron lasers (XFELs) [4–8] have the capability of providing ultrafast pulses (< 100 fs) of transversally coherent laser light in the x-ray regime ($\sim 250 - 25,000$ eV) at immense peak brilliances (up to $\sim 10^{33}$ photons/sec/mm²/mrad²/0.1% bandwidth). This is achieved by introducing a highly energetic electron bunch (~ 17.5 GeV) into an array of rapidly alternating magnetic fields, called undulators. This subsequently causes the trajectory of the electron bunch to alternately curve, thereby emitting electromagnetic radiation. The emitted radiation is made transversally coherent through the process of self-amplified spontaneous emission (SASE), whereby the electrons interact with the emitted photons [9]. Several XFEL facilities have already been established around the globe, including the LCLS [10], SACLA [11], the European XFEL [12, 13], PAL-XFEL [14], SwissFEL [15], and FLASH [16].

The applicability of XFELs is highly diverse and interdisciplinary, ranging from atomic physics to molecular biology [17–25], from nanophysics to solid-state physics [26–29], and to astrophysics [30]. The theoretical results presented in this thesis are of particular importance to two fields of XFEL applications, namely their imaging capability in the context of structural biology [31–33] and their capability to create and probe exotic states of matter [34, 35].

The imaging capability of XFELs arises from the fact that from the scattered light that is observed after irradiating some sample, the three-dimensional structure of that sample can be deduced [21–25]. For a single scatterer, such as a single biomolecule for example, the amount of scattered photons will be limited, making its structural imaging rather challenging. Two methods can be used to circumnavigate this issue. The first way is to increase the number of scatterers, albeit in a specific manner. Namely, if the scatterers are in crystalline form, the coherent diffraction from the crystal allows for an enhanced scattering signal. For example, a molecule of interest can be grown in a (nano)crystalline form and one may subsequently

irradiate numerous of these samples to obtain its molecular structure. This is the principle underlying serial-femtosecond crystallography (SFX) [31,32]. The second way is to increase the number of photons to be scattered. This is where the immense brilliance of the XFEL pulses comes into play. The ultra-intense nature of XFEL pulses negates the necessity for the use of a crystalline structure. However, the high brilliance of the pulse also causes rapidly progressing damage to occur within the sample [36,37]. Therefore, the x-ray pulse may obliterate the sample to be imaged, causing the scattered light to not accurately represent the structural information. This can, however, be remedied by the ultrafast nature of the XFEL pulse. The temporal span of the pulse is short enough to outrun radiation-induced molecular dynamics, thereby retaining the structural information in the scattered signal. However, electronic motion can not be outrun with currently available XFEL pulses [38]. Therefore, the understanding of the radiation damage induced by electronic motion, including its treatment in simulation toolkits, is crucial to achieve high-resolution structural information from experimental data [38–43].

Chapter 3 investigates the effect of electron-impact ionization in the context of imaging done by XFELs. The contribution of this process to radiation damage is significant in dense systems [37,38]. Electron-impact ionization is the process whereby an incoming electron scatters with, and ejects, a bound electron, thereby ionizing the parent atom of the latter [44–49]. In Chapter 3, we studied whether the explicit electronic configuration of an ion of a given charge state present in an imaged sample affects the electron-impact-ionization cross section. The conclusion is that the electronic configuration does indeed affect the cross section for a specific ionic charge state and this effect cannot, therefore, be simply ignored [1]. The observed trends are discussed and justified in the framework of the developed theory.

Aside from the imaging capability of XFELs, we mentioned their ability to create and probe exotic states of matter. The exotic state of matter of particular interest for this thesis is warm dense matter (WDM). Ever since its conceptual inception, warm dense matter has asserted itself as one of the most peculiar, and therefore interesting, states of matter [50]. It lies in this region of phase space where plasma physics and condensed-matter physics, and to some degree atomic physics, overlap; characterized by temperatures of the order of $T \sim 0.1 - 100$ eV and densities ranging from 10^{-3} to 10^2 g/cm³. This makes it difficult to describe theoretically as conventional methods from either plasma physics or condensed-matter physics cannot be trivially extended into this regime. All that can be done is to use ideas from these fields and gain insight with regards to their applicability to WDM. This is particularly exciting, as it gives way for creativity and innovation in the development of new theories that potentially apply to WDM. Warm dense matter is not only theoretically interesting as, on the grand scale of the Universe, it is abundantly present. After all, it is expected to be present to

some degree in nearly all stars, in other stellar bodies such as white dwarfs, and in large planets [51–55]. Warm dense matter has been created in the last century in plasma experiments, but mostly as an intermediary, and transient, product. Consider as example the experiments related to the creation of plasmas in the context of fusion [56–59]. For fusion to occur, much higher temperatures than those characterized by WDM need to be obtained, but by heating up a sample to those temperatures, one will inevitably encounter the WDM regime, even if that was not aspired. Now, with the advent of XFEL facilities, the creation of WDM has become, aside from a byproduct, also a dedicated goal [34, 35, 60–63]. To create it, to probe it, and to study it. And apart from its thermodynamical properties, also processes within this state of matter are of importance, to describe its evolution and model how these processes differ in this regime from a conventional context. The goal of this thesis has been to contribute to the advancement of our understanding of warm dense matter as well as processes therein.

Chapter 4 addresses the explicit calculation of the electronic states present in warm dense matter, which is created by irradiating a solid sample with an XFEL pulse. Despite its importance, WDM remains a particularly elusive state of matter to describe theoretically [50]. This is due to the fact that both quantum coupling effects as well as thermal effects come into play at similar magnitudes, foregoing a trivial extension of conventional condensed-matter theories at zero temperature, or of plasma theories, into the WDM regime. In Chapter 4, a specific transient nonisothermal state of WDM, with a lifetime of tens of fs, created during XFEL experiments is investigated. In this transient state, electrons are assumed to be hot, with temperatures typical for WDM conditions (10,000 – 10 million K), whereas the nuclei are assumed to remain cold and “frozen” in a lattice structure [64–70]. The electronic states in this system were calculated with a novel toolkit, XCRYSTAL [3]. Specifically, we calculated the change in ionization potentials in ions caused by the presence of a dense and charged environment as opposed to a single isolated ion. Additionally, the band structure was calculated for these systems as a function of temperature. In light of the results presented in Chapter 4, we comment on the effects of the incorporation of the explicit lattice structure, as well as the proper treatment of the so-called core orbitals.

In **Chapter 5** the topics of the previous two chapters are combined, to consider the electron-impact-ionization cross section within transient nonisothermal WDM. The WDM state will evolve beyond this transient state, progressing from the nonisothermal system considered in Chapter 4, so as to include lattice vibrations, electron-ion coupling, and eventually, nuclear interaction and dynamics [64–70]. The main catalyst inducing this evolution can be attributed to electronic processes. It is expected that the process of electron-impact ionization plays a significant role in this context. The explicit calculation of the electronic states performed by XCRYSTAL will al-

low for the first calculation of the electron-impact-ionization cross section in this WDM state from first principles. The respective theory framework developed by the author is presented, followed by an elaborate discussion on the implementation of this framework into the XCRYSTAL code.

Chapter 6 provides a summary and outlook.

Before presenting the original work of this thesis, a description of the theoretical framework that is relevant for all three parts is presented in **Chapter 2**. This chapter outlines the many-electron quantum theory that was employed, the calculation of cross sections within perturbation theory, the inclusion of temperature, and, finally, the description of electronic states in a periodic system.

Chapter 2

Theory framework

The purpose of this chapter is to introduce the theory that was used as a basis for the original work done in the upcoming Chapters 3 to 5. The framework presented in this chapter can be found in Refs. [71–77]. We will start with the general formulation of the principle of stationary action for both classical particles and fields, which will allow us to naturally define and relate Lagrangians, Lagrangian densities, Hamiltonians, and Hamiltonian densities. Having done so, we will extend this formalism into the framework of quantum mechanics, thereby introducing the use and importance of (Hermitian) operators in this framework. This will lead us into a discussion on the distinction between first and second quantization in quantum theory. Using the quantization of the electromagnetic field as an example, we will provide a general recipe for developing a quantum theory in second quantization, which will be used throughout this thesis. Subsequently, we will develop the formalism for the theoretical description of a many-electron system. This will be followed up by addressing the approximations made for its practical implementation, finally arriving at the derivation of the so-called Hartree-Fock-Slater equations. After an overview of the use of perturbation theory in the framework of quantum mechanics, we will introduce the cross section as a valuable observable and derive how it is to be calculated using the previous results for the specific example of electron-impact ionization. We will finish with a brief discussion on the incorporation of temperature and a periodic environment in this framework.

Throughout this thesis, Hartree atomic units will be employed, i.e., the electron mass m_e , the elementary charge e , and the reduced Planck constant \hbar are all set equal to 1, whereas the vacuum permittivity ε_0 is set equal to $1/4\pi$. In addition, the Boltzmann constant k_B is also set equal to 1.

2.1 Principle of stationary action

The principle of stationary action is a way to derive the equations of motions of a particular system. It is, in essence, simply a reformulation of classical Newtonian mechanics. However, it turns out that the principle of stationary action reaches far beyond the realm of classical mechanics and extends naturally into the fields of quantum mechanics and relativity. For this reason, it is an appropriate starting point of our theoretical formalism.

Consider a system with N degrees of freedom, described by the generalized coordinates $\mathbf{q} = (q_1, q_2, \dots, q_N)$. The action S is defined as

$$S = \int_{t_1}^{t_2} dt L(\mathbf{q}(t), \dot{\mathbf{q}}(t), t), \quad (2.1)$$

where $\dot{\mathbf{q}}$ defines the generalized velocities. The Lagrangian L is defined as the difference between the total kinetic energy of the system and the potential energy of the system, $L = T - V$. Considering the variation of S , we can calculate:

$$\begin{aligned} \delta S &= \int_{t_1}^{t_2} dt \delta L(\mathbf{q}(t), \dot{\mathbf{q}}(t), t) \\ &= \int_{t_1}^{t_2} dt \sum_{i=1}^N \left(\frac{\partial L}{\partial q_i} \delta q_i + \frac{\partial L}{\partial \dot{q}_i} \delta \dot{q}_i \right) \\ &= \sum_{i=1}^N \int_{t_1}^{t_2} dt \left[\frac{\partial L}{\partial q_i} \delta q_i + \frac{\partial L}{\partial \dot{q}_i} \frac{d(\delta q_i)}{dt} \right] \\ &= \sum_{i=1}^N \left\{ \int_{t_1}^{t_2} dt \frac{d}{dt} \left(\frac{\partial L}{\partial \dot{q}_i} \delta q_i \right) + \int_{t_1}^{t_2} dt \left[\frac{\partial L}{\partial q_i} \delta q_i - \frac{d}{dt} \left(\frac{\partial L}{\partial \dot{q}_i} \right) \delta q_i \right] \right\} \\ &= \sum_{i=1}^N \left\{ \left[\frac{\partial L}{\partial \dot{q}_i} \delta q_i \right]_{t_1}^{t_2} + \int_{t_1}^{t_2} dt \left(\frac{\partial L}{\partial q_i} - \frac{d}{dt} \frac{\partial L}{\partial \dot{q}_i} \right) \delta q_i \right\}. \end{aligned} \quad (2.2)$$

If we assume the initial and final points in configuration space, $\mathbf{q}(t_1)$ and $\mathbf{q}(t_2)$, to be fixed, such that their variations are zero, the first term vanishes. Imposing the principle of stationary action implies that we take the variation of S to be zero, thus setting $\delta S = 0$, which recovers the Euler-Lagrange (E-L) equations for the equations of motion:

$$\frac{\partial L}{\partial q_i} - \frac{d}{dt} \frac{\partial L}{\partial \dot{q}_i} = 0, \quad \text{for } i = 1, \dots, N. \quad (2.3)$$

We can show this is equivalent to Newton's second law of motion by considering the Lagrangian

$$L = \sum_{i=1}^N \frac{1}{2} m_i \dot{\mathbf{x}}_i^2 - V(\mathbf{x}_1, \mathbf{x}_2, \dots, \mathbf{x}_N), \quad (2.4)$$

with m_i , \mathbf{x}_i , and $\dot{\mathbf{x}}_i$ the mass, position, and velocity of the i -th particle, respectively. Plugging this into Eq. (2.3) immediately yields:

$$-\nabla V(\mathbf{x}_1, \mathbf{x}_2, \dots, \mathbf{x}_N) - \sum_{i=1}^N m_i \ddot{\mathbf{x}}_i = 0. \quad (2.5)$$

Defining the force, $\mathbf{F} = -\nabla V$, we recover Newton's second law of motion. This last connection between the force and the potential is valid for conservative forces, i.e., forces that result in the work done to move a particle between two points being independent of the path taken. All interactions considered in this thesis result in conservative forces.

We define the generalized (canonical) momentum conjugate to coordinate q_i as

$$p_i = \frac{\partial L}{\partial \dot{q}_i}. \quad (2.6)$$

This is a natural choice as we know from Noether's theorem that an invariance with respect to a coordinate q_i leads to the conservation of momentum, which follows immediately from Eq. (2.3), by plugging in the definition of p_i [Eq. (2.6)] and setting $\partial L / \partial q_i = 0$. The conventional form for the total momentum, $\mathbf{p} = \sum_{i=1}^N m_i \dot{\mathbf{x}}_i$, can be recovered using this definition in conjunction with the Lagrangian in Eq. (2.4). The Hamiltonian, H , is defined via a Legendre transformation of the Lagrangian

$$H = H(\mathbf{q}, \mathbf{p}, t) = \dot{\mathbf{q}} \cdot \mathbf{p} - L, \quad (2.7)$$

and is a constant of the motion if the Lagrangian is not explicitly dependent on time. This can be shown by considering

$$\begin{aligned} dH &= \sum_i \left(\frac{\partial H}{\partial q_i} dq_i + \frac{\partial H}{\partial p_i} dp_i \right) + \frac{\partial H}{\partial t} dt \\ &= d \left(\sum_i \dot{q}_i p_i - L \right) \\ &= \sum_i \left(-\frac{\partial L}{\partial q_i} dq_i + \dot{q}_i dp_i \right) - \frac{\partial L}{\partial t} dt, \end{aligned} \quad (2.8)$$

from which we can read off

$$\frac{\partial H}{\partial q_i} = -\dot{p}_i \quad \frac{\partial H}{\partial p_i} = \dot{q}_i \quad \frac{\partial H}{\partial t} = -\frac{\partial L}{\partial t}. \quad (2.9)$$

In all cases considered in this thesis, the Hamiltonian represents the total energy $T + V$ of the system. Furthermore, we will not be considering explicit time dependence in Lagrangians throughout this work, and will omit it henceforth.

We can extend this framework to include an infinite number of degrees of freedom, i.e., going from a discrete number of generalized coordinates to using continuous (vector-)fields $\mathbf{A}(\mathbf{x}, t)$. The Lagrangian L can (often) be written as a volume integral over a Lagrangian density, \mathcal{L} :

$$L = \int d^3x \mathcal{L}(\mathbf{A}, \partial_j A_i, \partial_t A_i), \quad (2.10)$$

where $\partial_j \equiv \partial/\partial x_j$ and $\partial_t \equiv \partial/\partial t$. Same as before, we obtain the equations of motion by setting $\delta S = 0$, yielding:

$$\delta S = \int_{t_1}^{t_2} dt \int d^3x \delta \mathcal{L}(\mathbf{A}, \partial_j A_i, \partial_t A_i) = 0, \quad (2.11)$$

where

$$\delta \mathcal{L} = \sum_i \left[\frac{\partial \mathcal{L}}{\partial A_i} \delta A_i + \sum_j \frac{\partial \mathcal{L}}{\partial(\partial_j A_i)} \frac{\partial(\delta A_i)}{\partial x_j} + \frac{\partial \mathcal{L}}{\partial(\partial_t A_i)} \frac{\partial(\delta A_i)}{\partial t} \right]. \quad (2.12)$$

Imposing similar conditions as before, $\delta A_i(t_1) = 0$ and $\delta A_i(t_2) = 0$, and imposing the additional condition that $\delta A_i \rightarrow 0$ as $\mathbf{x} \rightarrow \infty$ for all times, we may again perform an integration by parts resulting in

$$\frac{\partial}{\partial t} \frac{\partial \mathcal{L}}{\partial(\partial_t A_i)} + \sum_j \frac{\partial}{\partial x_j} \frac{\partial \mathcal{L}}{\partial(\partial_j A_i)} - \frac{\partial \mathcal{L}}{\partial A_i} = 0. \quad (2.13)$$

Analogous to before, we may define a canonical momentum density field $\mathbf{\Pi}(\mathbf{x}, t)$ with components

$$\Pi_i = \frac{\partial \mathcal{L}}{\partial(\partial_t A_i)}, \quad (2.14)$$

and a Hamiltonian H in terms of a Hamiltonian density \mathcal{H}

$$H = \int d^3x \mathcal{H}, \quad \text{with} \quad \mathcal{H} = (\partial_t \mathbf{A}) \cdot \mathbf{\Pi} - \mathcal{L}. \quad (2.15)$$

The purpose of this section was to show that all that is needed to determine the equations of motion of a system is either the Hamiltonian or the Lagrangian (only one is desired as the other is connected via a Legendre transformation). From them, an action S can be constructed and the equations of motion can be derived by imposing that this action is stationary, $\delta S = 0$. In addition, the Hamiltonian represents the total energy of the system considered.

2.2 Quantum theory

To develop a quantum-mechanical framework, one has the choice of employing one of two schemes: first quantization or second quantization. First and second quantization lie at the heart of the wave-particle duality in quantum mechanics. In simple terms, first quantization refers to the fact that particles behave like waves and second quantization to the fact that waves exhibit particle-like behaviour [73]. Examples are, for instance, electrons being described with the Schrödinger equation, which is a wave equation, or electromagnetic waves being described by photons, and vibrations in a lattice by phonons. In this section, we will elaborate on first and second quantization and use it to extend the classical formalism of Sec. 2.1 into the microscopic quantum world.

2.2.1 First quantization and the Schrödinger equation

To introduce first quantization, consider a particle in one dimension. Conventionally, one may describe this particle using quantities such as its position x and its velocity $v \equiv \dot{x}$ at any given moment in time. We disembark from this in the quantum realm and instead describe the particle with a complex-valued probability-amplitude function $\Psi(x, t)$, that obeys a wave equation

$$i\frac{\partial\Psi}{\partial t} = -\frac{1}{2m}\frac{\partial^2\Psi}{\partial x^2} + V\Psi, \quad (2.16)$$

where m is the mass of the particle and V is the external potential. Admittedly, this is quite an assumption to make. Why should we care about a probability function, why would it be complex, and why would it follow a wave equation? Unfortunately, the historical development of quantum mechanics is such that theory and experiment walked hand in hand together very closely, depending on each other for guidance. As such, the consensus that they reached is utterly unintuitive and pedagogically difficult to justify. However, guided by experiment, we may take it as an ansatz and be assured that it works.

Like any probability amplitude, $\Psi(x, t)$ is normalized to one

$$\int_{-\infty}^{\infty} dx |\Psi(x, t)|^2 = 1, \quad (2.17)$$

which imposes $\Psi(x, t) \rightarrow 0$ as $x \rightarrow \infty$. This defines the probability-density function associated to the particle at the space-time point (x, t) as $|\Psi(x, t)|^2$. In addition, it defines the wave functions $\Psi(x, t)$ as vectors in a complex L^2 -Hilbert space with an inner product defined as

$$\langle\Psi|\Phi\rangle = \int_{-\infty}^{\infty} dx \Psi^\dagger(x, t)\Phi(x, t), \quad (2.18)$$

for two vectors $|\Psi\rangle$ and $|\Phi\rangle$ in this L^2 -Hilbert space. As a probability amplitude, $\Psi(x, t)$ shares the interpretation that if one wants to know the expectation value of an observable quantity, such as x , it is calculated as:

$$\langle x \rangle = \int_{-\infty}^{\infty} dx \Psi^\dagger x \Psi. \quad (2.19)$$

One can proceed by considering the expectation value of the particle's velocity. Using Eq. (2.16), it follows that

$$\begin{aligned} \frac{d\langle x \rangle}{dt} &= \int dx x \frac{\partial}{\partial t} |\Psi|^2 \\ &= \frac{i}{2m} \int dx x \frac{\partial}{\partial x} \left(\Psi^\dagger \frac{\partial \Psi}{\partial x} - \frac{\partial \Psi^\dagger}{\partial x} \Psi \right) \\ &= \frac{-i}{m} \int dx \Psi^\dagger \frac{\partial \Psi}{\partial x}, \end{aligned} \quad (2.20)$$

from which we can find the momentum $p = md\langle x \rangle/dt$. Together

$$\begin{aligned} \langle x \rangle &= \int_{-\infty}^{\infty} \Psi^\dagger [x] \Psi & p &= \int dx \Psi^\dagger \left[-i \frac{\partial}{\partial x} \right] \Psi, \\ &= \int_{-\infty}^{\infty} \Psi^\dagger [\hat{x}] \Psi & &= \int dx \Psi^\dagger [\hat{p}] \Psi \end{aligned} \quad (2.21)$$

The point of this exercise was to show that we can reformulate the determination of certain quantities x and p into the determination of the expectation values of suitable *operators* $\hat{x} = x$ and $\hat{p} = -i\partial/\partial x$. In general, an observable O is represented by a Hermitian operator, \hat{O} , where its expectation value is calculated as $\langle \hat{O} \rangle = \langle \Psi | \hat{O} | \Psi \rangle = \int dx \Psi^\dagger \hat{O} \Psi$. This operator must be Hermitian to ensure that its expectation value is real. A key property that operators possess is the fact that they do not generally commute. Acting with $\hat{x}\hat{p} - \hat{p}\hat{x} = [\hat{x}, \hat{p}]$ on some test function f reveals that $[\hat{x}, \hat{p}] = i$. This representation of physical quantities as operators is referred to as *first quantization*. It turns out that promoting quantities to be operators that satisfy certain commutation relations is a general recipe to extend a classical theory into a quantum theory. For the general system of N particles developed in Sec. 2.1 this amounts to

$$[\hat{q}_i, \hat{q}_j] = [\hat{p}_i, \hat{p}_j] = 0, \quad \text{and} \quad [\hat{q}_i, \hat{p}_j] = i\delta_{ij}. \quad (2.22)$$

The fact that we may describe (the properties of) particles by using a probability amplitude $\Psi(\mathbf{x}, t)$ (with \mathbf{x} being the three-dimensional position vector) which obeys a wave equation of the form

$$i \frac{\partial \Psi}{\partial t} = -\frac{1}{2m} \nabla^2 \Psi + V \Psi \equiv \hat{H} \Psi, \quad (2.23)$$

reveals one direction of the wave-particle duality. As a quick note, if we factor out the time-dependence of $\Psi(\mathbf{x}, t)$ as $\Psi(\mathbf{x}, t) = \psi(\mathbf{x})e^{-i\hat{H}t} = \psi(\mathbf{x})e^{-iEt}$, where ψ and E are eigenfunctions and eigenvalues of the Hamiltonian \hat{H} , we arrive at the time-independent Schrödinger equation:

$$-\frac{1}{2m}\nabla^2\psi(\mathbf{x}) + V\psi(\mathbf{x}) \equiv \hat{H}\psi(\mathbf{x}) = E\psi(\mathbf{x}), \quad (2.24)$$

which identifies E as the energy of the particle considered. It turns out that any solution to the time-dependent Schrödinger equation, $\Psi(\mathbf{x}, t)$, may be written as a linear combination of $\psi_n(\mathbf{x})e^{-iE_nt}$, with $\{\psi_n, E_n\}$, $n \in \mathbb{N}$, one of infinite solutions of Eq. (2.24) [72]. We will return to the inclusion of time in Sec. 2.4.1. When describing more than one particle, say N of them, $\Psi = \Psi(\mathbf{x}_1, \mathbf{x}_2, \dots, \mathbf{x}_N, t)$, and in Eqs. (2.23) and (2.24) ∇^2 must be replaced by $\sum_i \nabla_i^2$, $i \in \{1, \dots, N\}$.

2.2.2 Second quantization and quantizing the electromagnetic field

The first quantization scheme works fine for systems where the number of particles N is fixed. However, there are numerous scenarios where one may be interested in changing the number of particles present in the system. The system with a particle added or removed would have to be described by a new wave function. Thus, having gone through the arduous task of solving for $\Psi(\mathbf{x}_1, \mathbf{x}_2, \dots, \mathbf{x}_N, t)$, we could have an interaction occur, thereby changing the number of particles, and having to solve for a new wave function $\Psi'(\mathbf{x}_1, \mathbf{x}_2, \dots, \mathbf{x}_{N'}, t)$, with $N \neq N'$, all over again. To remedy this, one performs the process of quantization on the fields that describe your system, rather than directly on observable quantities. The quantization of fields leads to the concept of a *quantum field*. For the vector fields considered in Sec. 2.1, this amounts to:

$$\begin{aligned} [\hat{A}_i(\mathbf{x}), \hat{A}_j(\mathbf{x}')] &= [\hat{\Pi}_i(\mathbf{x}), \hat{\Pi}_j(\mathbf{x}')] = 0 \\ [\hat{A}_i(\mathbf{x}), \hat{\Pi}_j(\mathbf{x}')] &= i\delta_{ij}\delta(\mathbf{x} - \mathbf{x}'). \end{aligned} \quad (2.25)$$

As such, the normal modes of the (now quantum) field, after defining some basis to represent it in, become quantized. These discrete excitations that comprise the quantum field are interpreted as particles. This solves the issue of changing the number of particles N , since we only need to consider different quantized modes to change this number. Having particles pop up in this way from quantized fields in second quantization reveals the other direction of the wave-particle duality. Even though this last paragraph phrases the essence behind second quantization, it is not very informative without an explicit example. Therefore, as we will be working in second quantization in this thesis, and to better illustrate the aforementioned concepts, let us work out the example of quantizing the electromagnetic field.

A classical electromagnetic field is described by Maxwell's equations, presented here in Gaussian units

$$\nabla \cdot \mathbf{E} = 4\pi\rho, \quad (2.26a)$$

$$\nabla \cdot \mathbf{B} = 0, \quad (2.26b)$$

$$\nabla \times \mathbf{E} = -\frac{1}{c} \frac{\partial \mathbf{B}}{\partial t}, \quad (2.26c)$$

$$\nabla \times \mathbf{B} = \frac{4\pi}{c} \mathbf{J} + \frac{1}{c} \frac{\partial \mathbf{E}}{\partial t}, \quad (2.26d)$$

with \mathbf{E} and \mathbf{B} denoting the electric and magnetic field, respectively, and ρ and \mathbf{J} being the charge density and charge density current that arise from the present charged particles. They are given by:

$$\rho(\mathbf{x}, t) = \sum_n e_n \delta(\mathbf{x} - \mathbf{q}_n(t)), \quad (2.27a)$$

$$\mathbf{J}(\mathbf{x}, t) = \sum_n e_n \dot{\mathbf{q}}_n(t) \delta(\mathbf{x} - \mathbf{q}_n(t)), \quad (2.27b)$$

with e_n being the charge of the n -th particle, and $\mathbf{q}_n(t)$ and $\dot{\mathbf{q}}_n(t)$ its respective position and velocity. The equations of motion for the particles stem from coupling them to \mathbf{E} and \mathbf{B} through the Lorentz force

$$m_n \ddot{\mathbf{q}}_n(t) = e_n \left(\mathbf{E} + \frac{1}{c} \dot{\mathbf{q}}_n(t) \times \mathbf{B} \right), \quad (2.28)$$

with m_n being the mass of the n -th particle. From Eqs. (2.26a)-(2.26d), we can obtain solutions for \mathbf{E} and \mathbf{B} in terms of the scalar and vector potentials Φ and \mathbf{A} , which are

$$\mathbf{E} = -\nabla\Phi - \frac{1}{c} \frac{\partial \mathbf{A}}{\partial t}, \quad (2.29)$$

$$\mathbf{B} = \nabla \times \mathbf{A}. \quad (2.30)$$

They remain invariant under the following transformation

$$\Phi \Rightarrow \Phi' = \Phi - \frac{1}{c} \frac{\partial \lambda}{\partial t}, \quad (2.31)$$

$$\mathbf{A} \Rightarrow \mathbf{A}' = \mathbf{A} + \nabla\lambda, \quad (2.32)$$

where $\lambda(\mathbf{x}, t)$ is any real scalar function. This transformation is called a gauge transformation. As Φ and \mathbf{A} , and in turn also \mathbf{E} and \mathbf{B} , remain invariant under a gauge transformation, physical results should not depend on the function $\lambda(\mathbf{x}, t)$. This thus provides an extra degree of freedom and it is common to use this advantageously by imposing a particular restriction on either Φ or \mathbf{A} with the goal of simplifying computations. The gauge choice we will employ is the Coulomb gauge, $\nabla \cdot \mathbf{A} = 0$. Note that the scalar

potential provides no new information, as it can be related to the charge density via Poisson's equation:

$$\nabla^2 \Phi = -4\pi\rho, \quad \implies \quad \Phi(\mathbf{x}, t) = \int d^3x' \frac{\rho(\mathbf{x}', t)}{|\mathbf{x} - \mathbf{x}'|}. \quad (2.33)$$

Thus, the electromagnetic field itself is characterized solely by the vector potential $\mathbf{A}(\mathbf{x}, t)$. Its equation of motion can be derived from Eqs. (2.26a)-(2.26d) and takes the form of a wave equation:

$$\left(\frac{1}{c^2} \frac{\partial^2}{\partial t^2} - \nabla^2 \right) \mathbf{A} = \frac{4\pi}{c} \mathbf{J}. \quad (2.34)$$

We will proceed by only considering the free electromagnetic field, i.e., setting ρ and \mathbf{J} equal to zero. We wish to find a Lagrangian density that recovers the equation of motion for $\mathbf{A}(\mathbf{x}, t)$ [Eq. (2.34) with $\mathbf{J} = 0$], such that we may identify the Hamiltonian and the canonically conjugate momentum $\mathbf{\Pi}(\mathbf{x}, t)$, as was explained in Sec. 2.1, thereby identifying what the canonically conjugate fields are that we wish to quantize.

The free electromagnetic field can be fully described by the Lagrangian density

$$\mathcal{L}_{\text{rad}} = \frac{1}{8\pi} \left[\frac{1}{c^2} \dot{\mathbf{A}}^2 - (\nabla \times \mathbf{A})^2 \right], \quad (2.35)$$

where $\dot{\mathbf{A}} \equiv \partial_t \mathbf{A}$. This Lagrangian density leads to the correct equation of motion for \mathbf{A} as

$$\frac{\partial}{\partial t} \frac{\partial \mathcal{L}_{\text{rad}}}{\partial (\partial_t A_i)} = \frac{1}{4\pi c^2} \frac{\partial^2 A_i}{\partial t^2} \quad (2.36a)$$

$$\sum_j \frac{\partial}{\partial x_j} \frac{\partial \mathcal{L}_{\text{rad}}}{\partial (\partial_j A_i)} = -\frac{1}{4\pi} \nabla^2 A_i \quad (2.36b)$$

$$\frac{\partial \mathcal{L}_{\text{rad}}}{\partial A_i} = 0, \quad (2.36c)$$

which can be used in the E-L equations to arrive at Eq. (2.34) with $\mathbf{J} = 0$. Having defined a Lagrangian density, we can find the canonical momentum conjugate to $\mathbf{A}(\mathbf{x}, t)$ using Eq (2.14)

$$\mathbf{\Pi}(\mathbf{x}, t) = \frac{\partial \mathcal{L}_{\text{rad}}}{\partial \dot{\mathbf{A}}} = \frac{1}{4\pi c^2} \dot{\mathbf{A}}, \quad (2.37)$$

as well as the Hamiltonian density through Eq. (2.15)

$$\mathcal{H}_{\text{rad}} = \frac{1}{8\pi} \left[(4\pi c \mathbf{\Pi})^2 + (\nabla \times \mathbf{A})^2 \right]. \quad (2.38)$$

To quantize the electromagnetic field, we simply promote \mathbf{A} and $\mathbf{\Pi}$ to operators $\hat{\mathbf{A}}$ and $\hat{\mathbf{\Pi}}$ and impose they satisfy the commutation relations in Eq. (2.25).

To show how this leads to particle-like behavior, we decompose the vector field $\mathbf{A}(\mathbf{x}, t)$ into a basis of plane waves. Since $\mathbf{A}(\mathbf{x}, t)$ satisfies a wave equation, plane waves form a natural choice for a basis. The mode expansion is

$$\begin{aligned}\mathbf{A}(\mathbf{x}, t) &= \sum_{\mathbf{k}, \lambda} \sqrt{\frac{2\pi c^2}{V\omega_{\mathbf{k}}}} \left[a_{\mathbf{k}, \lambda} \boldsymbol{\epsilon}_{\mathbf{k}, \lambda} e^{i(\mathbf{k} \cdot \mathbf{x} - \omega_{\mathbf{k}} t)} + a_{\mathbf{k}, \lambda}^\dagger \boldsymbol{\epsilon}_{\mathbf{k}, \lambda}^* e^{-i(\mathbf{k} \cdot \mathbf{x} - \omega_{\mathbf{k}} t)} \right] \\ &= \sum_{\mathbf{k}, \lambda} \sqrt{\frac{2\pi c^2}{V\omega_{\mathbf{k}}}} \left[a_{\mathbf{k}, \lambda} \boldsymbol{\epsilon}_{\mathbf{k}, \lambda} e^{i(\mathbf{k} \cdot \mathbf{x} - \omega_{\mathbf{k}} t)} + c.c. \right],\end{aligned}\quad (2.39)$$

where “c.c.” stands for the complex conjugate of the first term in the square brackets, $\omega_{\mathbf{k}} = c|\mathbf{k}|$ and the volume V is introduced to impose periodic boundary conditions on the plane waves. The polarization vectors $\boldsymbol{\epsilon}_{\mathbf{k}, \lambda}$, with $\lambda \in \{1, 2\}$, denote the two directions of polarization transverse to the direction of propagation, $\mathbf{k}/|\mathbf{k}|$. Explicitly calculating $\mathbf{\Pi}(\mathbf{x}, t)$ using Eqs. (2.37) and (2.39) yields

$$\mathbf{\Pi}(\mathbf{x}, t) = -i \sum_{\mathbf{k}, \lambda} \sqrt{\frac{\omega_{\mathbf{k}}}{8\pi c^2 V}} \left[a_{\mathbf{k}, \lambda} \boldsymbol{\epsilon}_{\mathbf{k}, \lambda} e^{i(\mathbf{k} \cdot \mathbf{x} - \omega_{\mathbf{k}} t)} - c.c. \right]. \quad (2.40)$$

The quantities of particular interest in this context are the mode coefficients $a_{\mathbf{k}, \lambda}$ and $a_{\mathbf{k}, \lambda}^\dagger$. The promotion of $\mathbf{A}(\mathbf{x}, t)$ and $\mathbf{\Pi}(\mathbf{x}, t)$ into operators implies that $a_{\mathbf{k}, \lambda}$ and $a_{\mathbf{k}, \lambda}^\dagger$ are also promoted to operators. The commutation relations between $\hat{\mathbf{A}}$ and $\hat{\mathbf{\Pi}}$ immediately allow us to compute the commutation relations between $\hat{a}_{\mathbf{k}, \lambda}$ and $\hat{a}_{\mathbf{k}, \lambda}^\dagger$, with the result:

$$\begin{aligned}[\hat{a}_{\mathbf{k}, \lambda}, \hat{a}_{\mathbf{k}', \lambda'}] &= [\hat{a}_{\mathbf{k}, \lambda}^\dagger, \hat{a}_{\mathbf{k}', \lambda'}^\dagger] = 0 \\ [\hat{a}_{\mathbf{k}, \lambda}, \hat{a}_{\mathbf{k}', \lambda'}^\dagger] &= \delta_{\lambda, \lambda'} \delta_{\mathbf{k}, \mathbf{k}'}.\end{aligned}\quad (2.41)$$

Using Eqs. (2.38)-(2.41), we can write \hat{H}_{rad} as

$$\hat{H}_{\text{rad}} = \int_V d^3x \hat{\mathcal{H}}_{\text{rad}} = \sum_{\mathbf{k}, \lambda} \omega_{\mathbf{k}} \left(\hat{a}_{\mathbf{k}, \lambda}^\dagger \hat{a}_{\mathbf{k}, \lambda} + \frac{1}{2} \right), \quad (2.42)$$

which corresponds to the Hamiltonian for a harmonic oscillator for each mode (\mathbf{k}, λ) . The operators $\hat{a}_{\mathbf{k}, \lambda}$ and $\hat{a}_{\mathbf{k}, \lambda}^\dagger$ now have the remarkable property that if $|n_{\mathbf{k}, \lambda}\rangle$ is an eigenstate of \hat{H}_{rad} with eigenvalue $E_{\mathbf{k}, \lambda}$ (the use of the notation $n_{\mathbf{k}, \lambda}$ will become clear shortly), then $\hat{a}_{\mathbf{k}, \lambda}|n_{\mathbf{k}, \lambda}\rangle$ and $\hat{a}_{\mathbf{k}, \lambda}^\dagger|n_{\mathbf{k}, \lambda}\rangle$ will

be eigenstates of that same Hamiltonian, with eigenvalues $E_{\mathbf{k},\lambda} - \omega_{\mathbf{k}}$ and $E_{\mathbf{k},\lambda} + \omega_{\mathbf{k}}$, respectively.

$$\begin{aligned}
\hat{H}_{\text{rad}}(\hat{a}_{\mathbf{k},\lambda}|n_{\mathbf{k},\lambda}\rangle) &= \left\{ \sum_{\mathbf{k}',\lambda'} \omega_{\mathbf{k}'} \left(\hat{a}_{\mathbf{k}',\lambda'}^\dagger \hat{a}_{\mathbf{k}',\lambda'} + \frac{1}{2} \right) \right\} (\hat{a}_{\mathbf{k},\lambda}|n_{\mathbf{k},\lambda}\rangle) \\
&= \sum_{\mathbf{k}',\lambda'} \omega_{\mathbf{k}'} \left[\left(\hat{a}_{\mathbf{k},\lambda} \hat{a}_{\mathbf{k}',\lambda'}^\dagger - \delta_{\lambda,\lambda'} \delta_{\mathbf{k},\mathbf{k}'} \right) \hat{a}_{\mathbf{k}',\lambda'} + \hat{a}_{\mathbf{k},\lambda} \frac{1}{2} \right] |n_{\mathbf{k},\lambda}\rangle \\
&= \hat{a}_{\mathbf{k},\lambda} \left\{ -\omega_{\mathbf{k}} + \sum_{\mathbf{k}',\lambda'} \omega_{\mathbf{k}'} \left[\hat{a}_{\mathbf{k}',\lambda'}^\dagger \hat{a}_{\mathbf{k}',\lambda'} + \frac{1}{2} \right] \right\} |n_{\mathbf{k},\lambda}\rangle \\
&= \hat{a}_{\mathbf{k},\lambda} (\hat{H}_{\text{rad}} - \omega_{\mathbf{k}}) |n_{\mathbf{k},\lambda}\rangle \\
&= (E_{\mathbf{k}} - \omega_{\mathbf{k}}) \hat{a}_{\mathbf{k},\lambda} |n_{\mathbf{k},\lambda}\rangle, \tag{2.43}
\end{aligned}$$

and similarly $\hat{H}_{\text{rad}}(\hat{a}_{\mathbf{k},\lambda}^\dagger |n_{\mathbf{k},\lambda}\rangle) = (E_{\mathbf{k}} + \omega_{\mathbf{k}}) \hat{a}_{\mathbf{k},\lambda}^\dagger |n_{\mathbf{k},\lambda}\rangle$, i.e., a single quantum of energy, $\omega_{\mathbf{k}}$, has been respectively removed and added to the mode (\mathbf{k}, λ) . Equivalently, this can be interpreted as a single particle, in this case photon, having been annihilated from or created in the mode (\mathbf{k}, λ) . For this reason, $\hat{a}_{\mathbf{k},\lambda}$ and $\hat{a}_{\mathbf{k},\lambda}^\dagger$ are known as annihilation and creation operators respectively. The number of photons, $n_{\mathbf{k},\lambda}$, in each mode (\mathbf{k}, λ) fully characterizes each eigenstate $|n_{\mathbf{k},\lambda}\rangle$, which are called Fock states. The value $n_{\mathbf{k},\lambda}$ is the eigenvalue of the number operator, $\hat{n}_{\mathbf{k},\lambda}$, which can be read off from Eq. (2.42) as:

$$\hat{n}_{\mathbf{k},\lambda} = \hat{a}_{\mathbf{k},\lambda}^\dagger \hat{a}_{\mathbf{k},\lambda}. \tag{2.44}$$

We can see that $\hat{a}_{\mathbf{k},\lambda}|n_{\mathbf{k},\lambda}\rangle \sim |n_{\mathbf{k},\lambda} - 1\rangle$ and $\hat{a}_{\mathbf{k},\lambda}^\dagger |n_{\mathbf{k},\lambda}\rangle \sim |n_{\mathbf{k},\lambda} + 1\rangle$, and by normalizing $\hat{a}_{\mathbf{k},\lambda}|n_{\mathbf{k},\lambda}\rangle$ and $\hat{a}_{\mathbf{k},\lambda}^\dagger |n_{\mathbf{k},\lambda}\rangle$, they satisfy

$$\begin{aligned}
\hat{a}_{\mathbf{k},\lambda}|n_{\mathbf{k},\lambda}\rangle &= \sqrt{n_{\mathbf{k},\lambda}} |n_{\mathbf{k},\lambda} - 1\rangle \\
\hat{a}_{\mathbf{k},\lambda}^\dagger |n_{\mathbf{k},\lambda}\rangle &= \sqrt{n_{\mathbf{k},\lambda} + 1} |n_{\mathbf{k},\lambda} + 1\rangle \tag{2.45}
\end{aligned}$$

This shows that changing the number of particles, in this case photons, can be easily accounted for by the operators $\hat{a}_{\mathbf{k},\lambda}$ and $\hat{a}_{\mathbf{k},\lambda}^\dagger$. Note that the particle-like photonic nature of the electromagnetic fields arose from the commutation relations between $\hat{a}_{\mathbf{k},\lambda}$ and $\hat{a}_{\mathbf{k},\lambda}^\dagger$, which in turn originated from tuning the fields \mathbf{A} and $\mathbf{\Pi}$ into quantized operators. So allow us to reiterate the essence of second quantization [stated directly after Eq. (2.25)] from this example: "As such, the normal modes $[a_{\mathbf{k},\lambda}$ and $a_{\mathbf{k},\lambda}^\dagger]$ of the (now quantum) field $[\hat{\mathbf{A}}(\mathbf{x}, t)]$, after defining some basis to represent it in [plane waves] become quantized $[\hat{a}_{\mathbf{k},\lambda}$ and $\hat{a}_{\mathbf{k},\lambda}^\dagger]$ in conjunction with the commutation relations in Eq. (2.41)]. These discrete excitations that comprise the quantum field are interpreted as particles [photons]."

Of course, much more could be said about the quantized electromagnetic field, but the whole purpose of this exercise was to show an example of the general recipe for developing a quantum theory in second quantization (also referred to as the process of canonical quantization). We summarize it below:

- 1): Identify a Lagrangian (density).
- 2): Identify the relevant canonically conjugate variables.
- 3): Construct the Hamiltonian (density).
- 4): Promote the canonically conjugate variables to operators and impose canonical commutation relations on them.
- 5): Construct the quantum-mechanical Hamiltonian operator.

From the Hamiltonian operator, the energies and eigenfunctions may subsequently be determined as per Eq. (2.24).

Let us now use this formalism of second quantization to develop a quantum theory of the many-electron system.

2.3 Many-electron system

We consider a system consisting of electrons and nuclei. Its Hamiltonian should contain: (i) the kinetic energies of the electrons and nuclei, (ii) the Coulomb attraction between electrons and nuclei, (iii) the Coulomb repulsion between the nuclei, and (iv) the Coulomb repulsion between the electrons. In this thesis, we will only perform electronic structure calculations in systems where the Coulomb interaction between nuclei need not be considered, nor will we consider the kinetic energy of the nuclei, which is much smaller than that of electrons due to the large mass of the nuclei. Therefore, our (classical) Hamiltonian takes on the form:

$$H = \sum_i \left(\frac{\mathbf{p}_i^2}{2} - \sum_n \frac{Z_n}{|\mathbf{q}_i - \mathbf{R}_n|} \right) + \frac{1}{2} \sum_{\substack{i,j \\ i \neq j}} \frac{1}{|\mathbf{q}_i - \mathbf{q}_j|}, \quad (2.46)$$

where Z_n and \mathbf{R}_n are the nuclear charge and the position of the n -th nucleus, and \mathbf{q}_i and \mathbf{p}_i the position and momentum of the i -th electron. In first quantization, one would promote \mathbf{q}_i and \mathbf{p}_i to be operators, with canonical commutation relations and proceed by letting the resulting Hamiltonian operator, \hat{H} , act on a wave function describing the electrons $\psi(\mathbf{x}_1, \mathbf{x}_2, \dots, \mathbf{x}_N)$, to solve the eigenvalue equation $\hat{H}\psi = E\psi$. However, this scheme is again dependent on the number of particles, N , in our system. So, keeping in mind the relevant physics we wish to capture from Eq. (2.46), let us proceed by applying the recipe of canonical quantization alluded to in the previous Sec. 2.2.2 to the many-electron system.

2.3.1 Quantizing the electron field

In Sec. 2.2.2, we described photons as excitations of a quantum field. In an analogous way, we will describe electrons as excitations of their own quantum field, denoted by $\psi(\mathbf{x}, t)$. Note the difference between this field $\psi(\mathbf{x}, t)$ and the wave function $\Psi(\mathbf{x}_1, \mathbf{x}_2, \dots, \mathbf{x}_N, t)$ from Sec. 2.2.1. In the latter case, a collection of electrons is described as a collection of particles. This is apparent from the dependence of Ψ on the explicit positions of the electrons, $\mathbf{x}_1, \mathbf{x}_2, \dots, \mathbf{x}_N$. In contrast, we are about to forego this particle description. Just as how we started from an electromagnetic field in Sec. 2.2.2 to describe all photons, we will describe all electrons by a single complex electron field, $\psi(\mathbf{x}, t)$.

In order for the field $\psi(\mathbf{x}, t)$ to describe electrons, we want it to incorporate spin. The field $\psi(\mathbf{x}, t)$ therefore really takes on the form of a two-component spinor field

$$\psi(\mathbf{x}, t) = \begin{pmatrix} \psi_{1/2}(\mathbf{x}, t) \\ \psi_{-1/2}(\mathbf{x}, t) \end{pmatrix}. \quad (2.47)$$

To have this field to describe electrons, we impose that each of its spinor components satisfies the Schrödinger equation with a Hamiltonian describing the same physics as Eq. (2.46). Therefore, we have an equation of motion for each of the two spin-components of $\psi(\mathbf{x}, t)$:

$$i\dot{\psi}_\sigma(\mathbf{x}, t) = \left\{ -\frac{1}{2}\nabla^2 - \sum_n \frac{Z_n}{|\mathbf{x} - \mathbf{R}_n|} + \int d^3x' \frac{\rho(\mathbf{x}', t)}{|\mathbf{x} - \mathbf{x}'|} \right\} \psi_\sigma(\mathbf{x}, t), \quad (2.48)$$

where $\sigma \in \{-1/2, +1/2\}$ and the electron density $\rho(\mathbf{x}, t) = \psi^\dagger(\mathbf{x}, t)\psi(\mathbf{x}, t)$. A Lagrangian that leads to this equation of motion is:

$$\begin{aligned} L[\psi, \dot{\psi}, \psi^\dagger] = & i \int d^3x \psi^\dagger(\mathbf{x}, t) \dot{\psi}(\mathbf{x}, t) \\ & - \int d^3x \psi^\dagger(\mathbf{x}, t) \left[-\frac{1}{2}\nabla^2 - \sum_n \frac{Z_n}{|\mathbf{x} - \mathbf{R}_n|} \right] \psi(\mathbf{x}, t) \\ & - \frac{1}{2} \int d^3x \int d^3x' \psi^\dagger(\mathbf{x}, t) \left[\frac{\psi^\dagger(\mathbf{x}', t)\psi(\mathbf{x}', t)}{|\mathbf{x} - \mathbf{x}'|} \right] \psi(\mathbf{x}, t), \end{aligned} \quad (2.49)$$

as we will now show. As we are working with a (spinor) field, our first step is to define a Lagrangian density \mathcal{L} . Unfortunately, because the third term involves an integration over all of space, we cannot write this Lagrangian in terms of a Lagrangian density \mathcal{L} , that is itself a function of only the fields and their (local) temporal and spatial derivatives, as we did in Sec. 2.1. Fortunately, the principle of stationary action $\delta S = 0$ itself made no such assumption, and is still applicable to this case. For each σ -component, it

just yields E-L equations in terms of functional derivatives with respect to the fields $\psi_\sigma(\mathbf{x}, t)$ and $\dot{\psi}_\sigma(\mathbf{x}, t)$, and $\psi_\sigma^*(\mathbf{x}, t)$ and $\dot{\psi}_\sigma^*(\mathbf{x}, t)$:

$$\begin{aligned} \delta S &= \int_{t_1}^{t_2} dt \delta L[\psi_\sigma, \dot{\psi}_\sigma, \psi_\sigma^*, \dot{\psi}_\sigma^*] = 0 \\ &= \int_{t_1}^{t_2} dt \left\{ \frac{\delta L}{\delta \psi_\sigma} \delta \psi_\sigma + \frac{\delta L}{\delta \dot{\psi}_\sigma} \delta \dot{\psi}_\sigma + \frac{\delta L}{\delta \psi_\sigma^*} \delta \psi_\sigma^* + \frac{\delta L}{\delta \dot{\psi}_\sigma^*} \delta \dot{\psi}_\sigma^* \right\}. \end{aligned} \quad (2.50)$$

Since the fields $\psi_\sigma(\mathbf{x}, t)$ and $\psi_\sigma^*(\mathbf{x}, t)$ are independent, the first two terms and the last two terms must be equal to zero separately. Proceeding similarly to what we did in Sec. 2.1, we can use the chain rule on $\delta \dot{\psi}$ and impose proper fall-off conditions such that a total time derivative does not survive the integration. This leads to the E-L equations:

$$\frac{d}{dt} \frac{\delta L}{\delta \dot{\psi}_\sigma} - \frac{\delta L}{\delta \psi_\sigma} = 0, \quad \text{and} \quad \frac{d}{dt} \frac{\delta L}{\delta \dot{\psi}_\sigma^*} - \frac{\delta L}{\delta \psi_\sigma^*} = 0. \quad (2.51)$$

The second equation will yield our equation of motion [Eq. (2.48)]. If we use the general functional-derivative rules

$$\frac{\delta f(\mathbf{x}, t)}{\delta f(\mathbf{x}', t)} = \delta(\mathbf{x} - \mathbf{x}') \quad (2.52a)$$

$$\frac{\delta F[f(\mathbf{x}, t)]}{\delta f(\mathbf{x}', t)} = \left(\frac{\delta F[f(\mathbf{x}, t)]}{\delta f(\mathbf{x}, t)} \right) \left(\frac{\delta f(\mathbf{x}, t)}{\delta f(\mathbf{x}', t)} \right), \quad (2.52b)$$

for a function $f(\mathbf{x}, t)$ and a functional $F[f]$, we obtain $\delta L / \delta \dot{\psi}_\sigma^* = 0$ (trivially) and find $\delta L / \delta \psi_\sigma^*$ equal to:

$$i\dot{\psi}_\sigma(\mathbf{x}, t) - \left\{ -\frac{1}{2}\nabla^2 - \sum_n \frac{Z_n}{|\mathbf{x} - \mathbf{R}_n|} + \int d^3x' \frac{\rho(\mathbf{x}', t)}{|\mathbf{x} - \mathbf{x}'|} \right\} \psi_\sigma(\mathbf{x}, t). \quad (2.53)$$

As this is equal to zero, we recover Eq. (2.48). Repeating this scheme with the other E-L equation, we obtain the complex conjugate of Eq. (2.48).

Having found a Lagrangian that reproduces the equations of motion, we may define the canonical momentum density conjugate to $\psi_\sigma(\mathbf{x}, t)$:

$$\Pi_\sigma(\mathbf{x}, t) = \frac{\delta L}{\delta \dot{\psi}_\sigma} = i\psi_\sigma^*(\mathbf{x}, t). \quad (2.54)$$

With it, we can find the relevant Hamiltonian, H_{matter} , expressed in terms of the spinor field $\psi(\mathbf{x}, t)$:

$$\begin{aligned} H_{\text{matter}} &= \int d^3x \sum_\sigma \Pi_\sigma(\mathbf{x}, t) \dot{\psi}_\sigma(\mathbf{x}, t) \\ &= \int d^3x \psi^\dagger(\mathbf{x}, t) \left[-\frac{1}{2}\nabla^2 - \sum_n \frac{Z_n}{|\mathbf{x} - \mathbf{R}_n|} \right] \psi(\mathbf{x}, t) \\ &\quad + \frac{1}{2} \int d^3x \int d^3x' \psi^\dagger(\mathbf{x}, t) \left[\frac{\psi^\dagger(\mathbf{x}', t) \psi(\mathbf{x}', t)}{|\mathbf{x} - \mathbf{x}'|} \right] \psi(\mathbf{x}, t). \end{aligned} \quad (2.55)$$

We now have all the necessary ingredients required to quantize our theory. We promote the fields $\psi(\mathbf{x}, t)$ and $\Pi(\mathbf{x}, t)$ into operators $\hat{\psi}(\mathbf{x})$ and $\hat{\Pi}(\mathbf{x})$, which, in turn, promotes the Hamiltonian H_{matter} into the operator \hat{H}_{matter} . The operators do not exhibit time dependence as we employ the Schrödinger picture (see Sec 2.4.1).

To proceed, we need to impose commutation relations on the operators $\hat{\psi}(\mathbf{x})$ and $\hat{\Pi}(\mathbf{x})$. However, we know that the fermionic wave function is anti-symmetric in first quantization: $\Psi(\dots, \mathbf{x}_i, \dots, \mathbf{x}_j, \dots, t) = -\Psi(\dots, \mathbf{x}_j, \dots, \mathbf{x}_i, \dots, t)$, for $i, j \in \{1, \dots, N\}$ and $i \neq j$. Therefore, to reproduce this behavior we have to impose for our field operators the relation: $\hat{\psi}(\mathbf{x})\hat{\psi}(\mathbf{x}') = -\hat{\psi}(\mathbf{x}')\hat{\psi}(\mathbf{x})$. To achieve this, the commutator relations are instead replaced by *anticommutator* relations, imposing:

$$\begin{aligned} \{\hat{\psi}_\sigma(\mathbf{x}), \hat{\psi}_{\sigma'}(\mathbf{x}')\} &= \{\hat{\Pi}_\sigma(\mathbf{x}), \hat{\Pi}_{\sigma'}(\mathbf{x}')\} = 0 \\ \{\hat{\psi}_\sigma(\mathbf{x}), \hat{\Pi}_{\sigma'}(\mathbf{x}')\} &= i\delta_{\sigma, \sigma'}\delta(\mathbf{x} - \mathbf{x}'), \end{aligned} \quad (2.56)$$

where $\{a, b\} = ab + ba$, or by using $\hat{\Pi}(\mathbf{x}) = i\hat{\psi}^\dagger(\mathbf{x})$:

$$\begin{aligned} \{\hat{\psi}_\sigma(\mathbf{x}), \hat{\psi}_{\sigma'}(\mathbf{x}')\} &= \{\hat{\psi}_\sigma^\dagger(\mathbf{x}), \hat{\psi}_{\sigma'}^\dagger(\mathbf{x}')\} = 0 \\ \{\hat{\psi}_\sigma(\mathbf{x}), \hat{\psi}_{\sigma'}^\dagger(\mathbf{x}')\} &= \delta_{\sigma, \sigma'}\delta(\mathbf{x} - \mathbf{x}'). \end{aligned} \quad (2.57)$$

Having identified the relevant Hamiltonian operator and canonical variables, we may consider how we regain the particle-like behavior for electrons from the spinor field $\hat{\psi}(\mathbf{x})$. As with the electromagnetic field in Sec. 2.2.2, they will arise as excitations of certain modes of the quantum field with respect to some basis.

To this end, we proceed by considering the mode expansion of $\hat{\psi}(\mathbf{x})$ and $\hat{\psi}^\dagger(\mathbf{x})$ in terms of a complete, orthonormal, enumerable basis of vectors, $\varphi_p(\mathbf{x})$, that are part of an L^2 -Hilbert space, so that $\langle \varphi_p | \varphi_q \rangle = \delta_{p, q}$:

$$\hat{\psi}(\mathbf{x}) = \sum_p \hat{c}_p \varphi_p(\mathbf{x}), \quad \text{and} \quad \hat{\psi}^\dagger(\mathbf{x}) = \sum_p \hat{c}_p^\dagger \varphi_p^\dagger(\mathbf{x}). \quad (2.58)$$

From the completeness of the states $\varphi_p(\mathbf{x})$, we can find the expansion coefficients \hat{c}_p and \hat{c}_p^\dagger :

$$\hat{c}_p = \int d^3x \varphi_p^\dagger(\mathbf{x}) \hat{\psi}(\mathbf{x}), \quad \text{and} \quad \hat{c}_p^\dagger = \int d^3x \hat{\psi}^\dagger(\mathbf{x}) \varphi_p(\mathbf{x}). \quad (2.59)$$

The anticommutation relations between $\hat{\psi}(\mathbf{x})$ and $\hat{\psi}^\dagger(\mathbf{x})$ immediately allow us to calculate the anticommutation relations between \hat{c}_p and \hat{c}_p^\dagger :

$$\begin{aligned} \{\hat{c}_p, \hat{c}_q\} &= \{\hat{c}_p^\dagger, \hat{c}_q^\dagger\} = 0 \\ \{\hat{c}_p, \hat{c}_q^\dagger\} &= \delta_{p, q}. \end{aligned} \quad (2.60)$$

The similarity between the operators \hat{c}_p and \hat{c}_p^\dagger and the annihilation and creation operators, $\hat{a}_{\mathbf{k},\lambda}$ and $\hat{a}_{\mathbf{k},\lambda}^\dagger$, of the electromagnetic field is apparent. Whereas the latter obeyed commutation relations [Eq. (2.41)] consistent with the photon's bosonic nature, the former obey anticommutation relations [Eq. (2.60)] consistent with the electron's fermionic nature. The operators \hat{c}_p and \hat{c}_p^\dagger also share a similar physical interpretation and are the annihilation and creation operators of the electron field. The anticommutation relations allow us to recover many fermionic properties for any state vector $|\Phi\rangle$:

- From $\{\hat{c}_p, \hat{c}_p\} = 0$ and $\{\hat{c}_p^\dagger, \hat{c}_p^\dagger\} = 0$, we can immediately see that $\hat{c}_p \hat{c}_p |\Phi\rangle = \hat{c}_p^\dagger \hat{c}_p^\dagger |\Phi\rangle = 0$, implying that no two identical electrons may occupy the same quantum state, thus recovering Pauli's exclusion principle.
- We can define a number operator $\hat{n}_p = \hat{c}_p^\dagger \hat{c}_p$, which is a suitable choice for a number operator as it only has 0 and 1 as eigenvalues:

$$\begin{aligned} (\hat{c}_p^\dagger \hat{c}_p)^2 &= 1 - 2\hat{c}_p \hat{c}_p^\dagger + \hat{c}_p (1 - \hat{c}_p \hat{c}_p^\dagger) \hat{c}_p^\dagger \\ &= 1 - \hat{c}_p \hat{c}_p^\dagger \\ &= \hat{c}_p^\dagger \hat{c}_p, \end{aligned} \quad (2.61)$$

which indicates that $\hat{c}_p^\dagger \hat{c}_p (1 - \hat{c}_p^\dagger \hat{c}_p) = \hat{n}_p (1 - \hat{n}_p) = 0$.

- The vacuum state, $|0\rangle$, is defined to have no electrons present, so that $\hat{c}_p |0\rangle = 0$, resulting in $\hat{n}_p |0\rangle = 0$ and $\hat{n}_p \hat{c}_p^\dagger |0\rangle = 1$.
- Assuming that the vacuum state is normalized, $\langle 0|0\rangle = 1$, then for a single node p , the eigenstates, $|n_p\rangle$ of \hat{n}_p form a complete set, i.e. $\sum_{n_p=0}^1 |n_p\rangle \langle n_p| = \mathbf{1}_p$.
- Finally, one can define multi-orbital states, which are Fock states, from the vacuum state $|0\rangle$ as:

$$\begin{aligned} |\{n_p\}\rangle &\equiv |n_1, n_2, \dots\rangle \equiv |n_1\rangle |n_2\rangle \dots \\ &= \prod_{p=1}^{\infty} (\hat{c}_p^\dagger)^{n_p} |0\rangle, \quad \text{for } n_p = 0, 1. \end{aligned} \quad (2.62)$$

We may conclude that we may describe our many-electron system using a Hamiltonian operator, \hat{H}_{matter} :

$$\begin{aligned} \hat{H}_{\text{matter}} &= \int d^3x \hat{\psi}^\dagger(\mathbf{x}) \left[-\frac{1}{2} \nabla^2 - \sum_n \frac{Z_n}{|\mathbf{x} - \mathbf{R}_n|} \right] \hat{\psi}(\mathbf{x}) \\ &\quad + \frac{1}{2} \int d^3x \int d^3x' \hat{\psi}^\dagger(\mathbf{x}) \left[\frac{\hat{\psi}^\dagger(\mathbf{x}') \hat{\psi}(\mathbf{x}')}{|\mathbf{x} - \mathbf{x}'|} \right] \hat{\psi}(\mathbf{x}), \end{aligned} \quad (2.63)$$

where $\hat{\psi}(\mathbf{x})$ is a two-component spin-field operator, satisfying the anticommutation relations in Eq. (2.57). From these, a mode expansion of $\hat{\psi}(\mathbf{x})$ in a complete orthonormal basis of L^2 -Hilbert-space vectors [Eq. (2.58)], allows us to identify the coefficients as fermionic annihilation and creation operators that treat electrons as specific mode excitations of the quantum spinor field.

As a final note, we show an easy “recipe” to convert an (electronic) operator from first quantization to second quantization and back. It goes as follows. For every discrete position \mathbf{x}_i being summed over i , convert this to a continuous variable \mathbf{x} , place the resulting expression between $\hat{\psi}^\dagger(\mathbf{x})\dots\hat{\psi}(\mathbf{x})$ and integrate over d^3x . In order to go back to first quantization, turn every continuous \mathbf{x} that is being integrated over in $\int d^3x \hat{\psi}^\dagger(\mathbf{x})\dots\hat{\psi}(\mathbf{x})$ into a discrete \mathbf{x}_i being summed over i . As an example, consider the density operator in first quantization: $\hat{n}(\mathbf{x}) = \sum_i \delta(\mathbf{x} - \mathbf{x}_i)$, where i runs over all electrons considered. Following our recipe, we have

$$\hat{n}(\mathbf{x}) = \sum_i \delta(\mathbf{x} - \mathbf{x}_i) = \int d^3x' \hat{\psi}^\dagger(\mathbf{x}) \delta(\mathbf{x} - \mathbf{x}') \hat{\psi}(\mathbf{x}) = \hat{\psi}^\dagger(\mathbf{x}) \hat{\psi}(\mathbf{x}). \quad (2.64)$$

This recipe also allows for a quick comparison between the Hamiltonians in Eqs. (2.46) and (2.63).

2.3.2 Hartree-Fock-Slater equations

Admittedly, the developed formalism does not indicate how to proceed in actually *solving* $\hat{H}_{\text{matter}}|\psi\rangle = E|\psi\rangle$. For that we need to turn our attention to the complete basis of L^2 -Hilbert-space vectors, $|\varphi_p\rangle$, that we used in our mode expansion. For simplicity, let us assume that these states are one-particle states and are thus henceforth referred to as spin orbitals. Let us further assume that they satisfy a Schrödinger-like equation of the form:

$$\bar{H}\varphi_p(\mathbf{x}) \equiv \left[-\frac{1}{2}\nabla^2 - \sum_n \frac{Z_n}{|\mathbf{x} - \mathbf{R}_n|} + \bar{V}(\mathbf{x}) \right] \varphi_p(\mathbf{x}) = \varepsilon_p \varphi_p(\mathbf{x}) \quad (2.65)$$

where ε_p is the energy eigenvalue of the spin orbital $\varphi_p(\mathbf{x})$ and $\bar{V}(\mathbf{x})$ is some hitherto unmentioned mean-field potential describing the interaction of the one electron in the state $\varphi_p(\mathbf{x})$ with all other electrons. Its usefulness will become apparent shortly. As $\varphi_p(\mathbf{x})$ describes a one-particle state, the defined Hamiltonian operator, \bar{H} [Eq. (2.65)], is a so-called one-body operator. In general, a one-body operator, which acts on only one coordinate, has the general form $\hat{t} = \sum_i \hat{t}(\mathbf{x}_i)$. We can rewrite this operator in second quantization as

$$\hat{t} = \int d^3x \hat{\psi}^\dagger(\mathbf{x}) t(\mathbf{x}) \hat{\psi}(\mathbf{x}), \quad (2.66)$$

or after rewriting our field operators in terms of $\varphi_p(\mathbf{x})$:

$$\begin{aligned}\hat{t} &= \sum_{p,q} \hat{c}_p^\dagger \hat{c}_q \int d^3x \varphi_p^\dagger(\mathbf{x}) t(\mathbf{x}) \varphi_q(\mathbf{x}) \\ &= \sum_{p,q} \hat{c}_p^\dagger \hat{c}_q \langle \varphi_p | t(\mathbf{x}) | \varphi_q \rangle \equiv \sum_{p,q} \hat{c}_p^\dagger \hat{c}_q t_{pq},\end{aligned}\quad (2.67)$$

where the matrix element $t_{pq} = \langle \varphi_p | t(\mathbf{x}) | \varphi_q \rangle$ was defined. We can repeat this for a general two-body operator:

$$\begin{aligned}\hat{v} &= \frac{1}{2} \sum_{\substack{i,j \\ i \neq j}} \hat{v}(\mathbf{x}_i, \mathbf{x}_j) = \frac{1}{2} \int d^3x \int d^3x' \hat{\psi}^\dagger(\mathbf{x}) \hat{\psi}^\dagger(\mathbf{x}') v(\mathbf{x}, \mathbf{x}') \hat{\psi}(\mathbf{x}') \hat{\psi}(\mathbf{x}) \\ &= \frac{1}{2} \sum_{p,q,r,s} \hat{c}_p^\dagger \hat{c}_q^\dagger \hat{c}_s \hat{c}_r \int d^3x \int d^3x' \varphi_p^\dagger(\mathbf{x}) \varphi_q^\dagger(\mathbf{x}') v(\mathbf{x}, \mathbf{x}') \varphi_r(\mathbf{x}) \varphi_s(\mathbf{x}') \\ &= \frac{1}{2} \sum_{p,q,r,s} \hat{c}_p^\dagger \hat{c}_q^\dagger \hat{c}_s \hat{c}_r v_{pqrs}.\end{aligned}\quad (2.68)$$

We can use these expansions on \hat{H}_{matter} from Eq. (2.63). Let us collect the one-body part and the two-body part under the names \hat{H}_{bare} and \hat{V}_{e-e} , respectively, so that:

$$\begin{aligned}\hat{H}_{\text{bare}} &= \int d^3x \hat{\psi}^\dagger(\mathbf{x}) \left[-\frac{1}{2} \nabla^2 - \sum_n \frac{Z_n}{|\mathbf{x} - \mathbf{R}_n|} \right] \hat{\psi}(\mathbf{x}) \\ \hat{V}_{e-e} &= \frac{1}{2} \int d^3x \int d^3x' \hat{\psi}^\dagger(\mathbf{x}) \left[\frac{\hat{\psi}^\dagger(\mathbf{x}') \hat{\psi}(\mathbf{x}')}{|\mathbf{x} - \mathbf{x}'|} \right] \hat{\psi}(\mathbf{x}),\end{aligned}\quad (2.69)$$

which become, in terms of our spin orbitals

$$\begin{aligned}\hat{H}_{\text{bare}} &= \sum_{p,q} \langle \varphi_p | \left[-\frac{1}{2} \nabla^2 - \sum_n \frac{Z_n}{|\mathbf{x} - \mathbf{R}_n|} \right] | \varphi_q \rangle \hat{c}_p^\dagger \hat{c}_q \\ \hat{V}_{e-e} &= \frac{1}{2} \sum_{p,q,r,s} \hat{c}_p^\dagger \hat{c}_q^\dagger \hat{c}_s \hat{c}_r v_{pqrs},\end{aligned}\quad (2.70)$$

where

$$v_{pqrs} = \int d^3x \int d^3x' \varphi_p^\dagger(\mathbf{x}) \varphi_q^\dagger(\mathbf{x}') \frac{1}{|\mathbf{x} - \mathbf{x}'|} \varphi_r(\mathbf{x}) \varphi_s(\mathbf{x}'). \quad (2.71)$$

The key step is to add and subtract the one-body operator \hat{V} to \hat{H}_{matter} , and to group together $\hat{H}_{\text{bare}} + \hat{V} \equiv \hat{\hat{H}}$ and $\hat{V}_{e-e} - \hat{V} \equiv \hat{\hat{V}}_{\text{res}}$. This is because the operator defined as $\hat{\hat{H}}$ exactly has the spin orbitals $\varphi_p(\mathbf{x})$ as eigenstates, with eigenvalues ε_p , as can be seen from Eq. (2.65). This allows it to take on

the simple form $\hat{H} = \sum_p \varepsilon_p \hat{n}_p$. The useful property we have just discovered is that, if we can find some mean-field potential \hat{V} such that the effect of \hat{V}_{res} is very small compared to \hat{H} , we can accurately approximate the effect of \hat{H}_{matter} by a one-particle Hamiltonian \hat{H} (!), for which we only need to solve Eq. (2.65). So, the question of interest becomes: what is the best choice of \hat{V} to achieve this goal? The answer is provided by the derivation of the Hartree-Fock equations.

To derive these equations, we must unfortunately make a slight detour to address the following point. On the one hand, since $\hat{H} = \sum_p \varepsilon_p \hat{n}_p$, we know that its eigenstates are the Fock states $|\{n_p\}\rangle$. On the other hand, we know from Eq. (2.65) that the spin orbitals $\varphi_p(\mathbf{x})$ are also eigenfunctions of \hat{H} . Can a relation be found between the two? Fortunately, the answer is yes. We may reduce the matrix elements of \hat{H} with respect to a basis of Fock states to matrix elements with respect to spin orbitals using the so-called Condon rules. An explicit derivation is presented for one-body operators. The results for two-body operators we will only quote. We start with the matrix element $\langle \{n_p\} | \hat{t} | \{n_q\} \rangle = \sum_{r,s} t_{rs} \langle \{n_p\} | \hat{c}_r^\dagger \hat{c}_s | \{n_q\} \rangle$. Let us introduce some notation. We will invoke the shorthand notation $|\{n_q\}\rangle = |\Phi\rangle$, and use the indices $i, j, \dots / a, b, \dots$ to indicate occupied/unoccupied spin orbitals in $|\Phi\rangle$, so $n_i = n_j = 1$ and $n_a = n_b = 0$. There are only a few possibilities that will give a non-zero contribution:

- $r = s$: in this case $\hat{c}_r^\dagger \hat{c}_r |\{n_q\}\rangle = \hat{n}_r |\{n_q\}\rangle$, which will only give a contribution if $n_r = 1$, and $|\{n_p\}\rangle = |\{n_q\}\rangle$. So then $\langle \{n_p\} | \hat{t} | \{n_q\} \rangle = \langle \Phi | \hat{t} | \Phi \rangle = \sum_{r,s} t_{rs} \langle \Phi | \hat{c}_r^\dagger \hat{c}_s | \Phi \rangle = \sum_i t_{ii}$.
- $r \neq s$: now $\hat{c}_r^\dagger \hat{c}_s |\{n_q\}\rangle$ will only be non-zero if in $|\{n_q\}\rangle$, $n_s = 1$, and $n_r = 0$. This will only yield a contribution if we can construct $|\{n_p\}\rangle$ from $|\{n_q\}\rangle$. $|\{n_p\}\rangle$ is then constructed by taking an electron from an occupied orbital in $|\{n_q\}\rangle$ and placing it in an unoccupied orbital of $|\{n_q\}\rangle$. If we consider a single substitution, then $|\{n_p\}\rangle = \hat{c}_a^\dagger \hat{c}_i |\Phi\rangle \equiv |\Phi_i^a\rangle$, for which $\langle \{n_p\} | \hat{t} | \{n_q\} \rangle = \langle \Phi_i^a | \hat{t} | \Phi \rangle = \sum_{r,s} t_{rs} \langle \Phi_i^a | \hat{c}_r^\dagger \hat{c}_s | \Phi \rangle = t_{ai}$. One can show that double or higher substitutions will yield zero.

The results for two-body operators are

$$\langle \Phi | \hat{v} | \Phi \rangle = \frac{1}{2} \sum_{i,j} v_{ij[ij]}, \quad \langle \Phi_i^a | \hat{v} | \Phi \rangle = \sum_j v_{aj[ij]}, \quad \langle \Phi_{ij}^{ab} | \hat{v} | \Phi \rangle = v_{ab[ij]}, \quad (2.72)$$

with all other contributions yielding zero. $v_{ij[ij]}$ refers to the antisymmetrization operation, i.e. $v_{ij[ij]} = v_{ijij} - v_{ijji}$.

We can use the Condon rules to derive the Hartree-Fock equations which will provide us with an expression for \hat{V} . From the variational principle, given some Hamiltonian operator, we know that its expectation value with

respect to any normalized wave function (not necessarily an eigenstate) gives an energy value that is greater than or equal to the ground-state energy, E_0 . The key step is to write out the expectation value of \hat{H}_{matter} in a basis of eigenstates of \hat{H}_{bare} , i.e., Fock states $|\Phi\rangle$. The goal of the Hartree-Fock equations is to determine the Fock state $|\Phi_0^N\rangle$ that best approximates the ground state of \hat{H}_{matter} . We do this by writing out $\langle\Phi_0^N|\hat{H}_{\text{matter}}|\Phi_0^N\rangle$ in terms of spin orbitals $\varphi_{i,\sigma}(\mathbf{x})$ and $\varphi_{i,\sigma}^*(\mathbf{x})$ (where we separated the spin index σ from the spatial index i) and subsequently minimizing it by varying it with respect to these spin orbitals, and setting it equal to zero. Therefore, the functional to minimize is

$$\tilde{E}[\varphi_{i,\sigma}(\mathbf{x}), \varphi_{i,\sigma}^*(\mathbf{x})] = \langle\Phi_0^N|\hat{H}_{\text{matter}}|\Phi_0^N\rangle - \sum_i \varepsilon_i [\langle\varphi_i|\varphi_i\rangle - 1], \quad (2.73)$$

where ε_i are Lagrange multipliers introduced to minimize the expectation value $\langle\Phi_0^N|\hat{H}_{\text{matter}}|\Phi_0^N\rangle$, with the constraint that the spin orbitals $\varphi_{i,\sigma}(\mathbf{x})$ are normalized to 1. Using the Condon rules, we may express $\tilde{E}[\varphi_{i,\sigma}(\mathbf{x}), \varphi_{i,\sigma}^*(\mathbf{x})]$ in terms of the spin orbitals:

$$\begin{aligned} \tilde{E}[\varphi_{i,\sigma}(\mathbf{x}), \varphi_{i,\sigma}^*(\mathbf{x})] &= \sum_i \langle\varphi_i| \left[-\frac{1}{2}\nabla^2 - \sum_n \frac{Z_n}{|\mathbf{x} - \mathbf{R}_n|} \right] |\varphi_i\rangle \\ &\quad + \frac{1}{2} \sum_{j,k} v_{jk}[jk] - \sum_i \varepsilon_i [\langle\varphi_i|\varphi_i\rangle - 1]. \end{aligned} \quad (2.74)$$

From calculating $\delta\tilde{E}[\varphi_{i,\sigma}(\mathbf{x}), \varphi_{i,\sigma}^*(\mathbf{x})]/\delta\varphi_{i,\sigma}^*(\mathbf{x}) = 0$, we find the first term to result in:

$$\begin{aligned} \frac{\delta}{\delta\varphi_{i,\sigma}^*(\mathbf{x})} \left\{ \sum_i \langle\varphi_i| \left[-\frac{1}{2}\nabla^2 - \sum_n \frac{Z_n}{|\mathbf{x} - \mathbf{R}_n|} \right] |\varphi_i\rangle \right\} \\ = \left[-\frac{1}{2}\nabla^2 - \sum_n \frac{Z_n}{|\mathbf{x} - \mathbf{R}_n|} \right] \varphi_{i,\sigma}(\mathbf{x}), \end{aligned} \quad (2.75)$$

the second term in:

$$\begin{aligned} \frac{1}{2} \frac{\delta}{\delta\varphi_{i,\sigma}^*(\mathbf{x})} \sum_{j,k} v_{jk}[jk] &= \frac{1}{2} \sum_{j,k} \sum_{\sigma_1, \sigma_2} \int d^3x_1 \int d^3x_2 \\ \frac{\delta}{\delta\varphi_{i,\sigma}^*(\mathbf{x})} \left\{ \frac{\varphi_{j,\sigma_1}^*(\mathbf{x}_1)\varphi_{k,\sigma_2}^*(\mathbf{x}_2)}{|\mathbf{x}_1 - \mathbf{x}_2|} [\varphi_{j,\sigma_1}(\mathbf{x}_1)\varphi_{k,\sigma_2}(\mathbf{x}_2) - \varphi_{k,\sigma_1}(\mathbf{x}_1)\varphi_{j,\sigma_2}(\mathbf{x}_2)] \right\} \\ &= \sum_j \sum_{\sigma'} \int d^3x' \varphi_{j,\sigma'}^*(\mathbf{x}') \frac{1}{|\mathbf{x} - \mathbf{x}'|} [\varphi_{i,\sigma}(\mathbf{x})\varphi_{j,\sigma'}(\mathbf{x}') - \varphi_{j,\sigma}(\mathbf{x})\varphi_{i,\sigma'}(\mathbf{x}')], \end{aligned} \quad (2.76)$$

and lastly the third term in:

$$-\frac{\delta}{\delta\varphi_{i,\sigma}^*(\mathbf{x})} \left\{ \sum_i \varepsilon_i [\langle \varphi_i | \varphi_i \rangle - 1] \right\} = -\varepsilon_i \varphi_{i,\sigma}(\mathbf{x}). \quad (2.77)$$

Putting all three terms together we arrive at the Hartree-Fock equations:

$$\begin{aligned} \varepsilon_i \varphi_i(\mathbf{x}) = & \left(-\frac{1}{2} \nabla^2 - \sum_n \frac{Z_n}{|\mathbf{x} - \mathbf{R}_n|} \right) \varphi_i(\mathbf{x}) \\ & + \sum_j \int d^3x' \frac{\varphi_j^\dagger(\mathbf{x}') \varphi_j(\mathbf{x}')}{|\mathbf{x} - \mathbf{x}'|} \varphi_i(\mathbf{x}) \\ & - \sum_j \int d^3x' \frac{\varphi_j^\dagger(\mathbf{x}') \varphi_i(\mathbf{x}')}{|\mathbf{x} - \mathbf{x}'|} \varphi_j(\mathbf{x}), \end{aligned} \quad (2.78)$$

where the second and third term are respectively called the *direct* and the *exchange* interaction. The Hartree-Fock equations are integro-differential equations which are solved self-consistently. This refers to filling in some guess for the orbital $\varphi_i(\mathbf{x})$, determining how well it obeys the Hartree-Fock equations, refining the guess to a better one, and iterating this procedure until it converges (if it converges). Once the occupied orbitals $\varphi_i(\mathbf{x})$ are known, we can apply the same equations, with $i \rightarrow a$ to determine the unoccupied (virtual) orbitals $\varphi_a(\mathbf{x})$. Comparing Eq. (2.65) to the Hartree-Fock equations, we have found an expression for the one-body operator $\hat{V} = \sum_{p,q} \hat{c}_p^\dagger \hat{c}_q \bar{V}_{pq}$, with

$$\bar{V}_{pq} = \sum_i v_{pi[qi]}. \quad (2.79)$$

The exchange term in Eq. (2.78) implies that solving this equation can be very computationally costly due to its nonlocal nature. An approximation for the exchange term, only involving local terms, can be made with Slater's simplification. It is obtained after applying the Hartree-Fock equations to the electron gas and determining the exchange interaction for it. The average exchange energy per electron then takes on the compact form:

$$\bar{V}_{exc} = -\frac{3}{2} \left(\frac{3}{\pi} \rho(\mathbf{x}) \right)^{1/3}, \quad (2.80)$$

where $\rho(\mathbf{x}) = \langle \Phi_0^N | \hat{\psi}^\dagger(\mathbf{x}) \hat{\psi}(\mathbf{x}) | \Phi_0^N \rangle = \sum_i \varphi_i^\dagger(\mathbf{x}) \varphi_i(\mathbf{x})$ is the electron density of the system. This approximation leads to the Hartree-Fock-Slater equa-

tions:

$$\begin{aligned}
\varepsilon_i \varphi_i(\mathbf{x}) &= \left(-\frac{1}{2} \nabla^2 - \sum_n \frac{Z_n}{|\mathbf{x} - \mathbf{R}_n|} \right) \varphi_i(\mathbf{x}) \\
&\quad + \int d^3x' \frac{\rho(\mathbf{x}')}{|\mathbf{x} - \mathbf{x}'|} \varphi_i(\mathbf{x}) \\
&\quad - \frac{3}{2} \left(\frac{3}{\pi} \rho(\mathbf{x}) \right)^{1/3} \varphi_i(\mathbf{x}) \\
&\equiv \hat{H}_{\text{HFS}} \varphi_i(\mathbf{x}).
\end{aligned} \tag{2.81}$$

It is computationally favourable to use this approximation as the exchange interaction in the Hartree-Fock equations. The Hartree-Fock-Slater equations [Eq. (2.81)] will be used throughout this thesis to calculate the electronic structure. They are solved self-consistently as mentioned previously. The spin orbitals $\varphi_i(\mathbf{x})$ will be calculated on a radial grid, and are henceforth referred to as $\varphi_i(\mathbf{r})$. They are expanded with respect to spherical harmonics $Y_{lm}(\Omega_{\mathbf{r}})$:

$$\varphi_i(\mathbf{r}) = \varphi_{nlms}(\mathbf{r}) = \frac{u_{nl}(r)}{r} Y_{lm}(\Omega_{\mathbf{r}}) \begin{pmatrix} \delta_{s,1/2} \\ \delta_{s,-1/2} \end{pmatrix}, \tag{2.82}$$

where n , l , m , and s denote the principal, azimuthal, magnetic, and spin quantum numbers. In addition, $r = |\mathbf{r}|$, and $\Omega_{\mathbf{r}}$ denotes the angular part of \mathbf{r} . Plugging this expansion into the Schrödinger equation [Eq. (2.24)] yields the radial Schrödinger equation for a given l :

$$\left[-\frac{1}{2} \frac{d^2}{dr^2} + \frac{l(l+1)}{2r^2} + V(r) \right] u_{nl}(r) = \varepsilon_{nl} u_{nl}(r). \tag{2.83}$$

To reiterate: after identifying the physics we wish to capture in our many-electron description with Eq. (2.46), we used the method of canonical quantization to identify the correct Hamiltonian operator \hat{H}_{matter} [Eq. (2.63)], and canonically conjugate variables $\psi(\mathbf{x})$ and $\psi^\dagger(\mathbf{x})$. Subsequently, we performed a mode expansion of the latter two in a complete, enumerable orthonormal basis, $\varphi_p(\mathbf{x})$, of L^2 -Hilbert space, allowing us to define fermionic annihilation and creation operators \hat{c}_p and \hat{c}_p^\dagger . After assuming the basis functions $\varphi_p(\mathbf{x})$ to be spin orbitals obeying Eq. (2.65), we approximated \hat{H}_{matter} as a one-body Hamiltonian $\hat{\hat{H}}$, which has the spin orbitals $\varphi_p(\mathbf{x})$ as eigenfunctions. To minimize the error of this approximation, the variational principle was used to arrive at the Hartree-Fock equations [Eq. (2.78)], thereby deriving a form for the mean-field potential $\hat{\hat{V}}$ [Eq. (2.79)]. Finally, a further simplification was given for the exchange term, thereby arriving at the Hartree-Fock-Slater equations [Eq. (2.81)]. These equations are numerically solved self-consistently on a radial grid.

2.4 Transition rates

Having gone through the formalism of the electronic-structure calculations used in this thesis, let us proceed by incorporating the description of transitions. We will begin with an exposition on time evolution in quantum mechanics.

2.4.1 Time-dependent perturbation theory

In (non-relativistic) quantum mechanics, time is not an observable, but a parameter, and has no operator associated to it. Time and space are not treated on an equal footing and, instead, the Newtonian concept of time being an absolute background entity is invoked. In this formalism, all observables are a function of time as an external parameter. However, we may introduce a time-*evolution* operator $\hat{U}(t, t_0)$ which evolves a particle's wave function from t_0 to t , with $t \geq t_0$, i.e.,

$$\Psi(\mathbf{x}, t) = \hat{U}(t, t_0)\Psi(\mathbf{x}, t_0). \quad (2.84)$$

The time-evolution operator satisfies some easily proveable properties:

- $\hat{U}(t_0, t_0) = 1$,
- $\hat{U}(t, t')\hat{U}(t', t_0) = \hat{U}(t, t_0)$, for $t \geq t' \geq t_0$,
- $i(d\hat{U}(t, t_0)/dt) = \hat{H}\hat{U}(t, t_0)$, which can be obtained after introducing $\psi(t) = \hat{U}(t, t_0)\psi(t_0)$ into Eq. (2.23),
- $\hat{U}(t_0, t) = \hat{U}^{-1}(t, t_0)$,
- $\hat{U}^\dagger(t, t_0)\hat{U}(t, t_0) = \mathbf{1}$, i.e., the time-evolution operator is unitary. This property follows from the fact that the normalization of states should not be time dependent.

Using the third property, we can find an explicit form of the time-evolution operator $\hat{U}(t, t_0)$ self-consistently. Integrating the expression from t_0 to t on both sides yields

$$\hat{U}(t, t_0) = \mathbf{1} - i \int_{t_0}^t dt_1 \hat{H}(t_1) \hat{U}(t_1, t_0). \quad (2.85)$$

Substituting the left hand side of this equation into the right hand side, we obtain:

$$\begin{aligned} \hat{U}(t, t_0) &= \mathbf{1} - i \int_{t_0}^t dt_1 \hat{H}(t_1) \\ &\quad + (-i)^2 \int_{t_0}^t dt_1 \hat{H}(t_1) \int_{t_0}^{t_1} dt_2 \hat{H}(t_2) \hat{U}(t_2, t_0), \end{aligned} \quad (2.86)$$

with $t_1 > t_2$. This can be iterated further, with $t_1 > t_2 > \dots > t_n$, yielding

$$\begin{aligned}\hat{U}(t, t_0) &= \sum_{n=0}^{\infty} (-i)^n \int_{t_0}^t dt_1 \dots \int_{t_0}^{t_{n-1}} dt_n \hat{H}(t_1) \dots \hat{H}(t_n) \\ &= \mathcal{T} \left\{ \sum_{n=0}^{\infty} \frac{(-i)^n}{n!} \left(\int_{t_0}^t dt' \hat{H}(t') \right)^n \right\} \\ &= \mathcal{T} \left\{ \exp \left[-i \int_{t_0}^t dt' \hat{H}(t') \right] \right\} = \mathcal{T} e^{-i\hat{H}(t-t_0)},\end{aligned}\quad (2.87)$$

where the last equality is only valid for time-independent Hamiltonians. The time ordering operator \mathcal{T} is defined as

$$\mathcal{T}\{A(t)B(t')\} = \begin{cases} A(t)B(t'), & \text{if } t' > t \\ B(t')A(t), & \text{if } t > t'. \end{cases} \quad (2.88)$$

Having introduced the time-evolution operator, we can define the Schrödinger picture (SP) and the Heisenberg picture (HP). The former assumes that the wave function carries time dependence and evolves in time according to the Schrödinger equation. The latter draws back to the more Newtonian notion of physics, where the aim is to calculate how observables depend on time. In quantum mechanics, this implies that the operators, not the states, should evolve in time. The two pictures are equivalent, as they both share the underlying assumption that the expectation value for any observable \hat{O} is given by $\langle \hat{O}(t) \rangle \equiv \langle \Psi(t) | \hat{O} | \Psi(t) \rangle$. The relation between the two pictures can be made clear through the following definitions:

$$\langle \hat{O}(t) \rangle = \begin{cases} \langle \Psi(0) | \hat{U}^\dagger(t, 0) \left(\hat{O} \right) \hat{U}(t, 0) | \Psi(0) \rangle \equiv \langle \Psi_S(t) | \hat{O}_S | \Psi_S(t) \rangle, & \text{for SP,} \\ \langle \Psi(0) | \left(\hat{U}^\dagger(t, 0) \hat{O} \hat{U}(t, 0) \right) | \Psi(0) \rangle \equiv \langle \Psi_H | \hat{O}_H(t) | \Psi_H \rangle, & \text{for HP,} \end{cases}$$

which allows us to relate the Schrödinger picture to the Heisenberg picture via $\hat{O}_H(t) = e^{+iHt} \hat{O}_S e^{-iHt}$. Taking the time derivative of $\hat{O}_H(t)$ and using the Schrödinger equation, we can find the equation of motion for $\hat{O}_H(t)$:

$$i \frac{d\hat{O}_H(t)}{dt} = [\hat{O}_H(t), \hat{H}]. \quad (2.89)$$

There is a third picture, used to describe interactions, called the interaction picture (IP). In this scenario, the Hamiltonian, \hat{H} , is split up into an unperturbed part \hat{H}_0 and a perturbation \hat{H}' , i.e., $\hat{H} = \hat{H}_0 + \hat{H}'$. In the interaction picture, both the states and the operators evolve in time. The operators \hat{O}_I evolve in time using only the free Hamiltonian \hat{H}_0 , i.e., $\hat{O}_I(t) = e^{iH_0 t} \hat{O} e^{-iH_0 t}$. The inclusion of \hat{H}' is what gives the wave functions a time dependence, in the following manner:

$$\begin{aligned}\langle \hat{O}(t) \rangle &= \langle \Psi(t) | \hat{O} | \Psi(t) \rangle \equiv \langle \Psi_I(t) | e^{iH_0 t} \hat{O} e^{-iH_0 t} | \Psi_I(t) \rangle \\ &= \langle \Psi_I(t) | \hat{O}_I(t) | \Psi_I(t) \rangle,\end{aligned}\quad (2.90)$$

where we defined $|\Psi_I(t)\rangle = e^{iH_0t}|\Psi(t)\rangle$, with $|\Psi(t)\rangle$ being the wave function in the Schrödinger picture. We can then use the Schrödinger equation to obtain the equation of motion for $|\Psi_I(t)\rangle$:

$$\begin{aligned} i\frac{d}{dt}|\Psi_I(t)\rangle &= e^{iH_0t}(-\hat{H}_0 + i\frac{d}{dt})|\Psi(t)\rangle \\ &= e^{iH_0t}(-\hat{H}_0 + \hat{H})|\Psi(t)\rangle \\ &= e^{iH_0t}\hat{H}'e^{-iH_0t}|\Psi_I(t)\rangle \equiv \hat{H}'_I(t)|\Psi_I(t)\rangle. \end{aligned} \quad (2.91)$$

For evolving a state in time in the IP, we need a time-evolution operator in the IP, $\hat{U}_I(t, t_0)$, so that $|\Psi_I(t)\rangle = \hat{U}_I(t, t_0)|\Psi_I(t_0)\rangle$. From $|\Psi_I(t)\rangle = e^{iH_0t}|\Psi(t)\rangle$ and Eq. (2.91), $\hat{U}_I(t, t_0)$ obeys

$$i\frac{d\hat{U}_I(t, t_0)}{dt} = \hat{H}'_I(t)\hat{U}_I(t, t_0). \quad (2.92)$$

This can be solved for $\hat{U}_I(t, t_0)$ self-consistently, similar to what we did before, yielding

$$\begin{aligned} \hat{U}_I(t, t_0) &= \sum_{n=0}^{\infty} (-i)^n \int_{t_0}^t dt_1 \dots \int_{t_0}^{t_{n-1}} dt_n \hat{H}'_I(t_1) \dots \hat{H}'_I(t_n) \\ &= \mathcal{T} e^{-i \int_{t_0}^t dt' \hat{H}'_I(t')}. \end{aligned} \quad (2.93)$$

This expression will prove very useful for the perturbative expansion of the transition rate between two states in the following section.

2.4.2 Fermi's golden rule

With the formalism from Sec. 2.4.1, we may proceed by calculating Fermi's golden rule, which calculates the rate, Γ_{FI} , of a certain transition occurring between two states $|I\rangle$ and $|F\rangle$, induced by a perturbation $\hat{H}'_I(t)$, and approximated to first order. To set up our transition, we start by considering our unperturbed Hamiltonian \hat{H}_0 . We assume that this Hamiltonian has a complete set of eigenstates $|n\rangle$, such that $\hat{H}_0|n\rangle = E_n|n\rangle$. In addition, we assume that the initial state, $|\Psi(t_0)\rangle$ at $t_0 \rightarrow -\infty$ is one of these eigenstates, i.e.:

$$\lim_{t_0 \rightarrow -\infty} |\Psi(t_0)\rangle = |I\rangle, \quad (2.94)$$

with $\langle I|n\rangle = \delta_{I,n}$. Long after the transition has occurred, for times $t \rightarrow \infty$, we assume that the state finds itself in another eigenstate of \hat{H}_0 , i.e.,

$$\lim_{t \rightarrow \infty} |\Psi(t)\rangle = |F\rangle, \quad (2.95)$$

with $\langle F|n\rangle = \delta_{F,n}$ and $\langle F|I\rangle = 0$. We impose that the transition between the states occurred because of the perturbation Hamiltonian \hat{H}' . The perturbation may be explicitly time dependent, but this scenario will not be considered here. We proceed by employing the interaction picture. As before, we define $\hat{H}'_I(t) = e^{i\hat{H}_0 t} \hat{H}' e^{-i\hat{H}_0 t}$, which obeys Eq. (2.91). In the interaction picture, the wave function may be expanded in the basis of eigenstates of \hat{H}_0 , $|\Psi(t)\rangle = \sum_n c_n(t)|n\rangle$, where all time dependence has been attributed to the expansion coefficients. Physically, $|c_n(t)|^2$ denotes the probability of finding the state $|\Psi(t)\rangle$ in the eigenstate $|n\rangle$. Therefore, the probability of a transition occurring from the initial state $|I\rangle$ to the final state $|F\rangle$ is $P_{FI} = |c_F(t)|^2$. The time-evolution operator $\hat{U}_I(t, t_0)$ allows us to identify these coefficients as

$$\begin{aligned} |F\rangle &= \hat{U}_I(t, t_0)|I\rangle \\ &= \sum_n |n\rangle \langle n|\hat{U}_I(t, t_0)|I\rangle, \end{aligned} \quad (2.96)$$

where we used the completeness of the eigenstates $|n\rangle$. This identifies the coefficients as $c_n(t) = \langle n|\hat{U}_I(t, t_0)|I\rangle$ and allows for their perturbative expansion using Eq. (2.93):

$$\begin{aligned} c_n(t) &= \delta_{nI} - i \int_{t_0}^t dt' \langle n|\hat{H}'_I(t')|I\rangle + (-i)^2 \int_{t_0}^t dt' \int_{t_0}^{t'} dt'' \langle n|\hat{H}'_I(t')\hat{H}'_I(t'')|I\rangle + \dots \\ &= c_n^{(0)}(t) + c_n^{(1)}(t) + c_n^{(2)}(t) + \dots, \end{aligned} \quad (2.97)$$

where $c_n^{(m)}(t) \propto O[(\hat{H}')^m]$. Setting $n = F$ in the above equation yields us the coefficient we are interested in. This also immediately reveals that $c_F^{(0)}(t) = 0$ as $\delta_{F,I} = 0$. We will proceed further by restricting ourselves to the first order coefficient and omitting higher order corrections, i.e., $P_{FI} = |c_F(t)|^2 \approx |c_F^{(1)}(t)|^2$, yielding

$$\begin{aligned} c_F^{(1)}(t) &= -i \int_{t_0}^t dt' \langle F|\hat{H}'_I(t')|I\rangle \\ &= -i \int_{t_0}^t dt' \langle F|e^{i\hat{H}_0 t} \hat{H}' e^{-i\hat{H}_0 t}|I\rangle \\ &= -i \int_{t_0}^t dt' \langle F|\hat{H}'|I\rangle e^{i(E_F - E_I)t'}, \end{aligned} \quad (2.98)$$

where E_F and E_I are the eigenvalues associated with $|F\rangle$ and $|I\rangle$, respectively. To proceed, we consider the limit $t \rightarrow \infty$:

$$\begin{aligned} \lim_{t \rightarrow \infty} c_F^{(1)}(t) &= -i \int_0^\infty dt' \langle F|\hat{H}|I\rangle e^{i(E_F - E_I)t'} \\ &= -2\pi i \langle F|\hat{H}|I\rangle \delta(E_F - E_I) \equiv S_{FI}, \end{aligned} \quad (2.99)$$

where we defined the probability amplitude S_{FI} . To calculate $P_{FI} = |S_{FI}|^2$ we use the expression:

$$\begin{aligned} [\delta(E_F - E_I)]^2 &= \delta(E_F - E_I) \lim_{T \rightarrow \infty} \int_{-T/2}^{T/2} \frac{dt}{2\pi} e^{i(E_F - E_I)t} \\ &= \delta(E_F - E_I) \lim_{T \rightarrow \infty} \frac{1}{2\pi} \frac{2 \sin[(E_F - E_I)T/2]}{(E_F - E_I)} \\ &= \delta(E_F - E_I) \lim_{T \rightarrow \infty} \frac{T}{2\pi}, \end{aligned} \quad (2.100)$$

which in turn gives

$$\begin{aligned} P_{FI} &= |S_{FI}|^2 \\ &= \lim_{T \rightarrow \infty} 2\pi T |\langle F | \hat{H}' | I \rangle|^2 \delta(E_F - E_I). \end{aligned} \quad (2.101)$$

The limit $T \rightarrow \infty$ may seem worrisome, but in reality, Eq. (2.100) is already well applicable for times $T \gg (E_F - E_I)^{-1}$. Nevertheless, we may obtain a rate from Eq. (2.101) as $\Gamma_{FI} = P_{FI}/T$, yielding

$$\Gamma_{FI} = 2\pi |\langle F | \hat{H}' | I \rangle|^2 \delta(E_F - E_I), \quad (2.102)$$

which is referred to as Fermi's golden rule.

2.4.3 Electron-impact ionization cross section

In what follows, we will use the obtained rate from Fermi's golden rule to derive the cross section for electron-impact ionization. The cross section provides an estimate for how likely a considered scattering process is to occur. Classically, the cross section is the two-dimensional area of an object projected onto the plane perpendicular to the direction of the incoming projectile. When considering the quantum regime however, some aspects that do not occur classically due to the wave nature of quantum particles need to be taken into account. The rate, Γ , at which a certain scattering process occurs is proportional to how many incident particles interact with the system. The latter is expressed through the luminosity, L , which is the number of incident particles passing per unit area per unit time. The proportionality constant, σ , therefore has the unit of area, and is called the cross section, so that $\Gamma = \sigma L$. One can see that the luminosity and the rate have unchanging definitions with respect to what physical process is being considered, and, moreover, they are easily discernible in experiments. The physics behind the scattering process is confined to the cross section σ .

If one intends to know what the resulting direction of the projectile is after the interaction, one calculates the cross section per unit solid angle, called the differential cross section (DCS), denoted $d\sigma/d\Omega$. In the case of inelastic scattering, one may, in addition, resolve the energy transfer during

the interaction, thereby defining the cross section per unit solid angle and per unit energy, called the doubly differential cross section (DDCS), denoted by $d^2\sigma/(d\Omega dE_{\text{out}})$, where E_{out} is the outgoing energy of the projectile after the scattering. From this definition we have:

$$\sigma = \int dE_{\text{out}} \int_0^{2\pi} d\phi \int_{-1}^{+1} d(\cos \theta) \frac{d^2\sigma}{d\Omega dE_{\text{out}}}. \quad (2.103)$$

The integration limits of the energy integral are dependent on which process is under consideration (e.g., excitations or ionizations). The DDCS can be written as the number of particles scattered per unit time into a solid angle $d\Omega$ in the direction $\hat{r} = \mathbf{r}/r$, with energies between E_{out} and $E_{\text{out}} + dE_{\text{out}}$, divided by the number of incoming particles per unit time and per unit area along the incident direction, with momentum \mathbf{q}_{in} and energy E_{in} . This implies:

$$d^2\sigma = \frac{\mathbf{J}_{\text{out}}(\mathbf{r}, \mathbf{q}_{\text{out}}, E_{\text{out}}) \cdot \hat{r} r^2 d\Omega dE_{\text{out}}}{\mathbf{J}_{\text{in}}(\mathbf{q}_{\text{in}}, E_{\text{in}})}, \quad (2.104)$$

where \mathbf{q}_{out} is the momentum of the scattered particle, and \mathbf{J}_{in} and \mathbf{J}_{out} denote the current density of the incident and scattered particles, respectively, with units of number of particles per unit time per unit area. In the quantum regime, the numerator of Eq. (2.104) is the number of particles that are scattered, per unit time, into a group of states in a phase-space volume of d^3q_{out} around \mathbf{q}_{out} . This number of states dn that have a momentum with a magnitude in the range $[\mathbf{q}_{\text{out}}, \mathbf{q}_{\text{out}} + d\mathbf{q}_{\text{out}}]$ is equal to the momentum space volume d^3q_{out} divided by the average volume occupied by a single state, $(2\pi)^3/V$, with V being the volume to which the wave functions of the considered particles is normalized. Thus:

$$\begin{aligned} dn &= d^3q_{\text{out}} \frac{V}{(2\pi)^3} \\ &= q_{\text{out}}^2 dq_{\text{out}} d\Omega \frac{V}{(2\pi)^3}. \end{aligned} \quad (2.105)$$

The number of particles being scattered per unit time is the number of incident particles N_{in} times the rate, $\Gamma_{FI}(\mathbf{q}_{\text{in}} \rightarrow \mathbf{q}_{\text{out}})$, that corresponds to a transition from state $|I, \mathbf{q}_{\text{in}}\rangle$ to a state $|F, \mathbf{q}_{\text{out}}\rangle$ with an exchange in momentum $\mathbf{q}_{\text{in}} \rightarrow \mathbf{q}_{\text{out}}$. However, for a statistical ensemble, this needs to be multiplied by the probability, P_I , of finding target in the initial $|I\rangle$, and summed over all possible initial states. For a canonical ensemble at thermal equilibrium, this probability is given by $P_I = e^{-\beta E_I}/Z$, with $Z = \sum_J e^{-\beta E_J}$, and β the reciprocal temperature of the system (see Sec. 2.5.1). With this, the numerator of Eq. (2.104) is given by:

$$N_{\text{in}} \frac{V}{(2\pi)^3} \sum_I P_I \Gamma_{FI}(\mathbf{q}_{\text{in}} \rightarrow \mathbf{q}_{\text{out}}) q_{\text{out}}^2 d\Omega dq_{\text{out}}, \quad (2.106)$$

which explicitly shows that the DDCS can be obtained from the rate $\Gamma_{FI}(\mathbf{q}_{\text{in}} \rightarrow \mathbf{q}_{\text{out}})$.

Let us now consider the process of electron-impact ionization. We will start by calculating the rate of this process, $\Gamma_{FI}(\mathbf{q}_{\text{in}} \rightarrow \mathbf{q}_{\text{out}})$, by using Fermi's golden rule [Eq. (2.102)]. We assume that before scattering, the incident electron and the target system do not interact, such that

$$|I, \mathbf{q}_{\text{in}}\rangle = |I\rangle|\mathbf{q}_{\text{in}}\rangle, \quad \text{and} \quad |F, \mathbf{q}_{\text{out}}\rangle = |F\rangle|\mathbf{q}_{\text{out}}\rangle, \quad (2.107)$$

where $|I\rangle$ and $|F\rangle$ describe the initial and final system of the many-electron target system, which are eigenstates of the unperturbed Hamiltonian, assumed to be the Hartree-Fock-Slater (HFS) Hamiltonian [Eq. (2.81)]. The initial and the final state of the projectile electron (referred to as the incoming or incident electron and the scattered or outgoing electron, respectively) are modeled as plane waves, denoted by $|\mathbf{q}_{\text{in}}\rangle$ and $|\mathbf{q}_{\text{out}}\rangle$, with corresponding energies $E_{\text{in}} = \mathbf{q}_{\text{in}}^2/2$ and $E_{\text{out}} = \mathbf{q}_{\text{out}}^2/2$. Their description as plane waves is justified due to the following reason. The interaction Hamiltonian, treated as a perturbation which induces the ionization, describes the Coulomb interaction between a single incoming electron, at position \mathbf{x} , and the electrons in the target. It is given in second quantization by:

$$\begin{aligned} \hat{H}' &= \int d^3x' \hat{\psi}^\dagger(\mathbf{x}') \frac{1}{|\mathbf{x} - \mathbf{x}'|} \hat{\psi}(\mathbf{x}') \\ &= \int d^3x' \frac{\hat{n}(\mathbf{x}')}{|\mathbf{x} - \mathbf{x}'|}, \end{aligned} \quad (2.108)$$

where we used the expression for the electron density operator $\hat{n}(\mathbf{x}') = \hat{\psi}^\dagger(\mathbf{x}')\hat{\psi}(\mathbf{x}')$. Treating the Coulomb interaction between the many-electron target and the incident electron as a perturbation is equivalent to imposing that our incident electron has a large kinetic energy compared to this interaction potential energy. Working under this assumption justifies the approximation of modeling the incoming electron as a plane wave. Having modeled the outgoing electron as a plane wave as well implies that the energy transfer during the ionization process is assumed to be small in comparison to the kinetic energy of the incoming electron. As a result, our rate $\Gamma_{FI}(\mathbf{q}_{\text{in}} \rightarrow \mathbf{q}_{\text{out}})$ is given by:

$$\begin{aligned} \Gamma_{FI}(\mathbf{q}_{\text{in}} \rightarrow \mathbf{q}_{\text{out}}) &= 2\pi\delta((E_F + E_{\text{out}}) - (E_I + E_{\text{in}})) \\ &\times \left| \langle F | \langle \mathbf{q}_{\text{out}} | \int d^3x' \frac{\hat{n}(\mathbf{x}')}{|\mathbf{x} - \mathbf{x}'|} | \mathbf{q}_{\text{in}} \rangle | I \rangle \right|^2. \end{aligned} \quad (2.109)$$

By writing out the plane waves $|\mathbf{q}_{\text{in}}\rangle = e^{i\mathbf{q}_{\text{in}} \cdot \mathbf{x}}/\sqrt{V}$ and $|\mathbf{q}_{\text{out}}\rangle = e^{i\mathbf{q}_{\text{out}} \cdot \mathbf{x}}/\sqrt{V}$

and defining $\mathbf{Q} = \mathbf{q}_{\text{in}} - \mathbf{q}_{\text{out}}$ and $\omega = E_{\text{in}} - E_{\text{out}}$, this becomes

$$\Gamma_{FI}(\mathbf{q}_{\text{in}} \rightarrow \mathbf{q}_{\text{out}}) = \frac{2\pi}{V^2} \delta(E_F - E_I - \omega) \times \left| \langle F | \int_V d^3x \int_V d^3x' \frac{\hat{n}(\mathbf{x}')}{|\mathbf{x} - \mathbf{x}'|} e^{i\mathbf{Q} \cdot \mathbf{x}} | I \rangle \right|^2. \quad (2.110)$$

Let us focus on the integral inside the matrix element, i.e.,

$$\int_V d^3x \int_V d^3x' \frac{\hat{n}(\mathbf{x}')}{|\mathbf{x} - \mathbf{x}'|} e^{i\mathbf{Q} \cdot \mathbf{x}} = \int_V d^3x' \hat{n}(\mathbf{x}') e^{i\mathbf{Q} \cdot \mathbf{x}'} \int_V d^3x \frac{e^{i\mathbf{Q} \cdot (\mathbf{x} - \mathbf{x}')}}{|\mathbf{x} - \mathbf{x}'|}. \quad (2.111)$$

Performing the integral over d^3x results in $4\pi/Q^2$, as:

$$\begin{aligned} \int_V d^3x \frac{e^{i\mathbf{Q} \cdot (\mathbf{x} - \mathbf{x}')}}{|\mathbf{x} - \mathbf{x}'|} &= \int_V d^3(x - x') \frac{e^{i\mathbf{Q} \cdot (\mathbf{x} - \mathbf{x}')}}{|\mathbf{x} - \mathbf{x}'|} \\ &\equiv \int_V d^3(r) \frac{e^{i\mathbf{Q} \cdot \mathbf{r}}}{r} \\ &= 2\pi \int_0^\infty dr r \int_{-1}^1 d(\cos \theta) e^{iQr \cos \theta} \\ &= \frac{4\pi}{Q} \int_0^\infty dr \sin(Qr) \\ &= \lim_{a \rightarrow 0^-} \frac{4\pi}{Q} \int_0^\infty dr \sin(Qr) e^{ar} \\ &= \frac{4\pi}{Q} \lim_{a \rightarrow 0^-} \frac{Q}{Q^2 + a^2} = \frac{4\pi}{Q^2}. \end{aligned} \quad (2.112)$$

This reduces the integral to:

$$\begin{aligned} \int_V d^3x \int_V d^3x' \frac{\hat{n}(\mathbf{x}')}{|\mathbf{x} - \mathbf{x}'|} e^{i\mathbf{Q} \cdot \mathbf{x}} &= \frac{4\pi}{Q^2} \int_V d^3x' \hat{n}(\mathbf{x}') e^{i\mathbf{Q} \cdot \mathbf{x}'} \\ &= \frac{4\pi}{Q^2} \hat{n}(-\mathbf{Q}) = \frac{4\pi}{Q^2} \hat{n}^\dagger(\mathbf{Q}). \end{aligned} \quad (2.113)$$

Collecting all results, we have:

$$\begin{aligned} d^2\sigma &= \frac{V}{(2\pi)^3} N_{\text{in}} \frac{\sum_I P_I \Gamma_{FI}(\mathbf{q}_{\text{in}} \rightarrow \mathbf{q}_{\text{out}}) q_{\text{out}}^2 d\Omega dq_{\text{out}}}{\mathbf{J}_{\text{in}}(\mathbf{q}_{\text{in}}, E_{\text{in}})} \\ &= \frac{V^2}{(2\pi)^3} N_{\text{in}} \frac{\sum_I P_I \Gamma_{FI}(\mathbf{q}_{\text{in}} \rightarrow \mathbf{q}_{\text{out}}) q_{\text{out}} d\Omega dE_{\text{out}}}{N_{\text{in}} q_{\text{in}}}, \end{aligned} \quad (2.114)$$

where we used $\mathbf{J}_{\text{in}}(\mathbf{q}_{\text{in}}, E_{\text{in}}) = N_{\text{in}} q_{\text{in}}/V$ and $dq_{\text{out}} = dE_{\text{out}}/q_{\text{out}}$. Proceeding

further with the calculation of the DDCS, we have

$$\begin{aligned}
\frac{d^2\sigma}{d\Omega dE_{\text{out}}} &= \frac{V^2}{(2\pi)^3} \frac{q_{\text{out}}}{q_{\text{in}}} \sum_I P_I \Gamma_{FI}(\mathbf{q}_{\text{in}} \rightarrow \mathbf{q}_{\text{out}}) \\
&= \frac{V^2}{(2\pi)^3} \frac{q_{\text{out}}}{q_{\text{in}}} \sum_I P_I \frac{2\pi}{V^2} \delta(E_F - E_I - \omega) \left| \langle F | \frac{4\pi}{Q^2} \hat{n}^\dagger(\mathbf{Q}) | I \rangle \right|^2 \\
&= \frac{4}{Q^4} \frac{q_{\text{out}}}{q_{\text{in}}} \sum_I P_I \left| \langle F | \hat{n}^\dagger(\mathbf{Q}) | I \rangle \right|^2 \delta(E_F - E_I - \omega). \quad (2.115)
\end{aligned}$$

In order to actually calculate the DDCS, we need to consider the initial and final state, $|I\rangle$ and $|F\rangle$ of the many-electron system that acts as our target. As they are eigenstates of the HFS Hamiltonian, we can assume that the initial states, $|I\rangle$, being thermally averaged over, are Fock states:

$$|I\rangle = |\{N_{\text{el}}\}\rangle = \prod_{p=1}^{N_{\text{el}}} \hat{c}_p^\dagger |0\rangle, \quad (2.116)$$

where N_{el} denotes the number of electrons present in the initial state. If we neglect all correlations between the ejected electron and the remaining electrons in the parent ion, we may approximate the final state as

$$|F\rangle = \hat{c}_F^\dagger \hat{c}_I |\{N_{\text{el}}\}\rangle. \quad (2.117)$$

Thus, the matrix element is transformed into

$$\begin{aligned}
\langle F | \hat{n}^\dagger(\mathbf{Q}) | I \rangle &= \langle \{N_{\text{el}}\} | \hat{c}_I^\dagger \hat{c}_F \int d^3x \hat{n}(\mathbf{x}) e^{i\mathbf{Q}\cdot\mathbf{x}} | \{N_{\text{el}}\} \rangle \\
&= \sum_{p,q} \langle \varphi_p | e^{i\mathbf{Q}\cdot\mathbf{x}} | \varphi_q \rangle \langle \{N_{\text{el}}\} | \hat{c}_I^\dagger \hat{c}_F \hat{c}_p^\dagger \hat{c}_q | \{N_{\text{el}}\} \rangle, \quad (2.118)
\end{aligned}$$

where we expanded the density operator with respect to our spin orbitals as $\hat{n}(\mathbf{x}) = \sum_{p,q} \varphi_p^\dagger(\mathbf{x}) \varphi_q(\mathbf{x}) \hat{c}_p^\dagger \hat{c}_q$. We can see that the matrix element with respect to Fock states will only be nonzero only if: (i) $I = q$, resulting in $F = p$, or (ii) if $I \neq q$, resulting in $p = q$ and $I = F$. This last case we are not considering here. Therefore,

$$\begin{aligned}
\langle F | \hat{n}^\dagger(\mathbf{Q}) | I \rangle &= \sum_{I,F} \langle \varphi_F | e^{i\mathbf{Q}\cdot\mathbf{x}} | \varphi_I \rangle \langle \{N_{\text{el}}\} | \hat{c}_I^\dagger \hat{c}_F \hat{c}_F^\dagger \hat{c}_I | \{N_{\text{el}}\} \rangle \\
&= \sum_{I,F} \langle \varphi_F | e^{i\mathbf{Q}\cdot\mathbf{x}} | \varphi_I \rangle \langle \{N_{\text{el}}\} | \hat{n}_I (1 - \hat{n}_F) | \{N_{\text{el}}\} \rangle, \quad (2.119)
\end{aligned}$$

where we used the anticommutation relations between \hat{c} and \hat{c}^\dagger [Eq. (2.60)].

This expresses the DDCCS in Eq. (2.115) with respect to the spin orbitals as

$$\begin{aligned}
\frac{d^2\sigma}{d\Omega dE_{\text{out}}} &= \frac{4}{Q^4} \frac{q_{\text{out}}}{q_{\text{in}}} \sum_I P_I \left| \langle F | \hat{n}^\dagger(\mathbf{Q}) | I \rangle \right|^2 \delta(E_F - E_I - \omega) \\
&= \frac{4}{Q^4} \frac{q_{\text{out}}}{q_{\text{in}}} \sum_{\{N_{\text{el}}\}} P_{\{N_{\text{el}}\}} \sum_{I,F} n_I^{\{N_{\text{el}}\}} (1 - n_F^{\{N_{\text{el}}\}}) \\
&\quad \times \left| \langle \varphi_F | e^{i\mathbf{Q} \cdot \mathbf{x}} | \varphi_I \rangle \right|^2 \delta(\varepsilon_F - \varepsilon_I - \omega) \\
&= \frac{4}{Q^4} \frac{q_{\text{out}}}{q_{\text{in}}} \sum_{I,F} \bar{n}_I (1 - \bar{n}_F) \left| \langle \varphi_F | e^{i\mathbf{Q} \cdot \mathbf{x}} | \varphi_I \rangle \right|^2 \delta(\varepsilon_F - \varepsilon_I - \omega),
\end{aligned} \tag{2.120}$$

where we defined the eigenvalue of the density operator with respect to the Fock state $|\{N_{\text{el}}\}\rangle$ as $n^{\{N_{\text{el}}\}}$, and the energy eigenvalues of the spin orbitals are denoted as ε . The average number of particles in spin orbital φ , is denoted by \bar{n} and calculated as $\sum_{\{N_{\text{el}}\}} P_{\{N_{\text{el}}\}} n^{\{N_{\text{el}}\}}$.

At this point, the reader has been made familiar with all of the theoretical background used for the work done in Chapter 3.

2.5 Temperature and environment

The final elements to be included in our theoretical framework are the concept of temperature in the quantum theory of a many-electron system, as well as the effects of a periodic crystal structure.

2.5.1 Temperature in quantum mechanics

When discussing many-particle systems, it is natural to consider the temperature, T , (or its reciprocal $\beta = 1/T$). At zero temperature, a physical system occupies its lowest allowed energy configuration. As the temperature is increased, more and more energy is introduced into the system. How this energy is distributed among the particles is characterized by a temperature-dependent probability function, $P(E_i, \beta)$, denoting the probability for given particle having an energy E_i at temperature β .

Let us consider a system of N particles, where N is considered to be “large“, i.e., as typically found in macroscopic systems. This system has a total energy E_{tot} , which, at thermal equilibrium, is a fixed constant. The fundamental assumption of statistical mechanics is that in thermal equilibrium every configuration with the same total energy E_{tot} is equally probable. As a trivial example, consider two particles that can have an energy associated to them of either 0 or 1 (in arbitrary units). The assumption is then that if the total energy is 1, that the configurations (0,1) and (1,0) are equally probable. In our N -particle system ($\sum_{j=1}^{\infty} n_j = N$ for $n_j \in \{0,1\}$)

if the particles are fermions), let us consider a particle that is in a state with energy E_i ($n_i = 1$). The total energy is $E_{\text{tot}} = \sum_{j=1}^{\infty} n_j E_j$. Let $\Omega(E)$ define the number of accessible microstates such that the total energy is E . In our previous example, we have $\Omega(0) = \Omega(2) = 1$ and $\Omega(1) = 2$. The number of microstates for the system minus the particle under consideration is $\Omega(E_{\text{tot}} - E_i)$. However, since that particle is definitely in the state with energy E_i , the number of available microstates for the total system is also $\Omega(E_{\text{tot}} - E_i)$. Now, as all these microstates have the same probability associated to them, we find that the probability of finding our one particle in the state with energy E_i is

$$P_i \sim \Omega(E_{\text{tot}} - E_i) = C\Omega(E_{\text{tot}} - E_i), \quad (2.121)$$

for some proportionality constant C . Using the fact that $E_i \ll E_{\text{tot}}$ (because N is large), we can expand P_i around E_{tot} . However, as we expect P_i to vary rapidly when changing E_i , it is better instead to vary $\ln P_i$:

$$\ln P_i = \ln C + \ln \Omega(E_{\text{tot}}) - \left. \frac{\partial \ln \Omega}{\partial E} \right|_{E=E_{\text{tot}}} E_i + \dots; \quad (2.122)$$

The quantity $\partial \ln \Omega / \partial E|_{E=E_{\text{tot}}} \equiv \beta$ defines the temperature $\beta = 1/T$. Defining another constant $A = C\Omega(E_{\text{tot}})$, we have for P_i

$$P_i = A e^{-\beta E_i}. \quad (2.123)$$

To find A , we simply impose that the probability distribution is normalized, i.e., $\sum_i P_i = 1$, yielding the fundamental result:

$$P_i = \frac{e^{-\beta E_i}}{\sum_i e^{-\beta E_i}} \equiv \frac{e^{-\beta E_i}}{Z}, \quad (2.124)$$

where Z is called the canonical partition function. Recall that this expression was mentioned briefly in Sec 2.4.3 for Eq. (2.106). Note that if E_i is the energy eigenvalue associated with a Hamiltonian \hat{H} , with the eigenfunction $|\psi_i\rangle$, then

$$Z = \sum_i \langle \psi_i | e^{-\beta \hat{H}} | \psi_i \rangle = \text{Tr}[e^{-\beta \hat{H}}] \quad (2.125)$$

The expectation value of some operator \hat{O} with respect to the state $|\psi_i\rangle$ can then be thermally weighted as

$$\langle \hat{O} \rangle_{\beta} = \sum_i P_i \hat{O} = \frac{1}{Z} \sum_i \langle \psi_i | \hat{O} | \psi_i \rangle e^{-\beta E_i} = \frac{1}{Z} \text{Tr}[\hat{O} e^{-\beta \hat{H}}]. \quad (2.126)$$

For completeness, we mention that the statistical ensembles under consideration in this work are canonical ensembles, i.e., where the number of particles

remains fixed in the system, but an exchange in energy with an external heat bath allows for the consideration of temperature.

As an example, let us consider a system with N identical fermions at thermal equilibrium. We assume they are all described by single-particle states, with eigenvalues ε_i , $i \in \{1, \dots, \infty\}$. Let us determine the thermally averaged expectation value for the amount of fermions in a given single-particle state with energy ε_i , called \bar{n}_i , with n_i being the occupancy of the i -th state, i.e., $n_i \in \{0, 1\}$. These satisfy the constraint that the total number of fermions is $N = \sum_{j=1}^{\infty} n_j$. The total system can be in any configuration S , that satisfies this constraint, and has a total energy $E_S = \sum_{j=1}^{\infty} n_j \varepsilon_j$. The probability of finding the system in the total state S is thus

$$\begin{aligned} P_S &= \frac{e^{-\beta E_S}}{\sum_{S'} e^{-\beta E_{S'}}} \\ &= \left(\prod_{j=1}^{\infty} e^{-\beta n_j \varepsilon_j} \right) \left(\sum_{n_1, n_2, \dots} \prod_{j=1}^{\infty} e^{-\beta n_j \varepsilon_j} \right)^{-1}, \end{aligned} \quad (2.127)$$

where

$$\sum_{n_1, n_2, \dots} \equiv \sum_{n_1=0}^1 \sum_{n_2=0}^1 \dots \quad (2.128)$$

Then, by definition:

$$\begin{aligned} \bar{n}_i &= \sum_S n_i P_S \\ &= \left(\sum_{n_1, n_2, \dots} n_i \prod_{j=1}^{\infty} e^{-\beta n_j \varepsilon_j} \right) \left(\sum_{n_1, n_2, \dots} \prod_{j=1}^{\infty} e^{-\beta n_j \varepsilon_j} \right)^{-1} \\ &= \left(\sum_{n_i=0}^1 n_i e^{-\beta n_i \varepsilon_i} \sum_{\substack{n_1, n_2, \dots / n_i \\ j=1 \\ j \neq i}}^1 \prod_{j=1}^{\infty} e^{-\beta n_j \varepsilon_j} \right) \left(\sum_{n_i=0}^1 e^{-\beta n_i \varepsilon_i} \sum_{\substack{n_1, n_2, \dots / n_i \\ j=1 \\ j \neq i}}^1 \prod_{j=1}^{\infty} e^{-\beta n_j \varepsilon_j} \right)^{-1} \\ &\equiv \left(\sum_{n_i=0}^1 n_i e^{-\beta n_i \varepsilon_i} Z_i(N - n_i) \right) \left(\sum_{n_i=0}^1 e^{-\beta n_i \varepsilon_i} Z_i(N - n_i) \right)^{-1} \\ &= \frac{0 + e^{-\beta \varepsilon_i} Z_i(N - 1)}{Z_i(N) + e^{-\beta \varepsilon_i} Z_i(N - 1)} \\ &= \frac{1}{[Z_i(N)/Z_i(N - 1)]e^{-\beta \varepsilon_i} + 1}, \end{aligned} \quad (2.129)$$

where $\sum_{n_1, n_2, \dots / n_i}$ is understood to exclude the contribution of n_i in the

sums, and we defined

$$Z_i(N - n_i) = \sum_{n_1, n_2, \dots, n_i}^1 \prod_{\substack{j=1 \\ j \neq i}}^{\infty} e^{-\beta n_j \varepsilon_j}. \quad (2.130)$$

Again, we will use a Taylor expansion so that

$$\ln Z_i(N - 1) = \ln Z_i(N) - \frac{\partial \ln Z_i(N)}{\partial N}. \quad (2.131)$$

The term $\partial \ln Z_i(N)/\partial N \equiv -\beta\mu$ is what defines the chemical potential μ . One can see that it encompasses the effect of adding or removing a single electron to or from the system to the partition function. Thus we find $Z_i(N)/Z_i(N - 1) = e^{-\beta\mu}$, resulting in

$$\bar{n}_i = \frac{1}{e^{\beta(\varepsilon_i - \mu)} + 1}, \quad (2.132)$$

which is referred to as the Fermi-Dirac factor. From Eq. (2.132) we can deduce that μ represents the energy under which all energy levels have an occupation number of at least 0.5.

2.5.2 Bloch's theorem

The many-electron systems considered in this thesis are both single isolated atoms, as well as crystalline solids. A particularly useful theorem to deal with systems exhibiting a crystal structure is Bloch's theorem. This theorem does assume that correlation effects may be (largely) neglected, which is not always an obvious assumption in the context of solids.

The starting point for deriving Bloch's theorem is the Schrödinger equation in three dimensions:

$$\hat{H}\psi(\mathbf{r}) = \left[-\frac{1}{2}\nabla^2 + V(\mathbf{r}) \right] \psi(\mathbf{r}) = E\psi(\mathbf{r}), \quad (2.133)$$

where $\psi(\mathbf{r})$ represents a single-electron wave function. Given the eigenvalues E_n and eigenfunctions $\psi_n(\mathbf{r})$ of \hat{H} , Eq. (2.133) simply becomes $\hat{H}\psi_n(\mathbf{r}) = E_n\psi_n(\mathbf{r})$. Next, let us assume the electron is located in a crystal, which is comprised of primitive unit cells characterized by primitive lattice vectors \mathbf{a}_i , with $i \in \{1, 2, 3\}$. The volume of one such unit cell is therefore $\Omega = |\mathbf{a}_1 \cdot (\mathbf{a}_2 \times \mathbf{a}_3)|$. The entire crystal is thus made up of copies of these primitive unit cells, translated over lattice vectors $\mathbf{R}_l = n_1\mathbf{a}_1 + n_2\mathbf{a}_2 + n_3\mathbf{a}_3$, with $l = (n_1, n_2, n_3)$ and n_i integers. Therefore, a translation over \mathbf{R}_l leaves the lattice invariant. The translation operator over a lattice vector \mathbf{R}_l is defined as:

$$\hat{T}_{\mathbf{R}_l}\psi_n(\mathbf{r}) = \psi_n(\mathbf{r} + \mathbf{R}_l). \quad (2.134)$$

As the crystal lattice is fixed, the Hamiltonian \hat{H} is invariant under symmetry operations of the crystal, which includes $\hat{T}_{\mathbf{R}_l}$. Therefore:

$$\hat{T}_{\mathbf{R}_l}[\hat{H}\psi_n(\mathbf{r})] = \hat{H}[\hat{T}_{\mathbf{R}_l}\psi_n(\mathbf{r})]. \quad (2.135)$$

However, it also true that:

$$\begin{aligned} \hat{T}_{\mathbf{R}_l}[\hat{H}\psi_n(\mathbf{r})] &= \hat{T}_{\mathbf{R}_l}[E_n\psi_n(\mathbf{r})] \\ &= E_n[\hat{T}_{\mathbf{R}_l}\psi_n(\mathbf{r})], \end{aligned} \quad (2.136)$$

from which it follows that $\psi_n(\mathbf{r})$ and $\hat{T}_{\mathbf{R}_l}\psi_n(\mathbf{r})$ are simultaneous eigenfunctions of \hat{H} with the same eigenvalue E_n .

We need now to distinguish different cases:

- E_n is non-degenerate. Then it only has one associated eigenfunction $\psi_n(\mathbf{r})$. Since $\psi_n(\mathbf{r})$ and $\hat{T}_{\mathbf{R}_l}\psi_n(\mathbf{r})$ are simultaneous eigenfunctions, this implies that the two must be proportional to each other with an overall factor, $\lambda^{(l)}$:

$$\hat{T}_{\mathbf{R}_l}\psi_n(\mathbf{r}) = \lambda^{(l)}\psi_n(\mathbf{r}). \quad (2.137)$$

From the fact that $|\hat{T}_{\mathbf{R}_l}\psi_n(\mathbf{r})|^2 = |\psi_n(\mathbf{r})|^2$, we get that $|\lambda^{(l)}|^2 = 1$. We can thus write it as $\lambda = e^{i\alpha_l}$. Note that $\lambda^{(l)}$ is the eigenvalue of the operator $\hat{T}_{\mathbf{R}_l}$. Next, as $\hat{T}_{\mathbf{R}_l}$ is a symmetry operator, it is an element of the (abelian) symmetry group, obeying the respective group properties. In particular, two lattice vectors \mathbf{R}_l and \mathbf{R}_m can be combined to form a third lattice vector, $\mathbf{R}_p = \mathbf{R}_l + \mathbf{R}_m$. This implies that the operator $\hat{T}_{\mathbf{R}_p} = \hat{T}_{\mathbf{R}_l}\hat{T}_{\mathbf{R}_m}$ has an eigenvalue $e^{i\alpha_p} = e^{i(\alpha_l + \alpha_m)}$. Because of this close connection between α_l and \mathbf{R}_l , it is natural, and convenient, to express α_l in terms of \mathbf{R}_l by multiplication of some vector \mathbf{k} , universal to all α_l , i.e., $\alpha_l = \mathbf{k} \cdot \mathbf{R}_l$.

- E_n is f -fold degenerate. Then E_n has f orthogonal eigenfunctions $\psi_{n,\kappa}(\mathbf{r})$, with $\kappa \in \{1, \dots, f\}$, and $\hat{T}_{\mathbf{R}_l}\psi_{n,\kappa}$ can be represented as a linear combination of $\psi_{n,\kappa}$:

$$\hat{T}_{\mathbf{R}_l}\psi_{n,\kappa} = \sum_{\kappa'=1}^f \lambda_{\kappa,\kappa'}^{(l)} \psi_{n,\kappa'}(\mathbf{r}). \quad (2.138)$$

Again, from $\hat{T}_{\mathbf{R}_l}\hat{T}_{\mathbf{R}_m} = \hat{T}_{\mathbf{R}_p}$, it follows that $\sum_{\kappa'=1}^f \lambda_{\kappa,\kappa'}^{(l)} \lambda_{\kappa'\kappa''}^{(m)} = \lambda_{\kappa,\kappa''}^{(p)}$. Since all translations form a group, its matrix representation (the coefficients $\lambda_{\kappa,\kappa'}^{(l)}$) also forms a group. We can then use the following two lemmas from group theory: 1) an equivalent matrix representation can be made from a linear combination of the $\psi_{n,\kappa}(\mathbf{r})$'s, which just states that the basis chosen to represent the matrix form of $\hat{T}_{\mathbf{R}_l}$

is not unique, and 2) among all equivalent matrix representations of an abelian group, one can always find one so that the matrix is in diagonal form:

$$\begin{aligned}\hat{T}_{\mathbf{R}_l}\psi_{n,\kappa} &= \sum_{\kappa'=1}^f \lambda_{\kappa,\kappa'}^{(l)} \delta_{\kappa,\kappa'} \psi_{n,\kappa'}(\mathbf{r}) \\ &= \lambda_{\kappa,\kappa}^{(l)} \psi_{n,\kappa}(\mathbf{r}).\end{aligned}\quad (2.139)$$

From then on, similar reasoning can be followed, to argue that $|\lambda_{\kappa,\kappa}^{(l)}|^2 = 1$, and thus $\lambda_{\kappa,\kappa}^{(l)} = e^{i\mathbf{k}_\kappa \cdot \mathbf{R}_l}$.

The important conclusion is that for every eigensolution of the Hamiltonian, $\psi_n(\mathbf{r})$, one can always find a vector \mathbf{k} , such that $\psi_n(\mathbf{r})$ is also an eigenfunction of $\hat{T}_{\mathbf{R}_l}$, with eigenvalue $e^{i\mathbf{k} \cdot \mathbf{R}_l}$. Thus, the translational invariance arising from the crystal structure allows for $\psi_n(\mathbf{r})$ to be classified by \mathbf{k} : $\psi_n(\mathbf{r}) \rightarrow \psi_{n,\mathbf{k}}(\mathbf{r})$.

Note that the only assumption made was that ψ_n is an energy eigenstate of a Hamiltonian which is invariant under the symmetry operations of a crystal (with eigenvalue $E_n = E_n(\mathbf{k}) \equiv E_{n,\mathbf{k}}$; where n is referred to as a band index). From that we could conclude:

$$\hat{T}_{\mathbf{R}_l}\psi_{n,\mathbf{k}}(\mathbf{r}) = \psi_{n,\mathbf{k}}(\mathbf{r} + \mathbf{R}_l) = e^{i\mathbf{k} \cdot \mathbf{R}_l} \psi_{n,\mathbf{k}}(\mathbf{r}). \quad (2.140)$$

This illustrates the fundamental result that the behavior of the wave function in any unit cell, and therefore throughout all of space, is captured by the wave function contained within some single reference unit cell. Subsequently, from this result, we can prove that $\psi_{n,\mathbf{k}}(\mathbf{r})$ can be written as a Bloch wave, which is defined as:

$$\psi_{n,\mathbf{k}}(\mathbf{r}) = \frac{1}{\sqrt{V}} e^{i\mathbf{k} \cdot \mathbf{r}} \mu_{n,\mathbf{k}}(\mathbf{r}), \quad (2.141)$$

where $\mu_{n,\mathbf{k}}(\mathbf{r} + \mathbf{R}_l) = \mu_{n,\mathbf{k}}(\mathbf{r})$ is a lattice periodic function, and the volume V was introduced to impose periodic boundary conditions. The proof goes as follows:

$$\begin{aligned}\mu_{n,\mathbf{k}}(\mathbf{r} + \mathbf{R}_l) &= \sqrt{V} e^{-i\mathbf{k} \cdot (\mathbf{r} + \mathbf{R}_l)} \psi_{n,\mathbf{k}}(\mathbf{r} + \mathbf{R}_l) \\ &= \sqrt{V} e^{-i\mathbf{k} \cdot \mathbf{r}} e^{-i\mathbf{k} \cdot \mathbf{R}_l} e^{i\mathbf{k} \cdot \mathbf{R}_l} \psi_{n,\mathbf{k}}(\mathbf{r}) \\ &= \sqrt{V} e^{-i\mathbf{k} \cdot \mathbf{r}} \psi_{n,\mathbf{k}}(\mathbf{r}) \\ &= \mu_{n,\mathbf{k}}(\mathbf{r}).\end{aligned}\quad (2.142)$$

We may subsequently conclude Bloch's theorem: The non-degenerate solutions of the Schrödinger equation, as well as a suitably chosen linear combination of degenerate solutions (to make the λ -matrix diagonal) are simultaneous eigenfunctions of all translation operators, as well as of the

Hamiltonian. They can then be written in the form given in Eq. (2.141). Finally, the physical interpretation of the vector \mathbf{k} is that it is the electron's wave vector. This can be seen by considering Eq. (2.141) with an "empty lattice", i.e., setting μ equal to a constant. Then the electron's wavefunction is $\propto e^{i\mathbf{k}\cdot\mathbf{r}}$, i.e., a plane wave, from which it follows that \mathbf{k} must be interpreted as the electron's wave vector.

The usefulness of the Bloch theorem becomes clear by realizing that any periodic function can be expressed as a Fourier series, i.e.,

$$\mu_{n,\mathbf{k}}(\mathbf{r}) = \sum_m v_{n,\mathbf{k}}(\mathbf{K}_m) e^{i\mathbf{K}_m \cdot \mathbf{r}} \quad (2.143a)$$

$$v_{n,\mathbf{k}}(\mathbf{K}_m) = \frac{1}{\Omega} \int_{\Omega} d^3r e^{-i\mathbf{K}_m \cdot \mathbf{r}} \mu_{n,\mathbf{k}}(\mathbf{r}), \quad (2.143b)$$

where $v_{n,\mathbf{k}}(\mathbf{K}_m)$ is a Fourier coefficient and the vectors \mathbf{K}_m are reciprocal lattice vectors. They have the property that $\mathbf{K}_m \cdot \mathbf{R}_l = 2\pi N$, with N being an integer, which is a consequence of the periodicity of $\mu_{n,\mathbf{k}}(\mathbf{r})$. The reciprocal space (\mathbf{k} space) associated with the real-space lattice is itself a lattice. The equivalent of the primitive unit cell in reciprocal space is called the first Brillouin zone. Due to the periodicity exhibited by the lattice in \mathbf{k} space, \mathbf{k} -dependent quantities that extend beyond the first Brillouin zone may be captured through higher-lying bands within the same first Brillouin zone.

This concludes the elaboration on the employed theoretical framework. With the elements explained in this chapter, the reader should have a comfortable theoretical foundation from which the original work in the upcoming chapters is based on.

Chapter 3

Ab initio calculation of electron-impact-ionization cross sections for ions in exotic electron configurations

This Chapter reflects the work done in the article [1], of which I am the first author, and has been included verbatim:

BEKX, SON, SANTRA, ZIAJA, Phys. Rev. A **98**, 022701 (2018).

Copyright (2018) by the American Physical Society. Reproduced with permission of the American Physical Society for the purpose of this thesis.

Abstract

Atomic or molecular assemblies irradiated with intense hard x-ray pulses, such as those emitted from x-ray free-electron lasers (XFELs), are subject to a strong ionization, which also releases electrons from atomic inner shells. The resulting core-hole states relax via various channels, including fluorescence and Auger decay. The latter is the predominant relaxation channel for light elements and typically occurs on a time scale of 1-10 fs. In dense samples, the core-hole ions may already undergo electron-impact ionizations during this time due to the abundance of highly energetic photoelectrons and Auger electrons. In this study we perform an *ab initio* calculation of the electron-impact-ionization cross sections of ions with an arbitrary electronic configuration at zero temperature. This allows us to evaluate and compare impact-ionization cross sections for ions in ground and “exotic” electronic states (e.g., with a few core holes), which may be formed during their interaction with intense x-ray pulses. We show that the impact-ionization cross sections for ions of the same charge, but with varying electronic configura-

tions, may significantly differ. This finding has to be taken into account in any modeling tool treating the relaxation of atoms after high-energy-impact collision, e.g., simulations dedicated for coherent x-ray diffraction imaging of nanocrystals and single biological macromolecules, or laser-created plasma studies. Our computationally efficient *ab initio* calculation scheme can be easily incorporated in such simulation schemes.

3.1 Introduction

Within the last decade, the advent of x-ray free-electron lasers (XFELs) [10–12,14,15] has provided novel insights for the study of x-ray–matter interactions. Applications of this knowledge range over various different scientific fields, including atomic and molecular physics [17–20], astrophysics [30], plasma physics [34], and structural biology [21–25].

In particular, XFELs provide ultrashort and ultraintense pulses of x rays, shaping new avenues in x-ray crystallography [31,32]. Three-dimensional determination of biomolecular structures is vital for studying biological functions of these macromolecules. Molecular structures of biomolecules are reconstructed from x-ray scattering patterns. In order to ensure a sufficiently strong scattering signal, the patterns are typically obtained from coherent diffraction on a crystal formed from the macromolecule. However, growing the high-quality crystals is a difficult and sometimes even an impossible task [78]. Instead, the high fluence from the XFEL can be exploited in order to generate a sufficiently strong scattering signal from nanocrystals [22] and single bioparticles [23]. At the same time, such a high fluence induces a rapidly progressing damage of the sample. In order to overcome this issue, the XFEL pulse duration should be sufficiently short (≤ 10 fs) to outrun the nuclear damage. This scheme is called “diffraction before destruction.” However, currently available XFEL pulses are not short enough to elude electronic motion and the subsequently induced electronic damage [38]. Therefore, quantitative understanding of the radiation damage mechanisms, as well as their proper treatment and incorporation into simulations, is vital for the accuracy of the structure determination from experimental data [38–43]. Such incorporation of radiation damage into photon–matter interaction studies has been done, e.g., with the molecular dynamics code XMDYN [79, 80]. Based on a combination of atomistic calculation and classical molecular dynamics, XMDYN provides microscopic simulations of x-ray-induced dynamics of clusters [81], nanocrystals [42], and solid-density matter [82] in connection with x-ray molecular imaging [83].

While interacting with the imaged sample, hard x rays predominantly excite inner-shell electrons. The resulting core-hole states can decay via various paths, including fluorescence and Auger decay. The latter is the predominant relaxation channel for light elements, and typically takes place

within 1-10 fs [43, 84] after a photoionizing event. At this timescale, in materials dense enough, the core-hole ions may also undergo electron-impact ionization, due to the abundance of highly energetic photoelectrons and Auger electrons.

The importance of impact ionization in radiation damage has been demonstrated not only in connection with x-ray imaging [37, 38], but also for electron diffraction [85, 86] and plasma studies [34, 87]. This ionization process has been extensively studied over many years [44–47]. The accuracy of theoretical methods used for the determination of the electron-impact-ionization cross sections depends both on the wave-function description used to describe the incoming and outgoing electrons, as well as on the collision theory employed. A concise overview can be found in Refs. [48] and [49]. Semiempirical approaches and simplified formulas are also frequently used to determine electron-impact-ionization cross sections, such as the semiempirical formula by Lotz [88–91] and the binary-encounter-Bethe (BEB) formula [92]. The latter method has also been extended to the relativistic regime [93, 94].

Here, we intend to describe electron-impact ionization of an ion with any excited electronic configuration which may occur as the result of its exposure to high-intensity x rays. Such cases are not accounted for accurately in semiempirical formulas due to the lack of experimental data on the electron-impact ionization of excited ions. In this paper, we provide an *ab initio* calculation of the electron-impact-ionization cross sections for such ions at zero temperature. In our framework, the impact electron before and after the scattering process is modeled as a plane wave. The target ion, as well as the ejected electron after the scattering process, is treated within a Hartree-Fock-Slater framework, with free states approximated by a discrete pseudocontinuum. With this approach, it is assumed that the outgoing scattered electron and the ejected electron are distinguishable.

The paper is structured as follows: In Sec. 3.2 we extend the electronic structure calculation code, XATOM [43, 79, 95], in order to implement the doubly differential electron-impact-ionization cross section (DDCS) within this scheme. From the DDCS, singly differential (DCS) and total cross sections (CS) are obtained. In Sec. 3.3 we calculate the DDCS for an incoming electron of 1 keV energy interacting with a double core-hole ($1s^{-2}$) carbon (+2) ion, as well as the angle- and energy-resolved DCS for the same system. For the total cross-section studies, we consider various electronic configurations of carbon (+), carbon (+2), and sulfur (+8) ions, including their ground states. The results are compared with the available experimental data and other theory models (Lotz and BEB schemes). The section is concluded with a discussion. Section 3.4 provides a conclusion and an outlook.

3.2 Theoretical and numerical framework

We start with a clarification of terminology. While discussing the process of electron-impact ionization, we consider the *incoming electron*, which, after the scattering process, becomes the *outgoing (scattered) electron*, and the *electron ejected* from the system.

Throughout this paper, atomic units are employed, i.e., $m_e = e = \hbar = 4\pi\epsilon_0 = 1$, unless specified otherwise.

3.2.1 xatom toolkit

In order to calculate electron-impact-ionization cross sections, we build our implementation on the preexisting XATOM toolkit [43, 79, 95]. This toolkit treats x-ray-atom interactions in an *ab initio* framework, employing nonrelativistic quantum electrodynamics and perturbation theory. XATOM is capable of calculating rates and cross sections of x-ray-induced processes, including photoionization, Auger decay, x-ray fluorescence, elastic x-ray scattering, and Compton scattering [96, 97]. It incorporates a Hartree-Fock-Slater (HFS) description of the many-electron system, which is an independent-particle approximation with a mean-field Hamiltonian:

$$\hat{H}_{\text{HFS}} = -\frac{1}{2}\nabla^2 - \frac{Z}{|\mathbf{x}|} + \int d^3x' \frac{n(\mathbf{x}')}{|\mathbf{x} - \mathbf{x}'|} + V_{\text{exc}}(\mathbf{x}), \quad (3.1)$$

where the exchange potential $V_{\text{exc}}(\mathbf{x})$ at zero temperature is of the form [98]

$$V_{\text{exc}}(\mathbf{x}) = -\frac{3}{2} \left[\frac{3}{\pi} n(\mathbf{x}) \right]^{1/3}, \quad (3.2)$$

and $n(\mathbf{x}) = \sum_i^{\text{occ}} \varphi_i^\dagger(\mathbf{x})\varphi_i(\mathbf{x})$ is the electron density, with $\varphi_i(\mathbf{x})$ denoting a single-particle spin-orbital wave function. Furthermore, the Latter tail correction is applied to this potential to ensure proper fall-off asymptotics [99]. Finally, the central-field approximation is made, imposing spherical symmetry. This enables us to write the solution of the Schrödinger equation in the form

$$\varphi_{nlms}(\mathbf{x}) = \frac{u_{nl}(r)}{r} Y_{lm}(\Omega_{\mathbf{x}}) \begin{pmatrix} \delta_{s,+1/2} \\ \delta_{s,-1/2} \end{pmatrix}, \quad (3.3)$$

with n , l , m , and s the principal, azimuthal, magnetic, and spin quantum number of the electron with the associated wave function $\varphi_{nlms}(\mathbf{x})$, respectively. Using this ansatz, XATOM subsequently solves the Schrödinger equation in a self-consistent way.

XATOM calculations involve numerous computational input parameters. In particular, the radial coordinate r in Eq. (3.3) is defined with the generalized pseudospectral method on a nonuniform grid [100], with the number of

radial grid points N , the maximum radius R_{max} , and the mapping parameter L , which determines the density distribution of radial grid points [100]. The larger L becomes, the more radial grid points are pushed towards higher values of r . There is also a cutoff parameter imposed on the azimuthal quantum number l , called l_{max} . We used $N = 200$, $L = 10$ a.u., $R_{max} = 80$ a.u., and $l_{max} = 35$ for all computations, unless specified otherwise.

3.2.2 Doubly differential electron-impact-ionization cross section

The expression for the doubly differential cross section (DDCS) for the inelastic scattering of an electron with a many-electron system is derived in Ref. [101]. The derivation is performed using the Born approximation, which assumes that both the incoming electron and the outgoing scattered electron have a high enough energy to be described by a plane wave. It takes on the form

$$\begin{aligned} \frac{d^2\sigma}{d\Omega_{\mathbf{q}_{out}}dE_{out}} &= \frac{4}{Q^4} \frac{q_{out}}{q_{in}} \sum_{I,F} P_I \left| \int d^3x \langle F | \hat{n}(\mathbf{x}) | I \rangle e^{i\mathbf{Q}\cdot\mathbf{x}} \right|^2 \delta(E_I - E_F + \omega) \\ &= \frac{4}{Q^4} \frac{q_{out}}{q_{in}} \sum_{I,F} P_I \left| \langle F | \hat{n}^\dagger(\mathbf{Q}) | I \rangle \right|^2 \delta(E_I - E_F + \omega), \end{aligned} \quad (3.4)$$

where $\hat{n}(\mathbf{x}) = \hat{\psi}^\dagger(\mathbf{x})\hat{\psi}(\mathbf{x})$ is the electron density operator, with $\hat{\psi}(\mathbf{x})$ being a fermionic field operator. The initial and final momenta of the incoming electron are denoted by \mathbf{q}_{in} and \mathbf{q}_{out} , \mathbf{Q} is their respective difference, $\mathbf{Q} = \mathbf{q}_{in} - \mathbf{q}_{out}$, $q_{in} = |\mathbf{q}_{in}|$, $q_{out} = |\mathbf{q}_{out}|$, and $Q = |\mathbf{Q}|$. The energies of the incoming and scattered electron are denoted as E_{in} and E_{out} , respectively. $|I\rangle$ and $|F\rangle$ represent the initial and final wave functions of the target system under consideration, and E_I and E_F denote their respective energies. Furthermore, P_I refers to the probability of finding the system in state $|I\rangle$ before the scattering. Finally, ω denotes the energy transfer $E_{in} - E_{out}$ from the incoming electron. The $1/Q^4$ dependence is a consequence of the Coulomb interaction between the projectile and the target, and exhibits an angular dependence, $Q^4 = [q_{in}^2 + q_{out}^2 - 2q_{in}q_{out}\cos(\theta)]^2$, where θ denotes the angle between the direction of the incoming and scattered electron. Azimuthal symmetry is always assumed.

In order to implement Eq. (3.4) into the HFS framework of `XATOM`, we introduce a complete orthonormal basis set of spin orbitals $|\varphi_p\rangle$ of the target, with orbital energy ε_p and associated fermionic creation and annihilation operators \hat{c}_p^\dagger and \hat{c}_p , respectively. The index p contains both spatial and spin quantum numbers. The field operator is expanded in this basis as $\hat{\psi}(\mathbf{x}) = \sum_p \varphi_p(\mathbf{x}) \hat{c}_p$. Within an independent-electron model, we approximate our initial state $|I\rangle$ as a single Fock state composed of the aforementioned spin

orbitals:

$$|I\rangle \approx |\{N_{el}\}\rangle \equiv \prod_{p=1}^{N_{el}} \hat{c}_p^\dagger |0\rangle, \quad (3.5)$$

where N_{el} denotes the number of electrons present in the initial state, and $|0\rangle$ is the vacuum state. Furthermore, we neglect all correlations between an electron eventually ejected during the collision and the electrons yet present in the parent ion. Within this approximation, we can write our final state as

$$|F\rangle \approx \hat{c}_f^\dagger \hat{c}_i |\{N_{el}\}\rangle. \quad (3.6)$$

After invoking these relations, we use the Condon rules [84], which allow for matrix elements with respect to Fock states to be reduced to matrix elements with respect to the spin orbitals. This enables us to transform Eq. (3.4) into the following form:

$$\begin{aligned} \frac{d^2\sigma}{d\Omega_{\mathbf{q}_{out}} dE_{out}} &= \frac{4}{Q^4} \frac{q_{out}}{q_{in}} \sum_{\{N_{el}\}} P_{\{N_{el}\}} \sum_{i,f} n_i^{\{N_{el}\}} (1 - n_f^{\{N_{el}\}}) \\ &\quad \times |\langle \varphi_f | e^{i\mathbf{Q}\cdot\mathbf{x}} | \varphi_i \rangle|^2 \delta(\varepsilon_i - \varepsilon_f + \omega) \\ &= \frac{4}{Q^4} \frac{q_{out}}{q_{in}} \sum_{i,f} \bar{n}_i (1 - \bar{n}_f) \\ &\quad \times \left| \int d^3x \varphi_f^\dagger(\mathbf{x}) e^{i\mathbf{Q}\cdot\mathbf{x}} \varphi_i(\mathbf{x}) \right|^2 \delta(\varepsilon_i - \varepsilon_f + \omega), \end{aligned} \quad (3.7)$$

where $n_i^{\{N_{el}\}}$ is the eigenvalue of the number operator $\hat{n}_i = \hat{c}_i^\dagger \hat{c}_i$, which is equal to 0 or 1 due to its fermionic nature. The superscript refers to the state on which the operator is acting on (in this case $|\{N_{el}\}\rangle$). The matrix element is calculated with respect to the spin orbitals $\varphi_{i,f}(\mathbf{x})$, with the orbital energies $\varepsilon_{i,f}$. Furthermore, we use the fact that $\sum_{\{N_{el}\}} P_{\{N_{el}\}} n_i^{\{N_{el}\}}$ represents the average number of particles in the orbital φ_i and is thus denoted by \bar{n}_i . At zero temperature ($T = 0$), we have $\bar{n}_i = N_{n_i, l_i} / \{2(2l_i + 1)\}$, with N_{n_i, l_i} denoting the number of electrons in subshell (n_i, l_i) . Likewise, $\bar{n}_f = N_{n_f, l_f} / \{2(2l_f + 1)\}$. For bound final states, N_{n_f, l_f} is the number of electrons in the final state characterized by the quantum numbers (n_f, l_f) .

In what follows we will apply Eq. (3.7) only to describe direct electron-impact ionization, i.e., a bound-to-free transition that ends up with the ejection of a bound electron into the continuum. We will not consider here the indirect excitation-autoionization channel—when an electron excitation is followed by a relaxation of the excited atom by ejecting an electron.

We proceed by implementing the ansatz from Eq. (3.3) for the spin orbitals $\varphi_{i,f}(\mathbf{x})$, which gives the following final expression for the DDCS,

$$\begin{aligned} \frac{d^2\sigma}{d\Omega_{\mathbf{q}_{\text{out}}}dE_{\text{out}}} &= \frac{4}{Q^4} \frac{q_{\text{out}}}{q_{\text{in}}} \sum_{n_f, l_f}^{\text{free}} \sum_{n_i, l_i}^{\text{occ.}} \delta(E_{\text{out}} - E_{\text{in}} - \varepsilon_{n_i, l_i} + \varepsilon_f) \\ &\times N_{n_i, l_i} \left[1 - \frac{N_{n_f, l_f}}{2(2l_f + 1)} \right] \sum_{L=0}^{l_i + l_f} (2L + 1) \\ &\times \left| R_{n_f, l_f, n_i, l_i}^L(Q) C_{l_i 0 L 0}^{l_f 0} \right|^2, \end{aligned} \quad (3.8)$$

where we explicitly denoted the orbital energy of the subshell (n_i, l_i) as ε_{n_i, l_i} , and where

$$R_{n_f, l_f, n_i, l_i}^L(Q) = \int_0^{R_{\text{max}}} dr u_{n_f l_f}(r) j_L(Qr) u_{n_i l_i}(r). \quad (3.9)$$

Here, $j_L(Qr)$ is a spherical Bessel function, and $C_{l_i 0 L 0}^{l_f 0}$ is a Clebsch-Gordan coefficient, which, due to the fact that $m_i = m_f = M = 0$, has the property that $l_i + l_f + L$ is an even integer in order to give a nonzero contribution. As we consider only ionization processes at zero temperature, we can set $N_{n_f, l_f} = 0$. Note that the sum $\sum_{n_f, l_f}^{\text{free}}$ only accounts for the situation when the ejected electron is free after the scattering process, i.e., when the system becomes ionized.

Let us consider the sum over the unoccupied final states. According to Eq. (3.8), these final states can be labeled with quantum numbers n_f and l_f . However, since we are considering bound-to-free transitions, the final states lie in the continuous part of the energy spectrum and cannot be labeled by the discrete number n_f . Instead, this label is replaced by the continuous parameter ε_f . The term $\sum_{n_f, l_f}^{\text{free}}$ should thus be read as $\sum_{l_f} \int d\varepsilon_f \rho_{l_f}(\varepsilon_f)$, where $\rho_{l_f}(\varepsilon_f)$ denotes the density of final states in between ε_f and $\varepsilon_f + d\varepsilon_f$, for a single discrete value of l_f . For energy-normalized wave functions $\rho_{l_f}(\varepsilon_f)$ reduces to unity, so we will omit it henceforth.

Conventionally, XATOM calculates the discrete bound states $u_{nl}(r)$ and the continuous free states $u_{\varepsilon l}(r)$ in two different ways. The bound states are calculated with the generalized pseudospectral method on a nonuniform radial grid [100], whereas the free states are determined by numerically solving the radial Schrödinger equation for a given ε using a fourth-order Runge-Kutta method on a uniform grid [102]. However, due to the implementation of both a uniform and a nonuniform grid, transitions from initial bound states to final free states require an interpolation between the two grids. This interpolation has to occur for every ε in the wide range of the energy spectrum and is, therefore, computationally expensive. As we are exclusively interested in bound-to-free transitions for impact ionization, we overcome

this difficulty by working only with the nonuniform grid and by approximating free states with a discrete nonuniform continuum: a *pseudocontinuum*. The latter step will be discussed in detail in the next section.

3.2.3 Implementation of pseudocontinuum for DDCS calculation

Recall that the DDCS in the HFS framework of XATOM takes on the following form in Eq. (3.8):

$$\begin{aligned} \frac{d^2\sigma}{d\Omega_{\mathbf{q}_{\text{out}}}dE_{\text{out}}} &= \frac{4}{Q^4} \frac{q_{\text{out}}}{q_{\text{in}}} \sum_{n_i, l_i}^{\text{occ.}} \sum_{l_f} \int d\varepsilon_f \delta(\varepsilon_f - \varepsilon_{n_i, l_i} + E_{\text{out}} - E_{\text{in}}) \\ &\quad \times N_{n_i, l_i} \sum_{L=0}^{l_i+l_f} (2L+1) \left| R_{\varepsilon_f, l_f, n_i, l_i}^L(Q) C_{l_i 0 L 0}^{l_f 0} \right|^2 \\ &\equiv \frac{4}{Q^4} \frac{q_{\text{out}}}{q_{\text{in}}} \sum_{n_i, l_i}^{\text{occ.}} \sum_{l_f} \int d\varepsilon_f f_{\varepsilon_f, l_f}^{(n_i, l_i)} \delta(\varepsilon_f - \Delta E^{(n_i, l_i)}), \end{aligned} \quad (3.10)$$

where we have defined $\Delta E^{(n_i, l_i)} = E_{\text{in}} - E_{\text{out}} + \varepsilon_{n_i, l_i}$, and

$$f_{\varepsilon_f, l_f}^{(n_i, l_i)} = N_{n_i, l_i} \sum_{L=0}^{l_i+l_f} (2L+1) \left| R_{\varepsilon_f, l_f, n_i, l_i}^L(Q) C_{l_i 0 L 0}^{l_f 0} \right|^2. \quad (3.11)$$

In order to calculate the DDCS, we need to evaluate ε_f and $f_{\varepsilon_f, l_f}^{(n_i, l_i)}$. As previously discussed, we calculate only discrete values of these quantities, which then define the pseudospectrum ε_{n_f} and $f_{n_f, l_f}^{(n_i, l_i)}$, with n_f denoting a discrete index, running from 1 to a certain finite integer number N . The question then arises as to how one can impose the proper energy normalization on the wave functions that comprise the obtained spectrum. To solve this issue, we assume that the calculated pseudospectrum is dense enough so that we can use local information on wave functions u_{n_f, l_f} and u_{n_f+1, l_f} , which have the corresponding energies ε_{n_f} and ε_{n_f+1} satisfying $\varepsilon_{n_f} \leq \varepsilon_f < \varepsilon_{n_f+1}$, similar to what was done in Refs. [103] and [104].

Our task is then to calculate an expression of the form $f_{l_f}^{(n_i, l_i)}(\Delta E^{(n_i, l_i)}) = \int d\varepsilon_f \delta(\varepsilon_f - \Delta E^{(n_i, l_i)}) f_{\varepsilon_f, l_f}^{(n_i, l_i)}$ by using a discrete pseudospectrum consisting of ε_{n_f} and $f_{n_f, l_f}^{(n_i, l_i)}$. Let us first integrate the function $f_{\varepsilon_f, l_f}^{(n_i, l_i)}$ up to a cutoff value $\Delta E^{(n_i, l_i)}$. The reason for this action will become apparent at the end of the explanation. Using our pseudospectrum, we can approximate this integral by the sum

$$\int^{\Delta E^{(n_i, l_i)}} d\varepsilon_f f_{\varepsilon_f, l_f}^{(n_i, l_i)} \approx \sum_{n_f=1}^m f_{n_f, l_f}^{(n_i, l_i)} \equiv \tilde{F}_{l_f}(\Delta E^{(n_i, l_i)}), \quad (3.12)$$

where $\varepsilon_m \leq \Delta E^{(n_i, l_i)} < \varepsilon_{m+1}$. $\tilde{F}_{l_f}(\Delta E^{(n_i, l_i)})$ is a histogram, where each value represents a partial, cumulative sum of $f_{n_f, l_f}^{(n_i, l_i)}$. The derivative of $\tilde{F}_{l_f}(\Delta E^{(n_i, l_i)})$ with respect to $\Delta E^{(n_i, l_i)}$, given by

$$\tilde{F}'_{l_f}(\Delta E^{(n_i, l_i)}) \equiv \sum_{n_f=1}^m f_{n_f, l_f}^{(n_i, l_i)} \delta(\varepsilon_{n_f} - \Delta E^{(n_i, l_i)}), \quad (3.13)$$

provides a discretized approximation of the quantity $f_{l_f}^{(n_i, l_i)}(\Delta E^{(n_i, l_i)}) = \int d\varepsilon_f \delta(\varepsilon_f - \Delta E^{(n_i, l_i)}) f_{\varepsilon_f, l_f}^{(n_i, l_i)}$. However, $\tilde{F}'_{l_f}(\Delta E^{(n_i, l_i)})$ suffers from the same δ -singularity problem. In order to overcome this issue, we connect the neighboring midpoints of the histogram values of $\tilde{F}_{l_f}(\Delta E^{(n_i, l_i)})$, constructing a piecewise linear function $F_{l_f}(\Delta E^{(n_i, l_i)})$. The derivative of *this* function, $F'_{l_f}(\Delta E^{(n_i, l_i)})$, will be a histogram and contains no δ functions. It can be shown [103, 104] that, with the increasing N , the function $F'_{l_f}(\Delta E^{(n_i, l_i)})$ converges to the correct value of $f_{l_f}^{(n_i, l_i)}(\Delta E^{(n_i, l_i)}) = \int d\varepsilon_f \delta(\varepsilon_f - \Delta E^{(n_i, l_i)}) f_{\varepsilon_f, l_f}^{(n_i, l_i)}$.

Using the method above, the DDCS is calculated by

$$\frac{d^2\sigma}{d\Omega_{\mathbf{q}_{\text{out}}} dE_{\text{out}}} = \frac{4}{Q^4} \frac{q_{\text{out}}}{q_{\text{in}}} \sum_{n_i, l_i}^{\text{occ.}} \sum_{l_f=0}^{l_{\text{max}}} \sum_{n_f=1}^m f_{n_f, l_f}^{(n_i, l_i)}, \quad (3.14)$$

where m is defined so as to uphold the relation $\varepsilon_m \leq \Delta E^{(n_i, l_i)} < \varepsilon_{m+1}$, and

$$f_{n_f, l_f}^{(n_i, l_i)} = N_{n_i, l_i} \sum_{L=0}^{l_i + l_f} (2L+1) \left| R_{n_f, l_f, n_i, l_i}^L(Q) C_{l_i 0 L 0}^{l_f 0} \right|^2. \quad (3.15)$$

With the calculated DDCS, we also have access to the singly differential cross sections, both angle- and energy-resolved, as well as to the total cross section (CS). In what follows we shall call the energy-resolved cross section DCS_E , whereas we define the DCS_θ to be the angle-resolved cross section, integrated over the azimuthal angle ϕ , i.e., $\text{DCS}_\theta = \int_0^{2\pi} d\phi (d\sigma/d\Omega_{\mathbf{q}_{\text{out}}})$. This integration can be immediately evaluated as the DDCS exhibits no dependence on ϕ . The upper limit of the energy integral, needed for the CS and DCS_θ , is chosen such that for each channel (n_i, l_i) , only ionization is considered. These calculations that involve an energy integral can also be evaluated immediately due to the presence of the δ function, negating the need for the machinery outlined above. Otherwise, when an explicit integral evaluation is needed, we employ nonuniform Gaussian quadrature.

3.2.4 BEB and Lotz models

Here we provide a short description of the BEB [92] and Lotz [91] models, as they will be compared to our results in Sec. 3.3. The binary-encounter-Bethe method [92] provides a simplified formula based on a binary collision

theory for direct electron-impact ionization. The BEB cross section (σ_{BEB}) is orbital specific. It depends on the orbital binding energy B , the orbital kinetic energy U , the electron occupation number N , and the dipole constant Q . The BEB cross section for each orbital is given by the following expression [105]:

$$\sigma_{\text{BEB}} = \frac{S}{t + (u + 1)/n} \left[\frac{Q \ln t}{2} \left(1 - \frac{1}{t^2} \right) + (2 - Q) \left(1 - \frac{1}{t} - \frac{\ln t}{t + 1} \right) \right], \quad (3.16)$$

where T is the energy of the incoming electron, $t = T/B$, $u = U/B$, $S = 4\pi a_0^2 N(R/B)^2$, $a_0 = 0.52918 \text{ \AA}$, $R = 13.6057 \text{ eV}$, and n is the principal quantum number of the orbital. In an ad hoc fashion, n is set to be 1 if $n < 3$. The dipole constant Q is defined in terms of the continuum dipole oscillator strength and the kinetic energy of the ejected electron. In most cases, Q is set to be equal to 1. The total cross section is a sum of these orbital contributions.

For some neutral atoms and ground-state ions, the orbital parameter B , required for evaluating Eq. (3.16), is available in the NIST database [105]. However, for most elements, the experimental data required for the input of the BEB formula are scarce, and in the case of exotic core-hole configurations of ions, they are mostly absent. In the former case, it is advised to use theoretically computed values instead [105], and we adopted this to the latter case as well. Therefore, we use B and U , which is a purely theoretical quantity, as obtained from the Hartree-Fock-Slater calculation performed with XATOM. Note that this implementation of the BEB formula using XATOM-evaluated atomic parameters has been used in XMDYN simulations [79,106]. Note further that the BEB formula makes no mention of the wave functions of the electrons within the target. Any contribution arising from a transition matrix element is therefore not accounted for. An incoming electron will distinguish two different systems with the same number of bound electrons only through a difference in the parameters B and U . How well this captures the difference in impact ionization for two ions with the same charge but of different electronic configuration is unknown.

The semiempirical formula provided by Lotz [91] for the total electron-impact-ionization cross section takes the following form:

$$\sigma_{\text{Lotz}} = \sum_{i=1}^N a_i q_i \frac{\ln(E/P_i)}{EP_i} (1 - b_i \exp[-c_i(E/P_i - 1)]), \quad \text{for } E \geq P_i, \quad (3.17)$$

where the sum over i runs over all N subshells, E is the energy of the incoming electron, P_i denotes the absolute value of the orbital energy of the i th

subshell, and q_i is the equivalent number of electrons present per subshell. The constants a_i , b_i , and c_i are orbital specific. Their values are listed in Ref. [91]. For the exotic electronic configurations, we used orbital energy values obtained from XATOM calculations. We also note that a formula similar to Eq. (3.17), taking into account inner-shell excitations and autoionization, has been obtained in Ref. [107]. The Lotz formula in Eq. (3.17) is the result of a best-fit approximation using all single-electron impact-ionization cross-section data available at the time it was proposed [88–91]. As these data were obtained from ground-state ions and atoms, one cannot expect Eq. (3.17) to yield well-established results for ions with exotic electronic configurations.

We would like to emphasize that the use of the BEB and Lotz formulas for ions with exotic electronic configurations is not standard practice, as neither of them was designed to handle these cases. However, it is still done, in part, because both the BEB and Lotz formulas are computationally efficient. In Sec. 3.3.2, we test these formulas with exotic electronic configurations by comparing their predictions with our *ab initio* calculations.

3.3 Results

Below we show electron-impact-ionization cross sections obtained for several electronic configurations of *carbon* and *sulfur* ions. These specific elements were selected due to their abundance in proteins and in biomolecules. In particular, we considered C^+ , and C^{2+} ions with different electronic configurations: (i) with the hole(s) in the innermost shell ($1s^1 2s^2 2p^2$ and $1s^0 2s^2 2p^2$) and (ii) with the hole(s) in the outermost valence shell ($1s^2 2s^2 2p^1$ and $1s^2 2s^2 2p^0$). For the sulfur ion, we removed eight electrons in order to show that the difference in cross sections obtained for two different electronic configurations of the same net charge is amplified for higher charge states. We considered either all holes in inner shells, or in valence shells ($1s^0 2s^0 2p^2 3s^2 3p^4$ and $1s^2 2s^2 2p^4 3s^0 3p^0$).

3.3.1 Doubly and singly differential electron-impact-ionization cross section

In Fig. 3.1 we show a contour plot of the DDCS ($\text{Mb eV}^{-1} \text{deg}^{-1}$ in a logarithmic scale) of a double core-hole ($1s^{-2}$) C^{2+} ion colliding with a 1-keV electron. The x and y axes show the scattering angle and the outgoing energy of the scattered electron, respectively. On the left panel, the DCS_E is plotted after the numerical integration over θ . To obtain converged results, this angular integration requires 50 angular grid points. The DCS_θ is plotted on the bottom panel. For the scattering-angle-resolved cross section, we only show the range from 0° to 60° , as the DDCS is almost negligible for $\theta \geq 60^\circ$. For the outgoing energy, we show the range from 800 to 1000 eV,

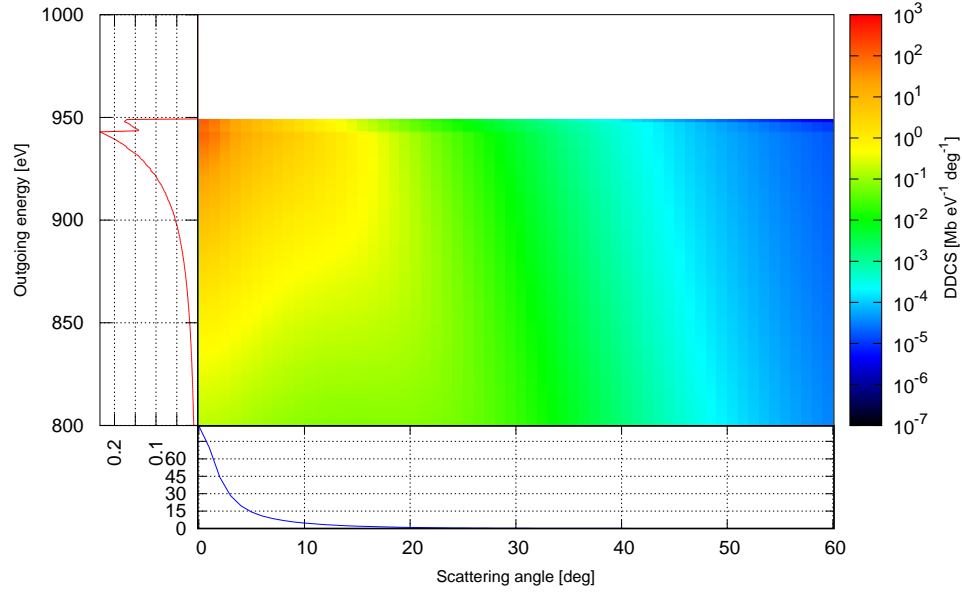


Figure 3.1: A contour plot depicting the doubly differential electron-impact-ionization cross section $[\text{Mb eV}^{-1} \text{ deg}^{-1}]$ of a double core-hole C^{2+} ion, on a \log_{10} scale. The incident energy of the electron is 1 keV. The x axis shows the scattering angle θ from 0° to 60° , and the y axis shows the energy of the scattered electron E_{out} from 800 to 1000 eV. The DCS_θ is plotted in blue and has units of Mb deg^{-1} . The DCS_E is plotted in red and has units of Mb eV^{-1} . The white area on the top indicates the region of zero cross section below the $2p$ edge (50.7 eV).

in which the cross section is the largest. In total, about 12 200 data points were calculated, which took ~ 31 min on one Intel Xeon E5-1620 CPU, corresponding on average to about 6.4 data points calculated per second. We note that DCS_θ calculations were much faster (~ 49 s for the whole range) because there was no need to numerically evaluate the energy integral. We used $N = 400$ for the number of radial grid points for all plots in Fig. 3.1. The DDCS plotted in Fig. 3.1 was multiplied by a factor of 2π , stemming from an integration over the azimuthal angle ϕ .

Figure 3.1 shows the presence of the ionization thresholds in the double core-hole C^{2+} ion, both in the DDCS and in the DCS_E (calculated to be at 50.7 and 56.5 eV for the $2p$ and $2s$ edge, respectively). The DDCS and DCS_θ reveal a high preference for low scattering angles, which is a consequence of the Coulomb factor $1/Q^4$ in Eq. (3.8).

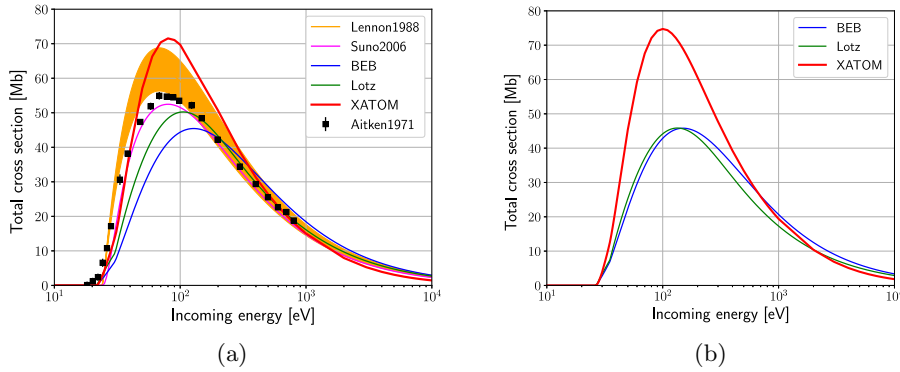


Figure 3.2: Total electron-impact-ionization cross section as a function of incoming electron energy in eV for C^+ with (a) one valence hole ($2p^{-1}$) and (b) one core hole ($1s^{-1}$). The XATOM label denotes the present *ab initio* calculations, in comparison with the BEB method [92] and the Lotz method [91]. For the ground-state C^+ ion, the predictions are also compared with experimental data (Aitken *et al.*, 1971 [110], Lennon *et al.*, 1988 [108], and Suno and Kato, 2006 [109]).

3.3.2 Total electron-impact-ionization cross section

In this section, we consider the total electron-impact-ionization cross sections for C^+ , C^{2+} , and S^{8+} , and compare our *ab initio* calculations for the ground-state ions to the experimental predictions [108–111], as well as to the Lotz [91] and BEB models [92]. The experimental data in Ref. [108] were provided with error bars, shown as a shaded orange area in the following figures. Additionally, for the carbon ions, a more recent review [109] was available, providing an additional set of recommended data. Figure 3.2 shows the electron-impact-ionization cross section for C^+ : (a) when the hole is in the valence shell and (b) when it is in the core shell. Figure 3.2(a) shows that our *ab initio* calculation (XATOM) is comparable to the results obtained from the Lotz and BEB models. In comparison with the experimental data, our result follows the quantitative trend of the data adequately. Both the initial rise at low incoming energies and the later decrease at higher incoming energies are captured quite well by the XATOM result. Only in the intermediate region, where the peak is located, our result overestimates the cross section with respect to the experimental values before falling back into the proper range of values. Of course, improved results are expected for higher incoming electron energies due to the plane-wave formalism employed in the description of the incoming electron. Comparing with Fig. 3.2(b), we can observe that both Lotz and BEB results differ slightly for both the core-hole and the valence-hole cases, similarly as the XATOM results. The CPU run-

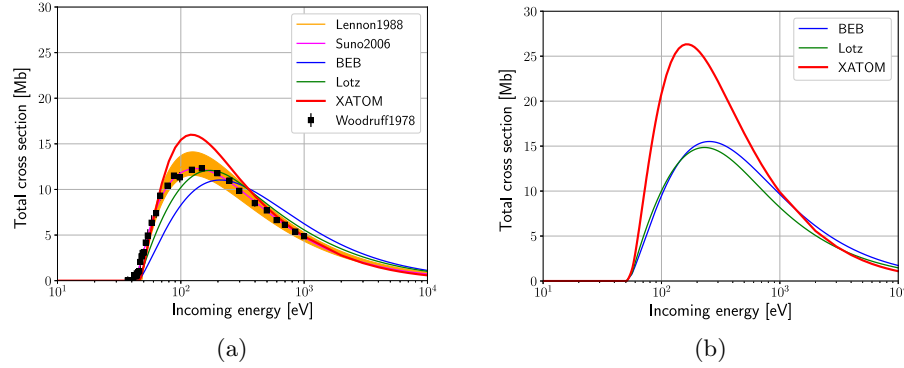


Figure 3.3: Total electron-impact-ionization cross section as a function of incoming electron energy in eV for C²⁺ with (a) two valence holes (2p⁻²) and (b) two core holes (1s⁻²). For the ground-state configuration (a), three experimental data sets (Woodruff *et al.*, 1978 [111], Lennon *et al.*, 1988 [108], and Suno and Kato., 2006 [109]) are compared with theory predictions.

time for a single total cross-section calculation with XATOM is dependent on the incoming electron energy; it was 10.5 s on average.

Figure 3.3 shows the total electron-impact-ionization cross section for C²⁺ with (a) two valence holes and (b) two core holes. Figures 3.3(a) and 3.3(b) demonstrate that for higher ion charges the difference in cross sections calculated for the distinct electronic configurations becomes more pronounced. In particular, Fig. 3.3(a) shows a similar trend as in Fig. 3.2(a), where the XATOM result was comparable to both Lotz and BEB models. Also, the XATOM result shows a similar kind of relation with the experimental data: the initial rise and later decrease of the data are reproduced quite accurately by XATOM, whereas it overestimates the values around the peak. Similarly, Fig. 3.3(b) again shows that both Lotz and BEB results differ slightly for the core-hole and the valence-hole cases. However, the XATOM result predicts a relatively large difference in cross sections for these cases.

Figure 3.4 shows the S⁸⁺ case: (a) with eight outer holes (2p⁻²3s⁻²3p⁻⁴) and (b) with eight inner holes (1s⁻²2s⁻²2p⁻⁴). For the ground-state configuration in Fig. 3.4(a), a trend similar to the carbon cases can be identified. By comparing Figs. 3.4(a) and 3.4(b), a large difference between total cross section for distinct electronic configurations becomes visible. We note that the positions of the maximum of the total cross section predicted with XATOM resemble the experimental ones more closely than those predicted with the Lotz and BEB models for all three cases considered. We have restricted the incoming electron energy to a maximum of 10 keV. At higher electron energies, relativistic effects [93, 94] become increasingly important. These are currently not incorporated in our approach.

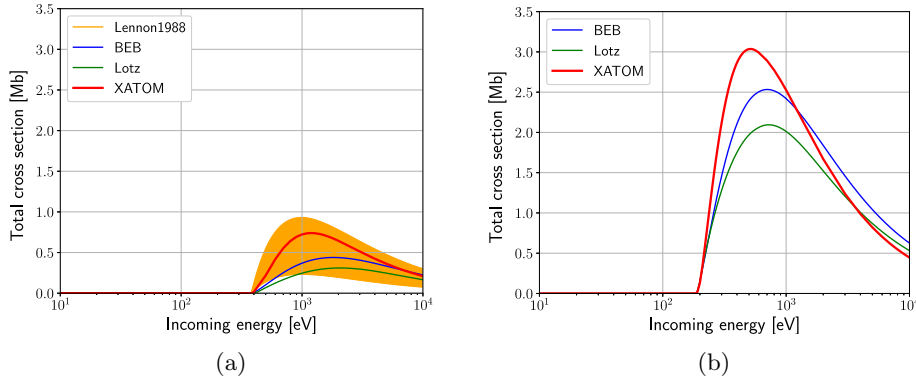


Figure 3.4: Total electron-impact-ionization cross section as a function of incoming electron energy in eV for S^{8+} with (a) eight outer holes ($2p^{-2} 3s^{-2} 3p^{-4}$) and (b) eight inner holes ($1s^{-2} 2s^{-2} 2p^{-4}$). For the ground-state configuration (a), the experimental data set from [108] is shown.

We conclude this section with an error estimate of our approach. As mentioned in Sec. 3.2.2, the incoming electron is described in a plane-wave formalism, which is an increasingly accurate description for higher incoming electron energies. Therefore, we will perform our error estimate as follows: We choose two values of the incoming energy, one for the representation of low incoming energies and the other for high energies. We chose 100 eV and 1 keV, respectively, for C^+ and C^{2+} , whereas for S^{8+} we chose 1 and 10 keV for the low and high incoming energy regime, respectively. At these points, we compare the values of the impact-ionization cross section for the ground-state ions between XATOM and the experimental dataset of Lennon [108] in order to obtain an upper limit for the percentage error estimate for the XATOM result. We chose this dataset to have a consistent comparison for all systems. At 100 eV, the error estimates for C^+ and C^{2+} are 18% and 24%, respectively, whereas at 1 keV they are 6.2% and 1.2%, respectively. The error estimates for S^{8+} are 25% at 1 keV and 14% at 10 keV. We argue that, since XATOM treats ground-state ions and exotic ions within a consistent *ab initio* framework, we expect at most the same percentage errors for the core-hole ions as for the ground-state ones.

3.3.3 Discussion

Below we discuss the observed trends in impact-ionization cross sections when comparing ground-state ions to their core-hole variants. Figures 3.2, 3.3, and 3.4 show that the impact-ionization cross section calculated by XATOM is larger for the core-hole configurations than for the ground-state ions. The magnitude of the difference depends on both the ion charge and

the energy of the incoming electron. The Lotz result does not follow this trend generally. As observed in Figs. 3.2(a) and 3.2(b), the Lotz result shows that the core-hole ion has a smaller cross section than the ground-state ion. We attribute this to the inapplicability of the Lotz formula for ions with exotic electronic configurations, as already discussed in Sec. 3.2.4. On the other hand, the BEB result does follow the trend of the XATOM result in all cases considered, albeit to a smaller extent. We argue that the physical reason behind this trend is a combination of two mutually competing factors in the core-hole ions. On the one hand, there are more valence electrons to interact with, which increases the cross sections. On the other hand, this effect is partly compensated by the change in orbital size due to the increased positive charge seen by valence electrons and results in a slight decrease of the cross sections. We will first make our arguments for the XATOM calculations, after which we will show why the BEB result follows the same trend.

The contribution to the total impact-ionization cross section from core-shell electrons calculated by XATOM was observed to be very small as compared to the contribution from valence-shell electrons, which is consistent with previous works [92]. For the purposes of this discussion, the contribution of core shells can be neglected. Now consider the example of C^{2+} . The ground-state ion has two electrons left in the $2s$ valence shell. In contrast, its double core-hole variant has four valence electrons which will contribute to the impact-ionization cross section, and so we would expect to see the cross section for the double core-hole case to be approximately double the one for the ground-state ion. This is indeed the case for incoming energies above 1 keV, as shown in Fig. 3.3. A similar conclusion can be drawn for C^+ , only now the cross section for the single valence-hole and single core-hole ions should not differ by a factor of 2 but by a factor of $4/3$, since we move from a case with three valence electrons to one with four. This is again observed in Fig. 3.2 for the energies beyond 1 keV. As for S^{8+} , the eight-core-hole ion has six more valence electrons than its eight-valence-hole variant. The cross sections for the two S^{8+} variants never differ by as much as a factor of 6 for the incoming energies considered, as is seen in Fig. 3.4. Instead, a factor of 3.5 can be deduced at most.

This leaves us to find some features of the core-hole variants of S^{8+} , C^{2+} , and C^+ , which compensate the effect of the increase in cross section due to the presence of more valence electrons, and which manifest themselves more for lower energies in the case of the carbon ions. To this end, note that the argument based on counting valence electrons assumes that the contributions to the cross section of the valence shells in the core-hole variants are roughly the same. However, for both C^+ and C^{2+} , we observed that the contribution from the $2s$ shell is smaller for the core-hole ion variant as compared to the ground-state ion, the difference of which diminishes for higher incoming energies. Since the configurations of S^{8+} we considered have

no orbitals which contain the same amount of electrons, such a comparison is less meaningful for S^{8+} . We attribute this to the decreased size of the valence orbitals in the core-hole variants caused by the increased positive charge they experience from the nucleus, as there is no screening effect from core electrons. To understand why a smaller orbital leads to a diminished contribution in the cross section, let us consider the transition matrix element in the expression for the impact-ionization cross section in Eq. (3.7). Also, we will separately consider low incoming energies (of the order of 100 eV) and high ones (1 keV or higher) in what follows.

Let us start with the regime of low incoming electron energies (take $E_{in} = 100$ eV) and consider the matrix element $\langle \varphi_f | e^{i\mathbf{Q}\cdot\mathbf{x}} | \varphi_i \rangle$. For an electron of 100 eV, the de Broglie wavelength is of the order of 1 Å. Since the ejected electron energy is less than the incoming electron energy, the de Broglie wavelength of the ejected electron will be larger than 1 Å. However, this is much larger than the spatial extent of the initial orbitals we are considering. Therefore, when performing the integration of $\langle \varphi_f | e^{i\mathbf{Q}\cdot\mathbf{x}} | \varphi_i \rangle$, we can largely consider $\langle \varphi_f |$ to be a constant. What remains is an integration over $e^{i\mathbf{Q}\cdot\mathbf{x}} \varphi_i(\mathbf{x})$, which is simply the Fourier component of the initial orbital associated with \mathbf{Q} , denoting the momentum transfer from the incoming electron. Effectively, we are considering the momentum distribution of the initial orbital $|\varphi_i\rangle$, evaluated at the momentum transfer \mathbf{Q} . However, not all values of \mathbf{Q} are considered. Since $\mathbf{Q} = \mathbf{q}_{in} - \mathbf{q}_{out}$, and, for our incoming electron, \mathbf{q}_{in} is of the order of $\sqrt{2E_{in}}$, \mathbf{Q} will not sample many points in the momentum distribution of $|\varphi_i\rangle$ for low energies. Combining this with the fact that smaller initial orbitals will have a more spread out momentum distribution leads to a smaller transition matrix element, thus diminishing the contribution to the impact-ionization cross section.

At higher energies (for example, $E_{in} = 1$ keV), the energy transfer from the incoming electron may be substantial, so we cannot assume the de Broglie wavelength of the ejected electron to be constant when performing integration of the matrix element $\langle \varphi_f | e^{i\mathbf{Q}\cdot\mathbf{x}} | \varphi_i \rangle$. However, in such cases, \mathbf{Q} will include a much larger range of values to sample over. Additionally, we can argue that the highly energetic ejected electron could equally well be described as a plane wave with an associated momentum \mathbf{q}_{ejec} . Then the transition matrix element will be an integral over $e^{i(\mathbf{Q}-\mathbf{q}_{ejec})\cdot\mathbf{x}} \varphi_i(\mathbf{x})$. From here on, we can reuse the Fourier analysis argument from the low-energy case. Again, a smaller initial orbital will lead to a spread in its momentum distribution, but since \mathbf{Q} will include a much larger range of values for sampling, we can argue that the diminishing effect to the cross-section contribution will be less present for higher energies. This last effect is not seen in the S^{8+} case, because the much stronger Coulomb interaction experienced by the incoming electron, as compared to the C^+ and C^{2+} cases, pushes the validity of the plane-wave framework to higher energies than those that were considered.

	Orbital kinetic energies U [eV]				
	$1s$	$2s$	$2p$	$3s$	$3p$
$C^+ (1s^{-1})$	478.9	67.6	63.8	-	-
$C^+ (2p^{-1})$	447.0	54.1	45.5	-	-
$C^{2+} (1s^{-2})$	495.8	89.6	91.0	-	-
$C^{2+} (2p^{-2})$	448.6	60.9	54.1	-	-
$S^{8+} (1s^{-2} 2s^{-2} 2p^{-4})$	3469.5	801.1	810.5	271.5	268.6
$S^{8+} (2p^{-2} 3s^{-2} 3p^{-4})$	3332.4	582.7	567.1	179.9	169.3

Table 3.1: The orbital kinetic energies in [eV] as calculated by XATOM for all systems considered and used for the calculation of the BEB cross sections.

These two factors which we have discussed above are also captured, to a different extent, by the BEB formula. First, the overall factor of N , denoting the number of electrons present in the orbital considered, is contained in Eq. (3.16). Second, the diminishing factor from the decreased orbital size is captured by the orbital kinetic energy U in the denominator of Eq. (3.16). We can relate the size of an orbital to the orbital kinetic energy as follows. The orbital kinetic energy is related to the momentum distribution of the target electron through $U = \langle \hat{\mathbf{p}}^2 \rangle / 2$, with $\hat{\mathbf{p}}$ the momentum operator of an electron in a certain subshell. This means U is associated to the second moment of the momentum distribution, i.e., its width. As an orbital becomes smaller and thus more localized, its momentum distribution will spread, causing U to become larger and therefore decreasing the BEB cross section. In order to justify the observed trend in Figs. 3.2 and 3.3, this would imply that the orbital kinetic energies U of the core-hole variants should be larger than those of the ground-state ions. Table 3.1 shows the values of U for each shell of each system considered, as calculated by XATOM. It shows, without exception, that the orbital kinetic energies U of the core-hole variants are indeed larger than those of the ground-state ions. Therefore, the qualitative behavior of the BEB result follows that of our *ab initio* calculations.

3.4 Conclusion and outlook

To sum up, we have developed a versatile *ab initio* scheme for calculation of direct electron-impact-ionization of ions in any electronic configuration at zero temperature within the Hartree-Fock-Slater (HFS) framework. In particular, we have incorporated the known formula for the doubly differential electron-impact-ionization cross section (DDCS) derived in Ref. [101] into the HFS-based XATOM toolkit. Within the scheme, the incoming electron and the scattered electron are treated using plane waves, the atomic system under consideration with a HFS approach, and the final state of the ejected electron with a pseudocontinuum description. From the DDCS obtained,

we have calculated singly differential cross sections, both angle and energy resolved, as well as the total electron-impact-ionization cross section.

Our approach, derived in the first Born approximation, should work accurately not only for the description of electron-impact ionization of cold ions, but also for more complex systems like molecules, solids, and plasmas, provided that the assumption of a weak scattering potential seen by the impact electron is reliable, i.e., the average interaction energy between the impact electron and the scatterer(s) is much lower than the kinetic energy of the impact electron. Following this criterion, we expect that especially in the condensed-matter systems, where the screening of ions diminishes the effect of long-range Coulomb interaction between the incoming electron and constituent ions, also the regime of lower electron-impact energies will be accessible for the impact-ionization cross sections calculated with this method.

The *ab initio* calculations can be easily incorporated in x-ray-induced dynamics simulations treating the relaxation of atoms after high-energy-impact collision and provide impact-ionization cross sections for any exotic (multihole) configuration.

On the examples of ground-state carbon and sulfur ions, we have shown that the results of our *ab initio* scheme for total electron-impact-ionization cross section manage to reproduce the experimental data at high energies of the incoming electron to a satisfactory degree, while resembling the overall trend of the data sets for all incoming energies considered. For the exotic configurations, for which no experimental data are available, our *ab initio* method enables us to perform cross-section calculations without any difficulties. Our results indicate that there are significant differences in impact-ionization cross sections between the core-hole (exotic) and valence-hole (ground-state) configurations in ions of the same charge, which increase with an increasing charge of the ions. Also, our results are, in general, comparable to those obtained with the BEB and Lotz models for core-hole configurations, using the input parameters calculated with XATOM. However, our method indicates stronger differences between the impact-ionization cross sections for core- and valence-hole configurations than the BEB and Lotz models. The discrepancies observed increase with increasing charge of the ions.

We expect that this finding can have a significant impact on any quantitative modeling studies treating the relaxation of atoms after high-energy-impact collision, e.g., simulations for coherent x-ray diffraction imaging of nanocrystals and single biological macromolecules, or studies of laser-created plasmas. While we advocate the use of an *ab initio* method, the need for repeated cross-section calculations in simulations of x-ray-driven complex systems requires striking a balance between numerical accuracy and computational efficiency. We believe that our implementation within XATOM satisfies these requirements. For quantitative checks, further studies are re-

quired in specific contexts. In particular, for dense samples, the inclusion of finite temperature and treatment of the ion's environment are necessary. This development is already underway.

Chapter 4

Electronic-structure calculations for nonisothermal warm dense matter

This Chapter reflects the work done in the article [3], of which I am the first author, and has been included verbatim:

BEKX, SON, ZIAJA, SANTRA, Phys. Rev. Res. **2**, 033061 (2020).

Copyright (2020) by the American Physical Society. Reproduced with permission of the American Physical Society for the purpose of this thesis.

Abstract

Warm dense matter (WDM) is an exotic state of matter that is inherently difficult to model theoretically, due to the fact that the thermal Coulomb coupling and quantum effects are comparable in magnitude and must be treated on equal footing, foregoing the employment of conventional methods from either plasma physics or condensed-matter physics. Our work focuses on describing electronic states present in a transient, nonisothermal WDM state, where electrons become hot and ions remain cold, during the first 10–100 fs after the irradiation of a solid sample with an intense femtosecond x-ray pulse. We present a methodology, combining the finite-temperature Hartree-Fock-Slater approach with the Bloch-wave approach within a periodic atomic lattice, implemented in a new toolkit, XCRYSTAL. In XCRYSTAL, electronic states are represented in a hybrid basis comprising plane waves and localized core orbitals on a radial pseudospectral grid. This hybrid basis ensures a high numerical efficiency as highly localized states need not be described using plane waves. Additionally, these core orbitals are respon-

sive to the presence of delocalized plasma electrons through an interwoven optimization between inner-shell and outer-shell electronic states employed in XCRYSTAL. Therefore, not only does XCRYSTAL model the plasma electrons efficiently, it also allows for access to inner-shell modifications at high electronic temperatures. To benchmark our method, we calculate K -shell threshold energies of x-ray-excited solid-density aluminum as well as the ionization potential depression and show their agreement with experiment. In comparing our method with other theoretical models, we conclude that the incorporation of optimized inner-shell orbitals is essential to obtain accurate results, and we find that the inclusion of the full crystal structure has a limited effect. Furthermore, we obtain temperature-dependent band structure predictions at WDM conditions, up to temperatures of 100 eV, which, to the best of our knowledge, are the first of their kind for this non-isothermal system. We expect that our proposed methodology will aid in the theoretical description of nonisothermal WDM, as well as advance the understanding of this exotic state of matter.

4.1 Introduction

Warm dense matter (WDM) has gained significant interest because of its abundant presence in a variety of physical systems. It is relevant to astrophysics, specifically for the research of the interiors of stellar bodies [51, 52] and large planets [53–55], in the field of inertial confinement fusion [56–59], and in laboratory experiments involving high-power laser sources, such as those at the National Ignition Facility [112], LCLS [10], SACLA [11], PAL-XFEL [14], FLASH [16], and the European XFEL [12].

WDM lies on the border between condensed-matter physics and plasma physics [50]. It is characterized by temperatures of the order of $T \sim 0.1 - 100$ eV and densities ranging from 10^{-3} to 10^2 g/cm³. The WDM regime is inherently challenging to describe theoretically because both thermal Coulomb coupling and quantum-mechanical effects are then of a similar magnitude. This implies that typical methods of conventional condensed-matter physics and plasma physics are not trivially extended into the WDM regime, nor can one justify the imposition that one effect is described as a small perturbation of the other. However, WDM is now routinely being produced during high-power-laser experiments, driving the need for a thorough understanding of this regime. Additionally, with the advent of x-ray free-electron lasers (XFELs) over the last decade, a rejuvenated interest in WDM has been garnered due to the ability of XFELs to produce this state of matter transiently and to probe it [34, 60–62, 113, 114].

Over the years, various theoretical models and approaches have been developed to describe WDM and its properties. Among them are the Ecker-Kröll (EK) model [115], the Stewart-Pyatt (SP) model [116], the average-

atom (AA) model [117–120] and its variation [121], finite-temperature density functional theory (DFT) [122–124], frequently in combination with *ab-initio* molecular dynamics (QMD) [125–133], time-dependent DFT [134], Monte Carlo molecular dynamics [82], quantum kinetic theory [135, 136], and quantum Monte Carlo simulations [137, 138]. A recent review highlighting and analyzing the last two topics can be found in Ref. [139].

In the current study, we will focus on the description of WDM created by an intense femtosecond XFEL pulse from solid aluminum (Al). Specifically, we will limit ourselves to the description of the electronic states during the first 10–100 fs after the x-ray exposure, which allows us to assume that the ion lattice remains cold. This assumption is well justified as the heating of electrons by the laser pulse occurs much faster than the transfer of energy to ions through electron-ion coupling [64–70]. Additionally, the dense electronic environment created forces the electrons to rapidly thermalize (on the order of a few fs to a few tens of fs) through electron-electron collisions and impact-ionization processes [140]. These assumptions allow us to describe the system as a hot, thermalized electron distribution embedded in a periodic crystal lattice, constituted of parent ions. The system is modeled by a muffin-tin potential, whereas the description of electronic states is done using a finite-temperature Hartree-Fock-Slater approach. These states are represented with respect to a hybrid basis consisting of plane waves and localized core orbitals solved on a radial pseudospectral grid. A simultaneous interleaved optimization of inner-shell and outer-shell electronic states accounts for inner-shell modifications at high electronic temperatures in an efficient manner. Additionally, the periodicity of the system allows for the implementation of the Bloch formalism [141], increasing computational efficiency. A detailed description of the developed methodology is presented in Sec. 4.2. The model has been implemented into a new toolkit, XCRYSTAL.

With the calculated electronic states, various characteristic properties of the transient, nonisothermal WDM state become available for evaluation and for comparison with experimental data. In order to benchmark XCRYSTAL, we will compare our model results to the data from the experiment performed at the LCLS on x-ray excited solid Al [34, 61, 62]. Specifically, the *K*-shell threshold energies were measured for this system. From them, the ionization potential depression (IPD) was determined, i.e., the lowering of the ionization potentials of atoms present in the system caused by the dense and charged environment. It was used to check the predictive capabilities of the widely-used EK and SP models [34, 61, 131]. The predictions of the SP model were found to be unsatisfactory, and a modified EK model [61, 142] was proposed for fitting the data.

In what follows, we will provide XCRYSTAL predictions for the *K*-shell threshold energy and IPD for Al, and compare them to experiment and the aforementioned theoretical models. In addition, we will compare the results from XCRYSTAL with those obtained from the AA model and the two-step

HFS model, introduced in Ref. [121]. Because of the incorporation of the periodic crystal structure within our model, it is possible with XCRYSTAL to calculate the band structure of the system at very high electronic temperatures (~ 100 eV). Let us also note that, even though band structure calculations at finite temperatures have been performed before [143, 144], it has never been done in the regime of such high temperatures for the type of transient WDM state we are considering. Also, the WDM system that we are interested in is strongly nonisothermal. It is characterized by electronic temperatures far above room temperature (up to 10–100 eV or 10^5 – 10^6 K) and ion temperatures close to room temperature. Therefore, the finite-temperature band structure calculations that we obtain at these conditions will be the first of their kind.

The paper is structured as follows: In Sec. 4.2 we outline the theory framework. In the following Sec. 4.3, we provide the K -shell threshold energies and the IPD values for solid-density aluminum (Al) at electron temperatures ranging from 0 to 100 eV. We then compare them with experiment and various theoretical models. Finally, we present the temperature-dependent band structure calculations of this system at various temperatures, and comment on the trends observed. In Sec. 3.4 we provide conclusions and an outlook.

4.2 Methodology

In this section we outline our theory framework. In particular, we describe the treatment of electrons in our approach. We distinguish between (1) electrons highly localized around an ion (core electrons) and (2) electrons delocalized within the unit cell (valence electrons). Worthy of note is that in our framework we will update the core electrons to the presence of the plasma electrons as opposed to keeping them frozen as is custom in low-temperature condensed-matter calculations. Our approach consists of describing the electronic states as Bloch states, represented in a hybrid basis consisting of plane waves and these updated localized core orbitals. Throughout this paper, atomic units are employed, i.e., $m_e = e = \hbar = 4\pi\epsilon_0 = 1$. We also set $k_B = 1$. The unit of length will be given in units of the Bohr radius, a_0 , and energies and temperatures will be given in electronvolts (eV).

4.2.1 Schrödinger equation for a periodic system

We consider a perfectly periodic crystal. The crystal lattice is defined by the primitive lattice vectors \mathbf{a}_1 , \mathbf{a}_2 , and \mathbf{a}_3 , thus defining a primitive unit cell volume $\Omega = |\mathbf{a}_1 \cdot (\mathbf{a}_2 \times \mathbf{a}_3)|$. In the independent-particle approximation, the wave function of an electron in a periodic system can be represented as

a Bloch wave:

$$\varphi_{n,\mathbf{k}}(\mathbf{r}) = \frac{1}{\sqrt{V}} e^{i\mathbf{k}\cdot\mathbf{r}} \mu_{n,\mathbf{k}}(\mathbf{r}), \quad (4.1)$$

where a total volume $V = N_{\text{cell}}\Omega$ is introduced to ensure periodic boundary conditions, with N_{cell} the number of primitive cells. Furthermore, \mathbf{k} is the wave vector of the electron, n is a band index, and $\mu_{n,\mathbf{k}}(\mathbf{r})$ is a lattice periodic function, i.e., $\mu_{n,\mathbf{k}}(\mathbf{r} + \mathbf{a}_i) = \mu_{n,\mathbf{k}}(\mathbf{r})$, with $i = 1, 2$, and 3 . Both labels \mathbf{k} and n specify an eigenstate of the effective one-electron (mean-field) Hamiltonian, $\hat{H} = [-\frac{1}{2}\nabla^2 + V(\mathbf{r})]$, where $V(\mathbf{r})$ is the mean-field potential of the periodic system. Since $\mu_{n,\mathbf{k}}(\mathbf{r})$ is periodic, we can decompose it into a Fourier series. In a Bravais lattice, this corresponds to a Fourier series with respect to a sum over reciprocal lattice vectors $\mathbf{K} = \sum_{i=1}^3 \beta_i \mathbf{b}_i$, with β_i being integer coefficients and \mathbf{b}_i being the reciprocal lattice basis vectors, which obey $\mathbf{b}_i \cdot \mathbf{a}_j = 2\pi\delta_{ij}$. The Fourier decomposition is thus

$$\begin{aligned} \mu_{n,\mathbf{k}}(\mathbf{r}) &= \sum_m v_{n,\mathbf{k}}(\mathbf{K}_m) e^{i\mathbf{K}_m \cdot \mathbf{r}}, \quad \text{with} \\ v_{n,\mathbf{k}}(\mathbf{K}_m) &= \frac{1}{\Omega} \int_{\Omega} d^3r e^{-i\mathbf{K}_m \cdot \mathbf{r}} \mu_{n,\mathbf{k}}(\mathbf{r}), \end{aligned} \quad (4.2)$$

where $m = (\beta_1, \beta_2, \beta_3)$ runs over all reciprocal lattice vectors \mathbf{K}_m and the latter integral is restricted to a unit cell. This implies that the wave function is expanded in a plane-wave basis of the form

$$\varphi_{n,\mathbf{k}}(\mathbf{r}) = \frac{1}{\sqrt{V}} \sum_m v_{n,\mathbf{k}}(\mathbf{K}_m) e^{i(\mathbf{k} + \mathbf{K}_m) \cdot \mathbf{r}}. \quad (4.3)$$

After inserting Eq. (4.3) into the Schrödinger equation, $\hat{H}\varphi_{n,\mathbf{k}}(\mathbf{r}) = E_{n,\mathbf{k}}\varphi_{n,\mathbf{k}}(\mathbf{r})$, we arrive at its representation in \mathbf{k} space for a periodic system:

$$\left[\frac{1}{2}(\mathbf{k} + \mathbf{K}_i)^2 - E_{n,\mathbf{k}} \right] v_{n,\mathbf{k}}(\mathbf{K}_i) + \sum_j W(\mathbf{K}_i - \mathbf{K}_j) v_{n,\mathbf{k}}(\mathbf{K}_j) = 0, \quad (4.4)$$

where i and j denote specific reciprocal lattice vectors and $W(\mathbf{K}) = \frac{1}{\Omega} \int_{\Omega} d^3r e^{-i\mathbf{K} \cdot \mathbf{r}} V(\mathbf{r})$. So far, this representation is general as all that was assumed to derive it was a perfect crystal structure. This allowed us to use a lattice periodic potential $V(\mathbf{r})$, decomposable in a Fourier series over the reciprocal space, and to describe the electrons with a one-electron wave function specified by Eq. (4.1). This implies that we neglect correlation effects.

4.2.2 Hybrid basis

A direct attempt to solve Eq. (4.4) would be computationally extremely costly as an accurate representation of the highly localized core states in a

basis of plane waves would require the contribution of large wave vectors. This would result in a very slow convergence of the solution. Many different methods of overcoming this problem, typically involving the separation of the localized core electrons from the delocalized valence electrons, have been developed over the years. They include the utilization of Wannier functions [145–147], pseudopotential methods [148, 149], and the augmented plane wave (APW) method [150–152].

Similar to the APW method, we intend to extend the basis of the plane waves so as to include atomic orbitals. Naturally, we do not wish to include *all* atomic orbitals in our hybrid basis. Only those that are highly localized, i.e., for which the description using only plane waves is inefficient, are added to this hybrid basis. We will refer to them as *core orbitals*. This provides an ansatz for our wave functions in the form

$$\varphi_{n,\mathbf{k}}(\mathbf{r}) = \frac{1}{\sqrt{V}} \sum_m v_{n,\mathbf{k}}(\mathbf{K}_m) e^{i(\mathbf{k}+\mathbf{K}_m)\cdot\mathbf{r}} + \sum_{n_C} w_{n,\mathbf{k}}(n_C) \psi_{n_C,\mathbf{k}}(\mathbf{r}), \quad (4.5)$$

where m runs from 1 to some cutoff index $N_{\mathbf{K}}$, which represents the number of valence bands. The index n_C denotes the band index of the core wave functions, introduced as follows. Since $\varphi_{n,\mathbf{k}}(\mathbf{r})$ is a Bloch function and the first term of Eq. (4.5) is structured so as to be a Bloch function [like in Eq. (4.3)], the core wave functions $\psi_{n_C,\mathbf{k}}(\mathbf{r})$ must be Bloch functions. We can construct them using the conventional atomic orbitals that are eigen-solutions of the Hamiltonian, with one Bloch function per core orbital, per atom in the unit cell. This implies that the general label n_C includes information regarding which atom in a unit cell we are considering, as well as the electronic structure information, i.e., $n_C = (a, n, l, m, s)$, where a denotes an atomic index, and n, l, m , and s denote the principal, azimuthal, magnetic, and spin quantum number, respectively. Subsequently, n_C runs from 1 to the total number of core orbitals, N_C , in the unit cell. Suppose that $\phi_{n_C}(\mathbf{r})$ denotes an atomic orbital that is strongly localized (for a detailed explanation of “strong localization” see Sec. 4.2.3) and can be considered as a core orbital. Let \mathbf{R}_{I,n_C} denote the position of the nucleus in the I th unit cell at which the spatial orbital of the n_C type is located: $\mathbf{R}_{I,n_C} = \mathbf{R}_I + \mathbf{r}_{n_C}$, with \mathbf{R}_I being the lattice vector denoting the I th unit cell, and $\mathbf{r}_{n_C} = \mathbf{R}_{0,n_C}$. The associated atomic core orbital can then be written as $\phi_{n_C}(\mathbf{r} - \mathbf{R}_{I,n_C})$. Since the unit cells are identical, the $\phi_{n_C}(\mathbf{r} - \mathbf{R}_{I,n_C})$ for all the unit cells I are degenerate eigenfunctions of the mean-field Hamiltonian, as they all have the exact same eigenvalue E_{n_C} as a consequence of the assumed strong localization. Therefore, *any* linear combination of them is also an eigenfunction of the same Hamiltonian. In particular, we can choose a linear combination such that the resulting wave function is a Bloch wave $\psi_{n_C,\mathbf{k}}(\mathbf{r})$. We can achieve this by considering the following linear combination of atomic

spatial orbitals:

$$\begin{aligned}
\psi_{n_C, \mathbf{k}}(\mathbf{r}) &= N \sum_I e^{i\mathbf{k} \cdot \mathbf{R}_{I, n_C}} \phi_{n_C}(\mathbf{r} - \mathbf{R}_{I, n_C}) \\
&= N_a e^{i\mathbf{k} \cdot \mathbf{r}} N_b \sum_I e^{-i\mathbf{k} \cdot (\mathbf{r} - \mathbf{R}_{I, n_C})} \phi_{n_C}(\mathbf{r} - \mathbf{R}_{I, n_C}) \\
&\equiv N_a e^{i\mathbf{k} \cdot \mathbf{r}} \mu_{n_C, \mathbf{k}}(\mathbf{r}),
\end{aligned} \tag{4.6}$$

where $N = N_a N_b$ is a normalization constant, with $N_a = 1/\sqrt{V}$ and $N_b = \sqrt{\Omega}$ (see Appendix 4.A for the derivation). In order to prove that $\psi_{n_C, \mathbf{k}}(\mathbf{r})$ constructed above is indeed a Bloch wave, we must show that $\mu_{n_C, \mathbf{k}}(\mathbf{r})$ exhibits the same periodicity as the lattice. Let \mathbf{R} denote some lattice displacement:

$$\begin{aligned}
\mu_{n_C, \mathbf{k}}(\mathbf{r} + \mathbf{R}) &= N_b \sum_I e^{-i\mathbf{k} \cdot (\mathbf{r} - \mathbf{R}_{I, n_C} + \mathbf{R})} \phi_{n_C}(\mathbf{r} - \mathbf{R}_{I, n_C} + \mathbf{R}) \\
&= N_b \sum_J e^{-i\mathbf{k} \cdot (\mathbf{r} - \mathbf{R}_{J, n_C})} \phi_{n_C}(\mathbf{r} - \mathbf{R}_{J, n_C}) \\
&= \mu_{n_C, \mathbf{k}}(\mathbf{r}),
\end{aligned} \tag{4.7}$$

where we used the fact that all cells are identical, resulting in a periodic behavior of the wave functions $\phi_{n_C}(\mathbf{r} - \mathbf{R}_{I, n_C})$. Furthermore, we define the index J such that $\mathbf{R}_{J, n_C} = \mathbf{R}_{I, n_C} - \mathbf{R}$. Since I and J run over all unit cells, they contain the same terms.

Having constructed our hybrid basis, we may insert our ansatz, Eq. (4.5), into the Schrödinger equation. This immediately yields

$$\begin{aligned}
&\sum_m \left[\frac{1}{2}(\mathbf{k} + \mathbf{K}_m)^2 + \sum_j W(\mathbf{K}_j) e^{i\mathbf{K}_j \cdot \mathbf{r}} \right] \frac{1}{\sqrt{V}} v_{n, \mathbf{k}}(\mathbf{K}_m) e^{i(\mathbf{k} + \mathbf{K}_m) \cdot \mathbf{r}} \\
&+ \sum_{n_C} E_{n_C} w_{n, \mathbf{k}}(n_C) \psi_{n_C, \mathbf{k}}(\mathbf{r}) \\
&= E_{n, \mathbf{k}} \left[\frac{1}{\sqrt{V}} \sum_m v_{n, \mathbf{k}}(\mathbf{K}_m) e^{i(\mathbf{k} + \mathbf{K}_m) \cdot \mathbf{r}} + \sum_{n_C} w_{n, \mathbf{k}}(n_C) \psi_{n_C, \mathbf{k}}(\mathbf{r}) \right].
\end{aligned} \tag{4.8}$$

For the core wave functions, we used $\hat{H} \psi_{n_C, \mathbf{k}}(\mathbf{r}) = E_{n_C} \psi_{n_C, \mathbf{k}}(\mathbf{r})$, where the energy eigenvalue of the core electrons, E_{n_C} , is independent of \mathbf{k} , because these core electrons are highly localized. We subsequently project this onto our hybrid basis and solve the Schrödinger equation through a matrix diagonalization.

Performing a projection onto the plane-wave part of our basis, we calculate $\langle \mathbf{k} + \mathbf{K}_i | \hat{H} | \varphi_{n, \mathbf{k}} \rangle$. Keeping in mind the proper normalization of our plane

waves, $\langle \mathbf{r} | \mathbf{k} \rangle = e^{i\mathbf{k} \cdot \mathbf{r}} / \sqrt{V}$, and using $\int_V d^3r e^{i(\mathbf{K}_i - \mathbf{K}_j) \cdot \mathbf{r}} = V \delta_{ij}$, this yields

$$\begin{aligned} & \frac{1}{2}(\mathbf{k} + \mathbf{K}_i)^2 v_{n,\mathbf{k}}(\mathbf{K}_i) + \sum_j v_{n,\mathbf{k}}(\mathbf{K}_j) W(\mathbf{K}_i - \mathbf{K}_j) \\ & + \sum_{n_C} E_{n_C} w_{n,\mathbf{k}}(n_C) \langle \mathbf{k} + \mathbf{K}_i | \psi_{n_C, \mathbf{k}} \rangle \\ & = E_{n,\mathbf{k}} \left[v_{n,\mathbf{k}}(\mathbf{K}_i) + \sum_{n_C} w_{n,\mathbf{k}}(n_C) \langle \mathbf{k} + \mathbf{K}_i | \psi_{n_C, \mathbf{k}} \rangle \right], \quad \text{for } i = 1, \dots, N_{\mathbf{K}}. \end{aligned} \quad (4.9)$$

Performing a projection onto the core-wave-function part of our basis, we calculate $\langle \psi_{n_C, \mathbf{k}} | \hat{H} | \varphi_{n, \mathbf{k}} \rangle$. By using the fact that $\psi_{n_C, \mathbf{k}}$ is an eigenstate of the Hamiltonian \hat{H} , with the eigenvalue E_{n_C} , we find that $\langle \psi_{n_C, \mathbf{k}} | \hat{H} | \varphi_{n, \mathbf{k}} \rangle = E_{n_C} \langle \psi_{n_C, \mathbf{k}} | \varphi_{n, \mathbf{k}} \rangle$, or

$$\begin{aligned} & E_{n_C} [v_{n,\mathbf{k}}(\mathbf{K}_i) \langle \psi_{n_C, \mathbf{k}} | \mathbf{k} + \mathbf{K}_i \rangle + w_{n,\mathbf{k}}(n_C)] \\ & = E_{n,\mathbf{k}} [v_{n,\mathbf{k}}(\mathbf{K}_i) \langle \psi_{n_C, \mathbf{k}} | \mathbf{k} + \mathbf{K}_i \rangle + w_{n,\mathbf{k}}(n_C)], \quad \text{for } i = 1, \dots, N_{\mathbf{K}}. \end{aligned} \quad (4.10)$$

We can combine these equations into a generalized eigenvalue equation, similar to the Roothaan-Hall equations [153, 154] of the form $\mathbf{F}\mathbf{C} = \mathbf{S}\mathbf{C}\mathbf{\Lambda}$, where $\mathbf{\Lambda} = \text{diag}(E_{n,\mathbf{k}})$. The n th column of \mathbf{C} is

$$(\mathbf{C})_n = \begin{pmatrix} v_{n,\mathbf{k}}(\mathbf{K}_1) \\ v_{n,\mathbf{k}}(\mathbf{K}_2) \\ \vdots \\ v_{n,\mathbf{k}}(\mathbf{K}_{N_{\mathbf{K}}}) \\ - - - \\ w_{n,\mathbf{k}}(n_C = 1) \\ w_{n,\mathbf{k}}(n_C = 2) \\ \vdots \\ w_{n,\mathbf{k}}(n_C = N_C) \end{pmatrix}, \quad (4.11)$$

and \mathbf{F} and \mathbf{S} are

$$\mathbf{F} = \left(\begin{array}{c|c} \frac{1}{2}(\mathbf{k} + \mathbf{K}_i)^2 \delta_{ij} + W(\mathbf{K}_i - \mathbf{K}_j) & E_{n_C=j} \langle \mathbf{k} + \mathbf{K}_i | \psi_{n_C=j, \mathbf{k}} \rangle \\ \hline E_{n_C=i} \langle \psi_{n_C=i, \mathbf{k}} | \mathbf{k} + \mathbf{K}_j \rangle & E_{n_C=i} \delta_{ij} \end{array} \right), \quad (4.12)$$

$$\mathbf{S} = \left(\begin{array}{c|c} \delta_{ij} & \langle \mathbf{k} + \mathbf{K}_i | \psi_{n_C=j, \mathbf{k}} \rangle \\ \hline \langle \psi_{n_C=i, \mathbf{k}} | \mathbf{k} + \mathbf{K}_j \rangle & \delta_{ij} \end{array} \right), \quad (4.13)$$

with i and j denoting rows and columns, respectively. Note that we have one such equation $\mathbf{F}\mathbf{C} = \mathbf{S}\mathbf{C}\mathbf{A}$ per \mathbf{k} point. It should come as no surprise to encounter equations similar to the Roothaan-Hall equations as these are a representation of the Hartree-Fock equations in a nonorthonormal basis, precisely as we have done with our hybrid basis consisting of plane waves and atomic orbitals.

Note that the theory developed in Sec. 4.2.2 assumed nothing more than a periodic potential $V(\mathbf{r})$, and a one-electron description for the electron wave function under consideration, with the ansatz given in Eq. (4.5). At this point we would like to emphasize that, even though we will not consider it in this work, it is possible to include molecular dynamics in this framework, so as to extend the applicability of XCRYSTAL to beyond the timescale of ~ 100 fs after x-ray irradiation. Conceptually, we need not take the assumption of periodicity to imply the use of a crystallographic unit cell as is done in this work. A larger supercell containing many more atoms could be employed. However, this would cause the Brillouin zone to shrink, rendering the matrices that must be diagonalized much larger. Under these conditions, employing the Bloch theorem in combination with a plane-wave basis may no longer be the most efficient approach. We leave this development and investigation for a future endeavor.

4.2.3 Calculation of atomic orbitals

In order to calculate the atomic orbitals needed for the construction of $\psi_{n_C, \mathbf{k}}(\mathbf{r})$, we used the XATOM toolkit [43, 79, 95]. This toolkit describes an isolated many-electron atom in a Hartree-Fock-Slater (HFS) framework. This is an independent-particle approximation with a mean-field Hamiltonian of the form

$$\begin{aligned} \hat{H}_{\text{HFS}} &= -\frac{1}{2}\nabla^2 + V(\mathbf{r}), \\ &= -\frac{1}{2}\nabla^2 - \frac{Z}{|\mathbf{r}|} + \int d^3r' \frac{\rho(\mathbf{r}')}{|\mathbf{r} - \mathbf{r}'|} + V_{\text{exc}}(\mathbf{r}), \end{aligned} \quad (4.14)$$

where Z is the nuclear charge. The exchange potential $V_{\text{exc}}(\mathbf{r})$ is assumed to be of the form [98]

$$V_{\text{exc}}(\mathbf{r}) = -\frac{3}{2} \left[\frac{3}{\pi} \rho(\mathbf{r}) \right]^{1/3}, \quad (4.15)$$

with $\rho(\mathbf{r}) = \sum_i^{\text{occ}} \phi_i^\dagger(\mathbf{r})\phi_i(\mathbf{r})$ being the electron density, and $\phi_i(\mathbf{r})$ denoting a single-particle spin-orbital wave function. In addition, XATOM imposes spherical symmetry, assuming the solution of the Schrödinger equation to be of the form

$$\phi_{nlms}(\mathbf{r}) = \frac{u_{nl}(r)}{r} Y_{lm}(\Omega_{\mathbf{r}}) \begin{pmatrix} \delta_{s,+1/2} \\ \delta_{s,-1/2} \end{pmatrix}, \quad (4.16)$$

with n , l , m , and s being the principal, azimuthal, magnetic, and spin quantum numbers of the electron with the associated wave function $\phi_{nlms}(\mathbf{r})$, respectively. A spherical averaging is done on the electronic density. This implies that both the electronic density and potential are spherically symmetric, such that $\rho(\mathbf{r}) = \rho(r)$ and $V(\mathbf{r}) = V(r)$. Subsequently, XATOM solves the Schrödinger equation in a self-consistent way. There are numerous computational input parameters required in XATOM calculations [43], the most relevant of which are the following. The radial coordinate r in Eq. (4.16) is defined with the generalized pseudospectral method on a nonuniform grid [100]. This grid is characterized by the number of radial grid points N_r , the maximum radius, r_{max} , and the mapping parameter L , which determines the density distribution of radial points [100]. A larger L invokes that more radial grid points are being pushed towards higher values of r . For the computations of the atomic orbitals presented further, we used $N_r = 200$, $L = 10$, and $r_{max} = 5.0 a_0$, unless specified otherwise. Since XATOM calculates the atomic orbitals in an isolated-atom description, these orbitals will not be accurate representations of orbitals in a charged and dense environment of atoms. We show how we adapt the core orbitals to the environment in Sec. 4.2.6. Let us continue by explaining exactly how we define the *core* atomic orbitals $\phi_{n_C}(\mathbf{r})$ in the framework of XCRYSTAL.

As we intend to work with the atomic orbitals provided by XATOM, which are calculated in a sphere of size r_{max} , we also construct spheres around the constituent atoms located within our unit cell. The radius of the sphere for atom a will be denoted by $r_s(a)$. In order to be able to maximally exploit spherical symmetry, we assume the spheres to be touching each other. The values of $r_s(a)$ are then dependent on the crystal geometry. From all orbitals obtained with XATOM, we include only those orbitals into our hybrid basis which are localized within the touching spheres. Thus, we define our *core orbitals* as those that satisfy

$$\left| 1 - \int_0^{r_C(a)} dr |u_{a,nl}(r)|^2 \right| \leq \delta_C, \quad (4.17)$$

where δ_C is a cutoff parameter set to 10^{-3} for all calculations shown in this work. This implies that at least 99.9% of the norm of the core orbitals of atom a is confined to the sphere of radius $r_C(a)$. The radius $0 < r_C(a) \leq r_s(a)$ is a model-dependent parameter. The reason for the

inclusion of $r_C(a)$ is that in the upcoming Sec. 4.2.4, we assume a model to describe our periodic crystal where we disembark from static, touching spheres.

4.2.4 Construction of the crystal potential

Having conceptualized touching spheres of radii $r_s(a)$ around our atoms, we may describe our system using a muffin-tin-type potential [121, 150, 151]. Inside of the spheres, a spherically symmetric potential $V_a(|\mathbf{r} - \mathbf{R}_a|)$ is assumed, where \mathbf{R}_a is the position vector of the a th atom. Outside of the spheres, in the interstitial region, the potential becomes a constant, V_0 . Typically, this potential is set to zero [117, 150, 151, 155–157]. However, we will follow Ref. [121] in explicitly calculating V_0 . In Ref. [121], V_0 is the potential value at the Wigner-Seitz radius and denotes the energy value above which the continuum of states starts. In our framework, we do not have a similar physical meaning behind V_0 . What remains true is that a continuum of delocalized states will be present at energies above V_0 in XCRYSTAL. However, there may also be some delocalized states below V_0 , evidently referring to states that are somewhat localized, yet not enough to be considered core orbitals as they do not satisfy Eq. (4.17). To determine the value of V_0 , we require the value of the potential on the boundaries of the spheres to be equal. We know that the potentials in the spheres are $\sim C/r$ for some $C < 0$. Therefore, for all our touching spheres, we assign $V_0 = \min\{V_a(r_s)\}$ and proceed by shrinking all spheres to a radius $r_V(a)$ so that $V_a(r_V) = V_0$. In this framework, this implies that in $r_C(a) = r_V(a)$ in Eq. (4.17).

The reason for adopting the muffin-tin potential into our framework is two fold: (1) the implementation of a spherically symmetric potential inside of a sphere can be accurately captured by the available XATOM toolkit, and (2) the muffin-tin potential simplifies the evaluation of the Fourier transform $W(\mathbf{K}) = \frac{1}{\Omega} \int_{\Omega} d^3r e^{-i\mathbf{K} \cdot \mathbf{r}} V(\mathbf{r})$ in Eq. (4.12), reducing a three-dimensional integral to a one-dimensional one:

$$\begin{aligned}
 W(\mathbf{K}) &= \frac{1}{\Omega} \int_{\Omega} d^3r e^{-i\mathbf{K} \cdot \mathbf{r}} V(\mathbf{r}) \\
 &= \frac{1}{\Omega} \sum_a e^{-i\mathbf{K} \cdot \mathbf{R}_a} \int_{Sph,a} d^3(|\mathbf{r} - \mathbf{R}_a|) e^{-i\mathbf{K} \cdot (\mathbf{r} - \mathbf{R}_a)} V_a(|\mathbf{r} - \mathbf{R}_a|) \\
 &\quad + V_0 \left[\frac{1}{\Omega} \int_{\Omega} d^3r e^{-i\mathbf{K} \cdot \mathbf{r}} - \frac{1}{\Omega} \sum_a e^{-i\mathbf{K} \cdot \mathbf{R}_a} \right. \\
 &\quad \left. \times \int_{Sph,a} d^3(|\mathbf{r} - \mathbf{R}_a|) e^{-i\mathbf{K} \cdot (\mathbf{r} - \mathbf{R}_a)} \right]
 \end{aligned}$$

$$\begin{aligned}
&= \frac{1}{\Omega} \sum_a e^{-i\mathbf{K} \cdot \mathbf{R}_a} \int_{Sph,a} d^3(|\mathbf{r} - \mathbf{R}_a|) e^{-i\mathbf{K} \cdot (\mathbf{r} - \mathbf{R}_a)} V_a(|\mathbf{r} - \mathbf{R}_a|) \\
&\quad + V_0 \left\{ \delta_{\mathbf{K},0} - \frac{1}{\Omega} \sum_a e^{-i\mathbf{K} \cdot \mathbf{R}_a} \right. \\
&\quad \left. \times \frac{4\pi}{K^3} [\sin(Kr_{V,a}) - Kr_{V,a} \cos(Kr_{V,a})] \right\}. \tag{4.18}
\end{aligned}$$

The inclusion of the muffin-tin crystal potential into Eq. (4.18) allowed us to split up the integral over the unit cell into two parts: the atomic region and the interstitial region, as schematically illustrated in Fig. 4.1. In the atomic

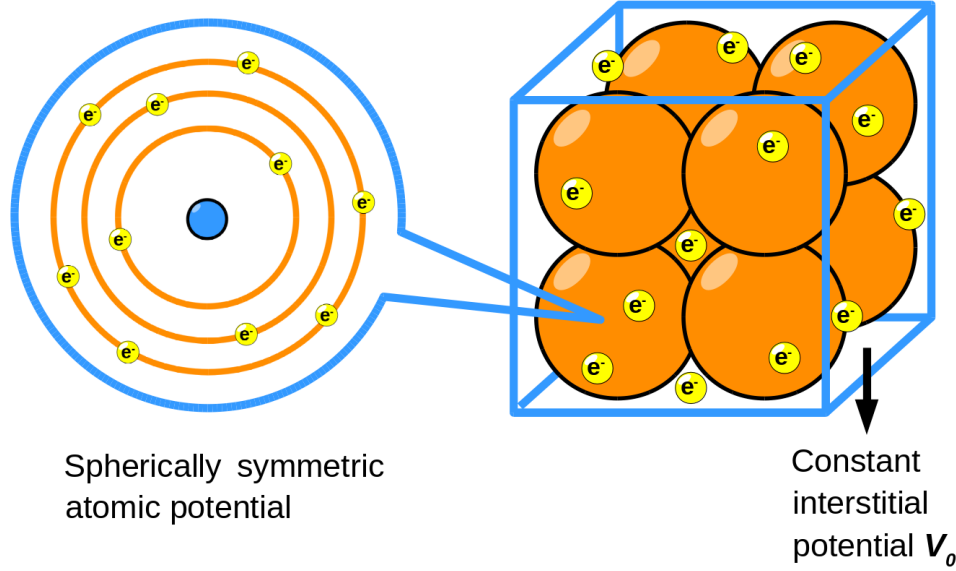


Figure 4.1: Schematic illustration of the calculation setup in XCRYSTAL.

region, the integral is represented as a sum of spherical integrals (in one dimension), whereas in the interstitial region the integral can be evaluated analytically. The latter is highly beneficial for computational efficiency. The spherically symmetric atomic potential $V_a(r)$, used in Eq. (4.18), is given by

$$V_a(r) = -\frac{Z_a}{r} + \int_{Sph,a} d^3r' \frac{\rho(r')}{|\mathbf{r} - \mathbf{r}'|} - \frac{3}{2} \left[\frac{3}{\pi} \rho(r) \right]^{1/3}. \tag{4.19}$$

Given the limitations on accuracy imposed by the simple muffin-tin approximation, using a higher quality exchange-correlation functional than the one alluded to in Eqs. (4.15) and (4.19) is not warranted. We have made the assumption that the electronic density ρ is also spherically symmetric inside of the spheres. The respective spherical averaging was done as $\rho(r) = \int d\Omega_{\mathbf{r}} \rho(\mathbf{r}) / \int d\Omega_{\mathbf{r}}$ and may be evaluated analytically. Note that

the assumption of a spherically averaged electronic density may be a poor approximation for capturing the electronic behavior at low temperatures for materials that exhibit directional bonding. However, we may expect any directional dependencies to be suppressed once the electronic temperature exceeds the zero-temperature band gap, allowing for thermal excitations. This will make the approximation of a spherically averaged electronic density less crude at these temperatures.

4.2.5 Electronic density at finite temperature

Within a finite-temperature HFS framework, the temperature is introduced assuming Fermi-Dirac occupation of the electronic orbitals [158]. Therefore, at temperature T and chemical potential μ , the electron density $\rho(\mathbf{r})$ is calculated as $\sum_p |\varphi_p(\mathbf{r})|^2 \bar{n}_p(\mu, T)$, with p being a spin-orbital index, φ_p the electron wave function, and $\bar{n}_p(\mu, T)$ a Fermi statistical weight. For the atomic core orbitals, the index $p = n_C$ (as defined in Sec. 4.2.2), and for the delocalized valence orbitals $p = (n, \mathbf{k}, s)$. We assume a degeneracy in the energies with regard to the spin quantum number, so a sum over the spins s will simply lead to a factor of 2. The Fermi weight at T is

$$\bar{n}_p(\mu, T) = \frac{1}{e^{\beta(\varepsilon_p - \mu)} + 1}, \quad (4.20)$$

where ε_p is the energy eigenvalue associated with φ_p , $\beta = 1/T$, and μ is the chemical potential of the system. The chemical potential is calculated by imposing charge neutrality on our unit cell. To find μ , we must solve

$$\begin{aligned} \sum_a Z_a - \sum_p \left[\int_{\Omega} d^3r |\varphi_p(\mathbf{r})|^2 \right] \bar{n}_p(\mu, T) &= 0, \\ \sum_a Z_a - \frac{1}{N_{\text{cell}}} \sum_p \bar{n}_p(\mu, T) &= 0, \end{aligned} \quad (4.21)$$

where we used the fact that $\varphi_p(\mathbf{r})$ is normalized to 1 in the total volume V . Since $|\varphi_p(\mathbf{r})|^2$ is a periodic function, $\varphi_p(\mathbf{r})$ is normalized to $1/N_{\text{cell}}$ in the unit cell Ω .

4.2.6 Self-consistent-field method

In the self-consistent-field (SCF) method, we start with an initial guess for the spherically symmetric electronic density $\rho(r)$. The initial guess can be based, for example, on the converged XATOM result for the initial atomic orbitals. This is the typical start for calculations at zero temperature. At nonzero temperatures, we may use the density calculated at a lower temperature, or even extrapolate the results from several lower-temperature runs.

With the initial density, we construct the potentials $V_a(r)$ as in Eq. (4.19), and perform the sphere shrinking in order to calculate V_0 (explained in

Sec. 4.2.4). At this point, instead of keeping our core orbitals fixed, we use the newly obtained muffin-tin potential in a single XATOM diagonalization in order to update the atomic core orbitals. Therefore, during the SCF iteration, the core orbitals, which are incorporated in our hybrid basis, are always updated to the presence of valence electrons, in contrast to the conventional low-temperature condensed-matter calculations where *frozen* core orbitals are typically used. We do expect that in dense plasmas the core orbitals strongly react to the presence of plasma electrons, throughout the entire unit cell. After this core-orbital update, we proceed by using our previously obtained muffin-tin potential and Eq. (4.18) to obtain $W(\mathbf{K})$. It is then utilized in the Fock matrix \mathbf{F} in Eq. (4.12). Therein the quantities referring to the core orbitals, E_{n_C} and $\psi_{n_C, \mathbf{k}}(\mathbf{r})$, are the results from the *updated* core orbitals. Subsequently, the equation $\mathbf{FC} = \mathbf{SCA}$ is solved to obtain $\{\mathbf{A}, \mathbf{C}\}$.

From the solutions obtained for the core orbitals and the valence orbitals, we calculate the new electronic density $\rho(\mathbf{r}) = \rho_{\text{core}}(\mathbf{r}) + \rho_{\text{val}}(\mathbf{r})$, which is spherically averaged analytically. With this electronic density, we construct a new potential $V_a(r)$ and update V_0 , thereby closing the loop in the SCF method. The whole procedure is repeated until the result converges. Further discussion on the scheme used to accelerate the SCF convergence can be found in Appendix 4.B. An illustration depicting the SCF algorithm employed is shown in Fig. 4.2.

4.2.7 Numerical parameters for crystal calculations

In addition to the computational parameters related to atomic calculations, there is a couple of numerical parameters utilized in XCRYSTAL, which are related to the crystal structure. They are (1) the cutoff on the number of reciprocal lattice vectors used and (2) the numerical grid defined for the momentum vectors in the first Brillouin zone (BZ).

The sum over reciprocal lattice vectors \mathbf{K}_i , used in the Fourier series should in principle be infinite and include all possible vectors $\{\mathbf{K}_i\}$. For practical purposes, a cutoff on the number of reciprocal lattice vectors, denoted by $N_{\mathbf{K}}$ (in Sec. 4.2.2), is indirectly imposed through a cutoff on the norm of the vectors, denoted by $|\mathbf{K}|_{\text{max}}$. As can be seen from the coupling term $W(\mathbf{K}_i - \mathbf{K}_j)$ in the Fock matrix \mathbf{F} in Eq. (4.12), the quantity $|\mathbf{K}|_{\text{max}}$ determines the energy cutoff for the bands. At $T = 0$ eV we may expect to achieve convergence with a relatively low $|\mathbf{K}|_{\text{max}}$, as the absence of thermal excitations implies that higher-lying bands will remain unoccupied. However, by increasing the temperature, the number of thermal excitations will rise, and a higher cutoff on $|\mathbf{K}|_{\text{max}}$ will be necessary to attain convergence. As one increases $|\mathbf{K}|_{\text{max}}$, additional plane waves are added to our hybrid basis with increasingly higher momenta. It may occur that these are high enough so as to describe the atomic core orbitals in our basis, and a linear

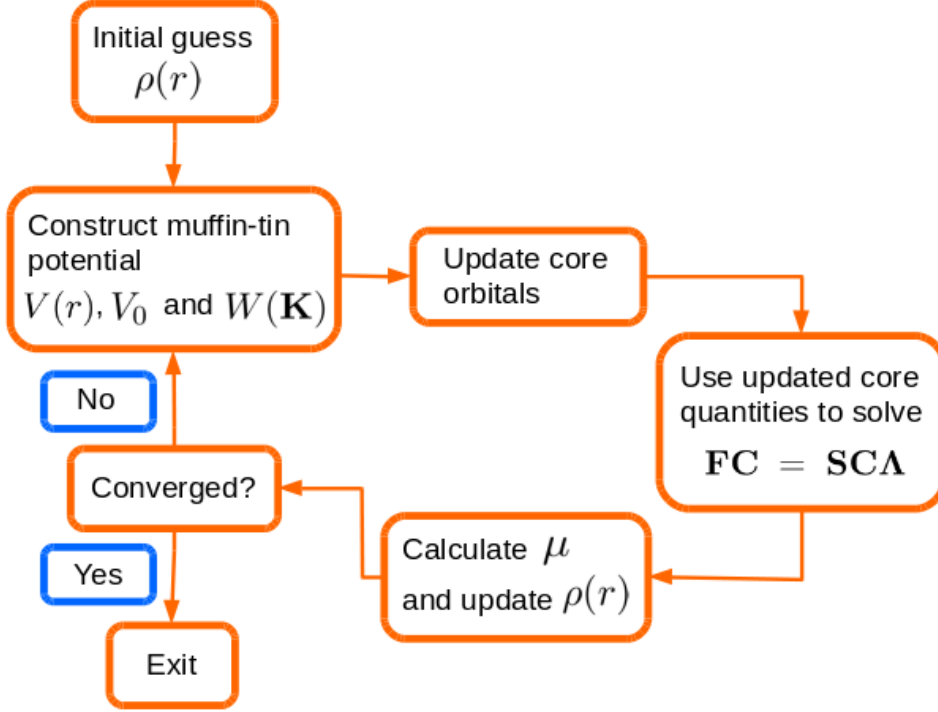


Figure 4.2: Schematic illustration of the algorithm used in XCRYSTAL.

dependency will ensue. In this case, a simple rank reduction is used on the matrices \mathbf{F} , \mathbf{S} , and \mathbf{C} to remove this linear dependency. For consistency between results at various temperatures, all XCRYSTAL calculations were done using $|\mathbf{K}|_{\max} = 6.0 \text{ } a_0^{-1}$, which corresponds to $N_{\mathbf{K}} = 1647$ valence bands.

The second parameter of interest defines the numerical grid defined for the momentum vectors in the first Brillouin zone and affects the sum over momentum vectors \mathbf{k} . Because of our employed Bloch formalism, the sums over \mathbf{k} are restricted to the momentum vectors confined within the first Brillouin zone (BZ) of the reciprocal lattice. However, contrary to the reciprocal lattice vectors $\{\mathbf{K}_i\}$, the vectors \mathbf{k} in the first BZ constitute an uncountable set. Therefore, a sum over vectors \mathbf{k} is performed as an integral: $\sum_{\mathbf{k}}^{BZ} = V(2\pi)^{-3} \int_{BZ} d^3k$. To perform this integral numerically, a grid is defined inside the first BZ. Through a dedicated analysis, we have found a \mathbf{k} grid of $7 \times 7 \times 7$ to be sufficient for achieving convergence. A more elaborate discussion on the employed BZ will be given in Sec. 4.3.

4.3 Results

In this section we show results obtained with XCRYSTAL for x-ray-excited solid Al, investigated experimentally in Refs. [34, 61]. This experiment was

conducted at the LCLS [34, 61] for solid Al at a density of 2.7 g/cm^3 . The sample reached electronic temperatures in the range of $T = 10\text{--}80 \text{ eV}$. The $K\alpha$ fluorescence signal was measured as a function of the incoming photon energy. After comparing the results calculated by XCRYSTAL to experiment, we will show band structure plots of this system. At zero temperature, these can be compared to known, well-established result [159, 160], whereas the band diagrams at higher temperatures will be of interest with regard to how they evolve as temperature is increased to values characteristic of WDM conditions (up to 100 eV or 10^6 K). To the best of our knowledge, these temperature-dependent electronic band structures at such high temperatures are the first of their kind for this nonisothermal, transient WDM state.

The Al crystal has a face-centered-cubic (FCC) structure, for which the primitive unit cell can be constructed from the primitive lattice vectors $\mathbf{a}_1 = a(1/2, 0, 1/2)$, $\mathbf{a}_2 = a(0, 1/2, 1/2)$, $\mathbf{a}_3 = a(1/2, 1/2, 0)$, where $a = 404.95 \times 10^{-12} \text{ m} = 7.652 a_0$ is the lattice constant of Al. The first Brillouin zone (BZ) is a truncated octahedron. Due to the implementation of the Bloch formalism, every sum over momentum vectors \mathbf{k} can be limited to this first Brillouin zone. However, for modeling this system in XCRYSTAL, it was numerically more efficient to define the unit cell to be cubic, with lattice vectors $\mathbf{a}_1 = a(1, 0, 0)$, $\mathbf{a}_2 = a(0, 1, 0)$, $\mathbf{a}_3 = a(0, 0, 1)$, and four Al atoms placed on the positions $a(0, 0, 0)$, $a(1/2, 0, 1/2)$, $a(0, 1/2, 1/2)$, and $a(1/2, 1/2, 0)$, similar to what was done by Vinko *et al.* in Ref. [131]. In this manner, any sum over \mathbf{k} can be evaluated using a simple linear grid in the cubic BZ. However, our real-space unit cell has a larger volume than the primitive unit cell of FCC. This implies that the volume of our cubic BZ is smaller than the first BZ of FCC. At first glance, this seems to imply we have lost information on \mathbf{k} points that lie outside of our cubic BZ but are located inside the first BZ of FCC. However, our employed periodic Bloch formalism ensures that this is not the case: the \mathbf{k} -dependent quantities, such as $E_{n,\mathbf{k}}$, that lie in the first BZ of FCC, but outside of our cubic BZ are then shifted to a higher band, n . This effect will reveal itself explicitly in the band structure plots shown in Sec. 4.3.2.

The geometry of the defined crystal structure implies a radius of the touching spheres $r_s = 2.706 a_0$ for all atoms. Due to the high level of symmetry, we found that $r_V(a) = r_s = 2.706 a_0$ for all atoms, and for all temperatures considered. Thereby, in Eq. (4.17), $r_C(a) = r_s$, which defines the $1s$, $2s$, and $2p$ orbitals as the core orbitals. Note that through the use of thermal occupation numbers with a well-defined chemical potential and temperature in xcrystal as was mentioned in Sec. 4.2.5, we assume the electrons to be in perfect thermal equilibrium for the conditions in the LCLS experiment, which is merely an approximation.

4.3.1 K -shell thresholds and ionization potential depression

The LCLS experiment described in Refs. [34, 61] provides the data on the K -shell threshold energy. The K -shell threshold energy refers to the energy that is required for the formation of a K -shell ($1s$) hole. From the spectrally resolved $K\alpha$ -emission spectrum in Ref. [34], they could deduce this quantity by observing at which XFEL-photon energy the emission peak started. Additionally, each separate emission peak observed indicates a specific charge state Q of an Al ion, which this peak refers to. Therefore, we will consider the K -shell threshold energy as a function of charge state Q . In addition to a comparison with this experiment, we will compare the result of XCRYSTAL with the results from the AA model and the two-step-HFS model, both shown in Ref. [121]. As such, we will first elaborate on how the K -shell threshold energy and the charge state Q are defined in these three models.

In the AA model, a thermal averaging is employed, so an integer value of Q corresponding to a specific electronic configuration cannot be obtained. Instead, an average charge $\bar{Q}_{\text{AA}} = Z - N_b^{\text{AA}}(\beta, \mu)$ is obtained, with Z the charge of the neutral Al atom and $N_b^{\text{AA}}(\beta, \mu)$ the number of bound electrons. In Ref. [121] a muffin-tin potential is also employed, albeit with Wigner-Seitz spheres, and the flat potential provides a clear energetic distinction between bound orbitals and the continuum. Therefore, $N_b^{\text{AA}}(\beta, \mu)$ is calculated as the sum over the thermal occupations of orbitals with energies below the flat potential [see Eq. (4.22a)]. The K -shell threshold energy is calculated as the energy difference between the $1s$ orbital and the lowest-lying orbital above the flat potential. To be complete, there are two subtleties: (1) if the chemical potential μ is larger than the flat potential, the K -shell threshold energy is calculated as $\mu - \varepsilon_{1s}$ to make sure the orbital being excited into is vacant, and (2) at higher temperatures, the $3p$ orbital drops below the flat potential and a $1s$ electron can be excited into it. In this case, the K -shell threshold energy is $\varepsilon_{3p} - \varepsilon_{1s}$. This definition for the K -shell threshold energy is also used in the two-step-HFS method [121]. However, the two-step-HFS model is capable of specifying integer charge states, as it uses an AA calculation in its first step to define a thermal grand-canonical ensemble and proceeds in its second step by working with the most likely electronic configuration for a specific integer charge state Q . In contrast to this, but similar to the AA model, XCRYSTAL also works with a thermally averaged, and atom-specific, charge state $\bar{Q}_{\text{XCRY}}(a)$. However, our flat potential V_0 does not share the same physical interpretation as the flat potential used in Ref. [121], as delocalized states can be found below V_0 in XCRYSTAL. Therefore, we calculate $\bar{Q}_{\text{XCRY}}(a) = Z(a) - N_b^{\text{XCRY}}(\beta, \mu, a)$, with the number of bound electrons of atom a , $N_b^{\text{XCRY}}(\beta, \mu, a)$, calculated as the sum of the

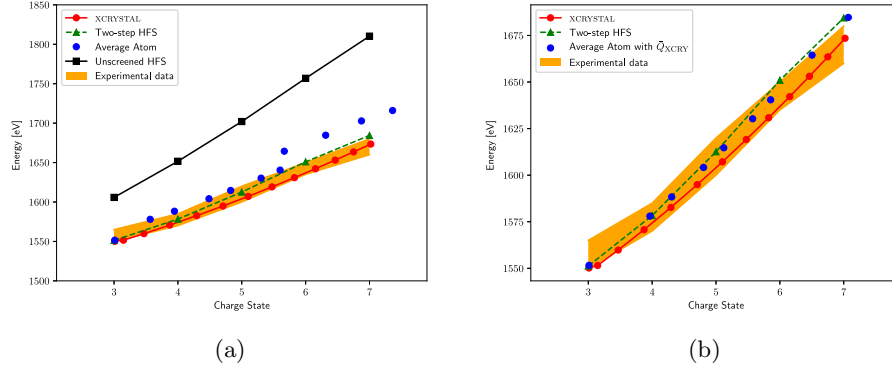


Figure 4.3: (a) K -shell threshold for Al as a function of the charge state, calculated using XCRYSTAL. A comparison is shown with the two-step-HFS result and the average-atom result from Ref. [121], as well as with the experimental data from Ref. [61]. Calculations using an isolated Al ion are labeled as “Unscreend HFS.” (b) K -shell threshold for Al as a function of the charge state, calculated using XCRYSTAL, the two-step-HFS result [121], and the average-atom result with \bar{Q} defined as in XCRYSTAL [Eq. (4.22b)]. The experimental data from Ref. [61] is shown as well.

thermal occupations of the core orbitals ($1s$, $2s$, and $2p$). In summary,

$$N_b^{\text{AA}}(\beta, \mu) = \sum_{p \leq V_0^{\text{AA}}} \frac{1}{e^{\beta(\varepsilon_p - \mu)} + 1} \quad \text{for AA}, \quad (4.22a)$$

$$N_b^{\text{XCRY}}(\beta, \mu, a) = \sum_{\substack{p=(n,l,m,s) \\ n=1,2}} \frac{1}{e^{\beta(\varepsilon_p - \mu)} + 1} \quad \text{for XCRYSTAL}, \quad (4.22b)$$

where V_0^{AA} is the flat potential in the AA model and $p = (n, l, m, s)$ for a fixed a . Due to the translational symmetry in the crystal, we found the average charge $\bar{Q}_{\text{XCRY}}(a)$ for each ion to be the same, for a given temperature T . The $K\alpha$ fluorescence energies employed in Refs. [34, 61] to assign atomic charges to spectroscopic features are sensitive primarily to K - and L -shell occupation numbers. The choice made in Eq. (4.22b) is consistent with this property. As for the K -shell threshold energy, it refers to the energy that is required for the formation of a K -shell ($1s$) hole by exciting a $1s$ electron into the lowest-lying, vacant, delocalized valence orbital. In the convention employed here, the K -threshold corresponds to the energy difference between the $1s$ orbital and the lowest-lying orbital that has a thermal occupation of ≤ 0.5 and that is associated with a nonzero bandwidth. Note that this definition is equivalent to the one employed in Ref. [121].

In Fig. 4.3(a), we plot the K -shell threshold energy as a function of

charge state Q calculated with XCRYSTAL and compare it to the experimental data [61], as well as to the theoretical models mentioned previously [121]. For both the AA model and the XCRYSTAL result, the average charge \bar{Q} for each method, as defined previously, is portrayed on the x axis. The \bar{Q} values shown correspond to a temperature range of 10–90 eV and 10–70 eV for the AA model and XCRYSTAL, respectively. The XCRYSTAL results were shifted by +20.92 eV, similar to what was done in Ref. [121]. This shift corresponds to the difference between the ionization potential calculated at $T = 0$ eV with XCRYSTAL (1538.68 eV) and the experimentally estimated binding energy (1559.60 eV) [161]. As shown in Fig. 4.3(a), XCRYSTAL is capable of reproducing the result for the K -shell threshold energy for all charge states considered.

The improvement of the XCRYSTAL result with respect to the AA result alone seemingly implies that this improvement is due to the incorporation of the full crystal structure in XCRYSTAL. However, the two-step-HFS model does not take the crystal structure into account and yet shows excellent agreement with experiment as well, through its individual configuration optimization. To shed some light on how large the effects of incorporating a full crystal structure are, we may dismiss their inclusion in XCRYSTAL. This simply amounts to an AA calculation, where the average charge is calculated as \bar{Q}_{XCRY} , i.e., the thermal occupations of the $1s$, $2s$, and $2p$ orbitals subtracted from the nuclear charge of Al. We show this result in Fig. 4.3(b). The temperature range for the AA result shown in Fig. 4.3(b) is 10–80 eV. Comparing the AA result between Fig. 4.3(a) and Fig. 4.3(b), we conclude that the discrepancy between experiment and the AA method shown in Ref. [121] is not so much a limitation of the applicability of the AA model, but rather a consequence of the definition of \bar{Q}_{AA} used in Ref. [121].

To further strengthen this claim, we may consider \bar{Q}_{AA} and $\bar{Q}_{\text{XCRY}}(a)$ for a single Al ion as a function of the electronic temperature, depicted in Fig. 4.4. Initially, \bar{Q}_{AA} increases with rising temperature as the bound orbitals are being partially thermally vacated. However, as the temperature increases, the previously unbound $3s$ and $3p$ orbitals fall below the flat potential V_0^{AA} [121] and count as bound states. This causes a sudden large contribution to the number of bound electrons, thereby decreasing the average charge \bar{Q}_{AA} below what one would expect if such a sudden addition of new bound orbitals had not taken place. The discontinuities at $T = 20$ eV ($\bar{Q}_{\text{AA}} \sim 3.0$) and $T = 58$ eV ($\bar{Q}_{\text{AA}} \sim 5.5$) shown in Fig. 4.4 directly result in the bumps for the K -shell threshold energy in Fig. 4.3(a), seen at these same values of \bar{Q} . In contrast, \bar{Q}_{XCRY} does not exhibit these sudden drops. The increase in average charge arises solely from gradually thermally vacating the core orbitals. This analysis, along with the results shown in Fig. 4.3(b), leads us to the conclusion that both the incorporation of the entire crystal structure, as well as individual configuration optimization, amount to a fairly limited effect overall. The property shared by the AA model, the

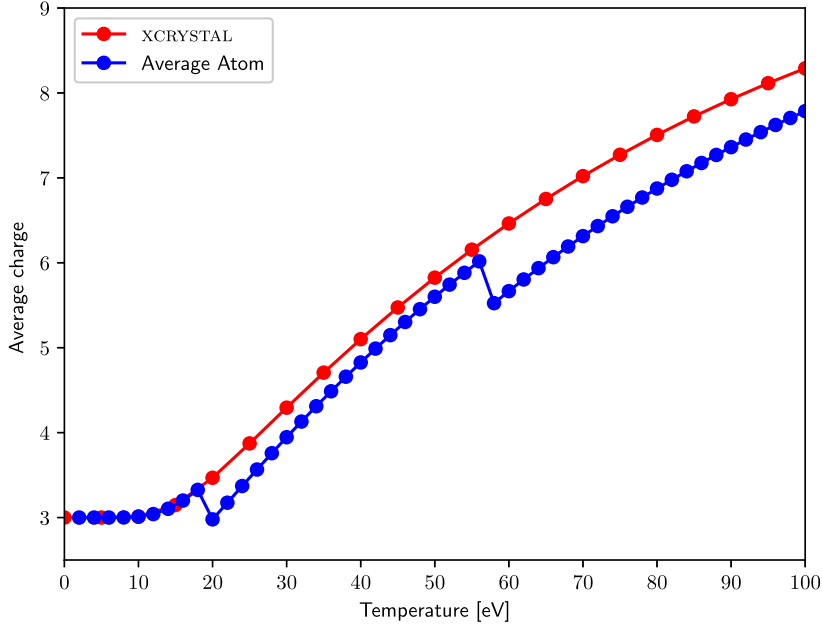


Figure 4.4: Average charge \bar{Q} versus the electronic temperature T obtained for the average-atom model and for XCRYSTAL.

two-step-HFS approach and XCRYSTAL is the optimization of core orbitals, to which we attribute the success of the three models.

We note that the work performed by Vinko *et al.* [131] seemingly contradicts this conclusion. Vinko *et al.* show an excellent agreement with the experiment of Ref. [61]. They used a plane-wave DFT calculation with a frozen-core pseudopotential determined at a fixed configuration and obtained values for the K -shell threshold energy using a Δ SCF scheme. The agreement with experiment was rationalized through their incorporation of a full three-dimensional electronic structure for the valence states and a lack of any spherical averaging. However, as both XCRYSTAL and the two-step-HFS model are able to adequately reproduce the experimental results of Ref. [61], which do incorporate both spherical and thermal averaging, we disagree with this proposed justification. The fact that Vinko *et al.* employed a frozen-core pseudopotential apparently contradicts our conclusion that core-orbital optimization is of vital importance. However, they do indirectly account for responsive core orbitals through their employment of a Δ SCF scheme to calculate the K -shell threshold energy. Explicitly, they calculate the difference in total free energy between a system with and without a single K -shell hole, accompanied by an additional number of L -shell

holes. Therefore, despite the $1s$ orbital being frozen in both configurations, their energies differ, resulting in an indirect response from the $1s$ core orbital to the K -shell threshold energy.

In order to illustrate the efficiency of our hybrid-basis approach, we compare numerical parameters of XCRYSTAL with the work done by Vinko *et al.* [131]. They considered high-energy bands with energies up to at least ten times the considered electronic temperature. Because of the high computational cost, they were incapable of making all temperature calculations with a single fixed $N_{\mathbf{K}}$ (see Sec. 4.2.2); instead the number of bands ranged from ~ 160 bands at $T = 10$ eV to ~ 5000 bands at $T = 100$ eV. The computational expense in the latter case was reported to exceed ~ 190 CPU days for a four-atom supercell containing 25 electrons. One should note that this cell did not contain all the electrons of a charge-neutral system containing four Al atoms, $4 \times Z(\text{Al}) = 52$, because of the employed pseudopotential formalism which used frozen, and not completely filled, core orbitals. In contrast, using XCRYSTAL we performed full all-electron calculations with 52 electrons. All calculations were consistently done with $|\mathbf{K}|_{\text{max}} = 6.0 a_0^{-1}$, corresponding to $N_{\mathbf{K}} = 1647$ bands. We found that this number of bands ($1647 < \sim 5000$) was sufficient to obtain converged XCRYSTAL results. Every temperature run could be completed within 72 CPU days for a four-atom unit cell containing 52 electrons. Additional parallelization of XCRYSTAL further reduced the calculation time to ~ 18 days with four CPU cores.

Finally, we present our result for the IPD of this system. For the $1s$ orbital, this is defined as the difference between the result from the HFS calculation for an unscreened (isolated ion) and the K -shell threshold energy [from Fig. 4.3(a)]. Defining the ionization potentials for the $2s$ and $2p$ orbitals in the analogous way as we did for our K -shell threshold, we can obtain IPD values for these orbitals as well. These values are shown in Fig. 4.5(a). The XCRYSTAL result was interpolated onto integer values of the charge state Q . Despite the ability of XCRYSTAL to calculate orbital-specific IPD values, Fig. 4.5(a) illustrates that the differences between the IPDs of different orbitals are minimal, in agreement with the observation of Son *et al.* [121]. Figure 4.5(b) shows the IPD values for the $2p$ orbital calculated with XCRYSTAL, comparing them with the two-step-HFS result [121], and the results from the modified-EK and the SP models, taken from Ref. [61]. We can see that XCRYSTAL reflects a similar trend as the two-step-HFS model, but lies closer to the IPD values determined from the modified-EK model as Q is increased.

4.3.2 Band structure at WDM temperatures

We proceed with calculations of the temperature-dependent band structure for Al at WDM conditions. We start with the discussion of Al at $T = 0$ eV. In Fig. 4.6 we present the first 10 energy bands of a nonzero bandwidth at T

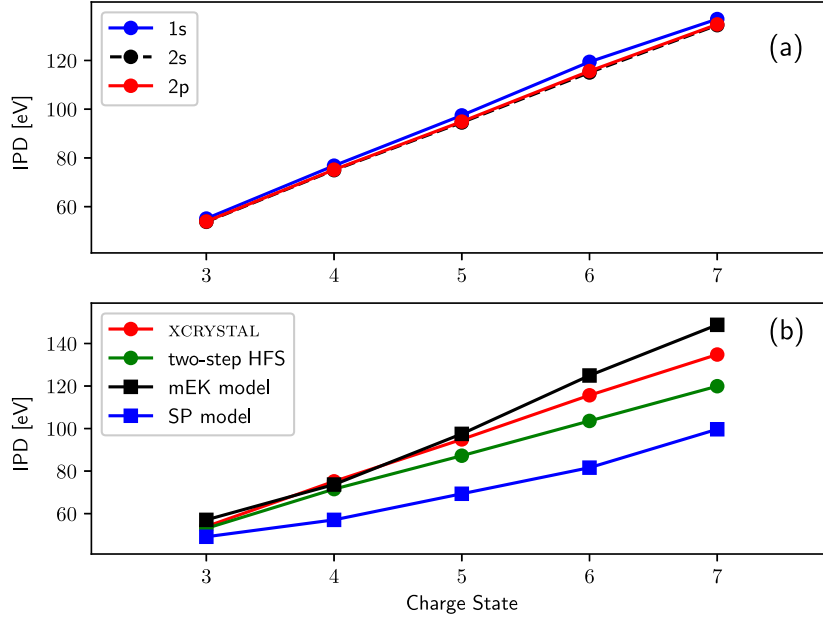


Figure 4.5: Ionization potential depression calculated for x-ray-excited solid Al as a function of charge state. (a) Result from XCRYSTAL obtained for all core orbitals of aluminum. (b) Comparison between the XCRYSTAL result for the 2p orbital, the two-step HFS model result [121], the result from the modified-EK model, and the result from the SP model, taken from Ref. [61]. The result from XCRYSTAL has been interpolated onto integer values of Q .

$= 0$ eV, along the path Γ -X-W-L- Γ -K-X in the BZ. This path was chosen for the comparison of our predictions with Refs. [159, 160]. The energy axis on the left is given in Rydbergs (Ry) and was shifted by $+1.54$ Ry ($+20.98$ eV), in order to adjust the energy at the Γ point to the energy of the lowest delocalized state, $E_{\min, \text{deloc}}$. An unshifted energy axis (in eV) is presented on the right. As was previously mentioned in Sec. 4.3, our choice of a cubic unit cell implies that \mathbf{k} -dependent quantities, such as the energies $E_{n, \mathbf{k}}$ shown in Fig. 4.6, that lie in the first BZ of FCC, but outside of our cubic BZ, are shifted to a higher band, n . Therefore, the result from any XCRYSTAL calculation shows many more bands as compared to conventional methods. This is simply a consequence of having chosen a cubic unit cell. Both the blue lines and the red lines presented in Fig. 4.6 are the result from the same XCRYSTAL calculation. The blue lines show the result as calculated using XCRYSTAL, whereas the red line traces out the bands which would be obtained for the conventional primitive unit cell. One can see excellent

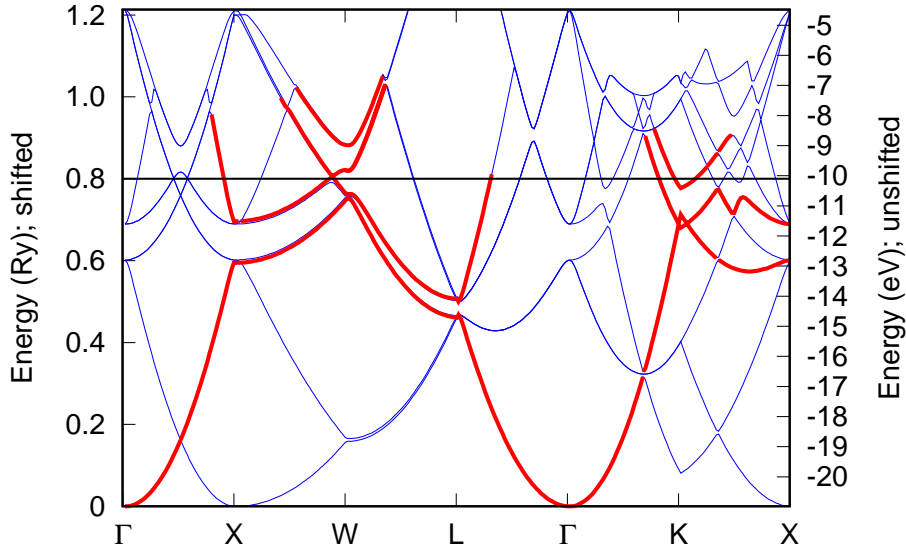


Figure 4.6: Band structure of aluminum at $T = 0$ eV along the path Γ -X-W-L- Γ -K-X calculated using XCRYSTAL. The blue line represents the XCRYSTAL result, and the red line traces out the lines that would be obtained when using the conventional primitive FCC unit cell, to help guide the eye for comparison with Refs. [159, 160]. The horizontal black line indicates the Fermi energy. The energy axis on the left is given in Rydbergs (Ry) and was shifted by +1.54 Ry (+20.98 eV), so that the energy at the Γ point starts at the origin. An unshifted energy axis given in eV is presented on the right.

agreement with the well-known results of Refs. [159, 160]. The solid black line denotes our value for the Fermi energy ε_F , calculated as the chemical potential μ at $T = 0$ eV, with a predicted value of -10.12 eV. Keeping the shift of $E_{\text{min,deloc}}$ ($= -20.98$ eV) in mind, the Fermi energy is calculated relative to the bottom of the conduction band, as $\varepsilon_F = \mu - E_{\text{min,deloc}}$. It is found to be $0.8 \text{ Ry} = 10.86 \text{ eV}$, whereas the experimental value is 11.7 eV [77]. The value for the constant potential V_0 at $T = 0$ eV is -18.34 eV , which is above the energy value of the lowest-lying delocalized energy band at $E_{\text{min,deloc}}$. This indicates that the bands in Fig. 4.6 with an (unshifted) energy below $V_0 = -18.34 \text{ eV}$ correspond to electronic states in which the electron is quasi-bound and tunnels between atomic sites. They are not localized enough to be considered part of the core orbitals [cf. Eq. (4.17)]. Between each symmetry point (Γ , X, W, etc.) in Fig. 4.6, there are 50 \mathbf{k} points shown, which is the value we shall retain for the remaining band structure plots. We do not perform an entire XCRYSTAL run with such a fine \mathbf{k} grid, instead taking the converged electronic density from the run with the parameters

mentioned previously (Sec. 4.2.7), and performing a single XCRYSTAL matrix diagonalization in the hybrid basis.

In Fig. 4.7, we show the first 30 energy bands with a nonzero bandwidth at temperatures of $T = 25, 50, 75$, and 100 eV. For these plots, we traced out the path Γ -X-W-L- Γ -K-W-U-X to cover all lines of high symmetry in the BZ. In addition to the interesting observation that at $T = 75$ eV there

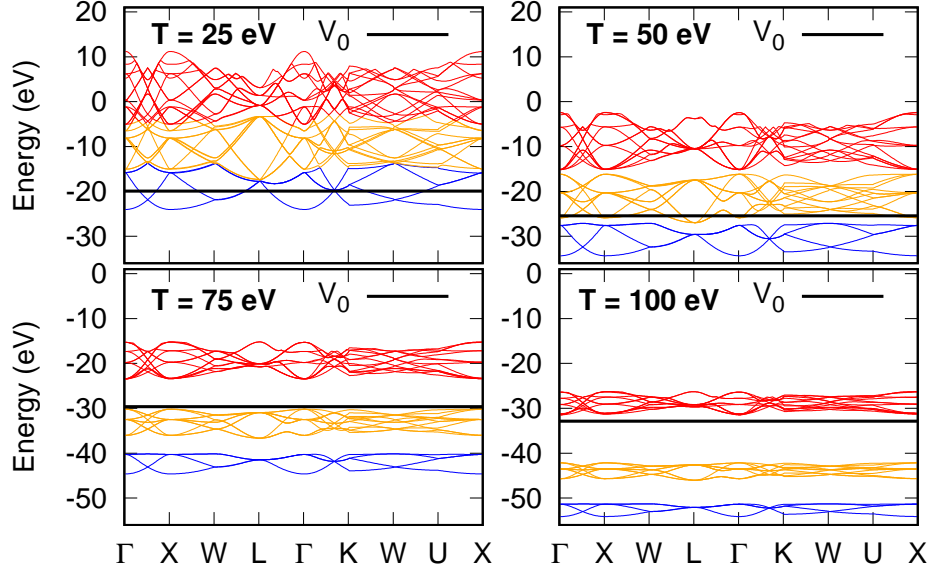


Figure 4.7: Band structure of the first 30 delocalized energy bands of aluminum at temperatures $T = 25, 50, 75$, and 100 eV, along the path Γ -X-W-L- Γ -K-W-U-X, calculated with XCRYSTAL. The black line denotes the constant potential V_0 . The colors are there to aid in grouping together those bands that separate from the rest for higher temperatures. The energies on the y axis are given in eV.

appear to be no orbital states present directly above V_0 , we can perceive three general features in Fig. 4.7 as the electronic temperature rises: (1) all energy bands are lowered, (2) two band gaps start to form and progressively separate, and (3) the bandwidths become smaller. The conclusion is that with the increasing temperature, we observe a formation of quasi-atomic $3s$ and $3p$ lines, that was also reported in Ref. [131].

The physical mechanism behind this observation is the following: As the temperature rises, thermal excitations start to generate partial vacancies within the bound $1s$, $2s$, and $2p$ orbitals. This causes the nucleus to experience less screening, which in turn makes its potential $V(r)$ more attractive, thereby dragging down all energies. In addition, it is apparent that with increasing electronic temperatures, the bands start to lose their width and their delocalized character, thereby exhibiting features of a more atomic

nature.

4.4 Conclusion and outlook

In this work, we have developed an *ab initio* method for calculating quantum states of hot thermalized electrons confined to a cold ionic crystal lattice. It has been implemented into a new toolkit, XCRYSTAL. Using a mean-field HFS approach in combination with the Bloch formalism, we constructed a hybrid basis consisting of both plane waves and localized atomic orbitals, with respect to which we represented the electronic states in this type of transient WDM system. Allowing for an interwoven optimization between core and valence electrons, we accurately reproduced the experimental data obtained from the LCLS experiment [34, 61] on Al plasmas in WDM conditions, in a highly efficient manner. Additionally, our model allowed for the calculation of band structures at various temperatures, $T \sim 0\text{--}100$ eV. We concluded that the incorporation of the full crystal structure had only a minor effect on the results calculated for comparison with Refs. [34, 61] and argued that the role of optimized core orbitals is vital in describing these types of systems. In addition, the band structure of Al was shown to be in good agreement with previous work at zero temperature [159, 160]. The computationally efficient scheme in XCRYSTAL facilitated the calculation of the band structure to temperatures and densities typical for WDM conditions.

The new tool XCRYSTAL provides not only the calculation of bands and energy levels but gives full access to the electronic wave functions in a thermalized electron plasma at a certain temperature. This will enable us in the future to model atomic processes in a dense plasma environment, which is critical for a proper description of WDM formation. Until now, the respective cross sections and rates were adapted from isolated-atom models (see, e.g., Ref. [1]). In particular, XCRYSTAL enables access to the evaluation of the electron-impact-ionization cross section in solid-density plasmas, also measured experimentally [87]. It is the ultimate goal of XCRYSTAL to provide fast and accurate data of WDM properties for electronic Monte Carlo simulations of WDM, so as to contribute to the description of matter exposed to high-intensity x-ray pulses, in a similar manner the codes XATOM [43, 79], XMDYN [79, 80], and XMOLECULE [162, 163] do. The inclusion of molecular dynamics is conceptually possible as was mentioned in Sec 4.2.2. For application of this work in an astrophysical context, it is conceivable that the inclusion of the effects of an external magnetic field will be necessary [164]. It would be possible to perturbatively treat the effect of an external magnetic field through an interaction Hamiltonian in XCRYSTAL. For magnetic fields that are nonperturbatively strong, their inclusion would break some of the symmetries being exploited in XCRYSTAL. We believe that the present

work will pave the way for a more accurate theoretical description of non-isothermal WDM, and will significantly advance the understanding of this extreme state of matter.

4.A Normalization of core Bloch waves

In this appendix, we will derive the normalization of the core Bloch wave functions $\psi_{n_C, \mathbf{k}}(\mathbf{r})$ as defined in Eq. (4.6), from the normalization of the total electronic wave function $\varphi_{n, \mathbf{k}}(\mathbf{r})$. The wave functions $\varphi_{n, \mathbf{k}}(\mathbf{r})$ are Bloch functions [see Eq. (4.1)]. These wave functions are orthonormal within the entire crystal volume, $\langle \varphi_{n, \mathbf{k}} | \varphi_{n', \mathbf{k}'} \rangle = \delta_{nn'} \delta_{\mathbf{k}, \mathbf{k}'}$. Therefore, we have

$$\begin{aligned}
 \langle \varphi_{n, \mathbf{k}} | \varphi_{n', \mathbf{k}'} \rangle &= \int_V d^3r \varphi_{n, \mathbf{k}}^*(\mathbf{r}) \varphi_{n', \mathbf{k}'}(\mathbf{r}) \\
 &= \frac{1}{V} \int_V d^3r e^{-i\mathbf{k} \cdot \mathbf{r}} \mu_{n, \mathbf{k}}^*(\mathbf{r}) e^{i\mathbf{k}' \cdot \mathbf{r}} \mu_{n', \mathbf{k}'}(\mathbf{r}) \\
 &= \frac{1}{V} \sum_{\mathbf{R}} \int_{\Omega} d^3r e^{-i\mathbf{k} \cdot (\mathbf{r} + \mathbf{R})} \mu_{n, \mathbf{k}}^*(\mathbf{r} + \mathbf{R}) e^{i\mathbf{k}' \cdot (\mathbf{r} + \mathbf{R})} \mu_{n', \mathbf{k}'}(\mathbf{r} + \mathbf{R}) \\
 &= \frac{1}{V} \sum_{\mathbf{R}} e^{-i(\mathbf{k} - \mathbf{k}') \cdot \mathbf{R}} \int_{\Omega} d^3r e^{-i(\mathbf{k} - \mathbf{k}') \cdot \mathbf{r}} \mu_{n, \mathbf{k}}^*(\mathbf{r}) \mu_{n', \mathbf{k}'}(\mathbf{r}) \\
 &= \frac{N_{\text{cell}}}{V} \delta_{\mathbf{k}, \mathbf{k}'} \int_{\Omega} d^3r e^{-i(\mathbf{k} - \mathbf{k}') \cdot \mathbf{r}} \mu_{n, \mathbf{k}}^*(\mathbf{r}) \mu_{n', \mathbf{k}'}(\mathbf{r}) \\
 &= \frac{1}{\Omega} \delta_{\mathbf{k}, \mathbf{k}'} \int_{\Omega} d^3r e^{-i(\mathbf{k} - \mathbf{k}') \cdot \mathbf{r}} \mu_{n, \mathbf{k}}^*(\mathbf{r}) \mu_{n', \mathbf{k}'}(\mathbf{r}) \\
 &= \delta_{nn'} \delta_{\mathbf{k}, \mathbf{k}'}, \tag{4.23}
 \end{aligned}$$

where \mathbf{R} denotes a lattice translation vector. We used $(1/N_{\text{cell}}) \sum_{\mathbf{R}} e^{-i(\mathbf{k} - \mathbf{k}') \cdot \mathbf{R}} = \delta_{\mathbf{k}, \mathbf{k}'}$ and $V = N_{\text{cell}} \Omega$. This implies that we normalize the $\mu_{n, \mathbf{k}}(\mathbf{r})$ within the unit cell volume Ω as

$$\int_{\Omega} d^3r \mu_{n, \mathbf{k}}^*(\mathbf{r}) \mu_{n, \mathbf{k}}(\mathbf{r}) = \Omega. \tag{4.24}$$

For core electrons, we know a priori that our atomic orbital wave functions obey $\langle \phi_{n_C} | \phi_{n'_C} \rangle = \delta_{n_C n'_C}$. However, for consistency, we should also normalize $\mu_{n_C, \mathbf{k}}(\mathbf{r})$ to Ω , with respect to a unit cell volume Ω , just as was the case for $\mu_{n, \mathbf{k}}(\mathbf{r})$. This is why the factor N in Eq. (4.6) was split

up as $N = N_a N_b$. Imposing the preferred normalization, we find

$$\begin{aligned}
 \Omega &= \int_{\Omega} d^3r \mu_{n_C, \mathbf{k}}^*(\mathbf{r}) \mu_{n_C, \mathbf{k}}(\mathbf{r}) = N_b^2 \int_{\Omega} d^3r e^{i\mathbf{k} \cdot (\mathbf{r} - \mathbf{r}_{n_C})} e^{-i\mathbf{k} \cdot (\mathbf{r} - \mathbf{r}_{n_C})} \\
 &\quad \times \phi_{n_C}^*(\mathbf{r} - \mathbf{r}_{n_C}) \phi_{n_C}(\mathbf{r} - \mathbf{r}_{n_C}) \\
 &= N_b^2 \int_{\Omega} d^3r \phi_{n_C}^*(\mathbf{r} - \mathbf{r}_{n_C}) \phi_{n_C}(\mathbf{r} - \mathbf{r}_{n_C}) \\
 &= N_b^2, \tag{4.25}
 \end{aligned}$$

revealing that $N_b = \sqrt{\Omega}$. Furthermore, the $\mu_{n_C, \mathbf{k}}(\mathbf{r})$ are orthogonal to each other, but only for $\mathbf{k} = \mathbf{k}'$:

$$\begin{aligned}
 \int_{\Omega} d^3r \mu_{n_C, \mathbf{k}}^*(\mathbf{r}) \mu_{n'_C, \mathbf{k}'}(\mathbf{r}) &= \Omega \int_{\Omega} d^3r e^{i\mathbf{k} \cdot (\mathbf{r} - \mathbf{r}_{n_C})} e^{-i\mathbf{k}' \cdot (\mathbf{r} - \mathbf{r}_{n'_C})} \\
 &\quad \times \phi_{n_C}^*(\mathbf{r} - \mathbf{r}_{n_C}) \phi_{n'_C}(\mathbf{r} - \mathbf{r}_{n'_C}) \\
 &= \Omega e^{i(\mathbf{k} - \mathbf{k}') \cdot \mathbf{r}_{n_C}} \int_{\Omega} d^3r e^{i(\mathbf{k} - \mathbf{k}') \cdot \mathbf{r}} \\
 &\quad \times \phi_{n_C}^*(\mathbf{r} - \mathbf{r}_{n_C}) \phi_{n'_C}(\mathbf{r} - \mathbf{r}_{n'_C}), \tag{4.26}
 \end{aligned}$$

which is equal to $\Omega \delta_{n_C, n'_C}$ only if $\mathbf{k} = \mathbf{k}'$. In the second line, we used the fact that the n_C label on \mathbf{r}_{n_C} depends only on which atom we are considering, and unless we are considering the same atom, the integrand will be zero for all values of \mathbf{r} within the unit cell because we are assuming nonoverlapping spheres.

Let us now derive N_a for a proper normalization of $\psi_{n_C, \mathbf{k}}(\mathbf{r})$:

$$\psi_{n_C, \mathbf{k}}(\mathbf{r}) = N_a e^{i\mathbf{k} \cdot \mathbf{r}} \mu_{n_C, \mathbf{k}}(\mathbf{r}) \quad \text{and} \quad \langle \psi_{n_C, \mathbf{k}} | \psi_{n'_C, \mathbf{k}'} \rangle = \delta_{n_C n'_C} \delta_{\mathbf{k}, \mathbf{k}'}, \tag{4.27}$$

which yields

$$\begin{aligned}
 \langle \psi_{n_C, \mathbf{k}} | \psi_{n'_C, \mathbf{k}'} \rangle &= \int_V d^3r \psi_{n_C, \mathbf{k}}^*(\mathbf{r}) \psi_{n'_C, \mathbf{k}'}(\mathbf{r}) \\
 &= N_a^2 \int_V d^3r e^{-i\mathbf{k} \cdot \mathbf{r}} \mu_{n_C, \mathbf{k}}^*(\mathbf{r}) e^{i\mathbf{k}' \cdot \mathbf{r}} \mu_{n'_C, \mathbf{k}'}(\mathbf{r}) \\
 &= N_a^2 \sum_{\mathbf{R}} \int_{\Omega} d^3r e^{-i\mathbf{k} \cdot (\mathbf{r} + \mathbf{R})} \mu_{n_C, \mathbf{k}}^*(\mathbf{r} + \mathbf{R}) e^{i\mathbf{k}' \cdot (\mathbf{r} + \mathbf{R})} \mu_{n'_C, \mathbf{k}'}(\mathbf{r} + \mathbf{R}) \\
 &= N_a^2 \sum_{\mathbf{R}} e^{-i(\mathbf{k} - \mathbf{k}') \cdot \mathbf{R}} \int_{\Omega} d^3r e^{-i(\mathbf{k} - \mathbf{k}') \cdot \mathbf{r}} \mu_{n_C, \mathbf{k}}^*(\mathbf{r}) \mu_{n'_C, \mathbf{k}'}(\mathbf{r}) \\
 &= N_{\text{cell}} N_a^2 \delta_{\mathbf{k}, \mathbf{k}'} \int_{\Omega} d^3r e^{-i(\mathbf{k} - \mathbf{k}') \cdot \mathbf{r}} \mu_{n_C, \mathbf{k}}^*(\mathbf{r}) \mu_{n'_C, \mathbf{k}'}(\mathbf{r}) \\
 &= N_{\text{cell}} N_a^2 \Omega \delta_{n_C n'_C} \delta_{\mathbf{k}, \mathbf{k}'}, \tag{4.28}
 \end{aligned}$$

showing that $N_a = 1/\sqrt{V}$. To summarize, the total wave function has the Bloch-wave form:

$$\varphi_{n, \mathbf{k}}(\mathbf{r}) = \frac{1}{\sqrt{V}} e^{i\mathbf{k} \cdot \mathbf{r}} \mu_{n, \mathbf{k}}(\mathbf{r}), \quad \text{satisfying} \quad \langle \varphi_{n, \mathbf{k}} | \varphi_{n', \mathbf{k}'} \rangle = \delta_{nn'} \delta_{\mathbf{k}, \mathbf{k}'}, \tag{4.29}$$

and we use the following ansatz with a hybrid basis:

$$\varphi_{n,\mathbf{k}}(\mathbf{r}) = \frac{1}{\sqrt{V}} \sum_i v_{n,\mathbf{k}}(\mathbf{K}_i) e^{i(\mathbf{k}+\mathbf{K}_i)\cdot\mathbf{r}} + \sum_{n_C} w_{n,\mathbf{k}}(n_C) \psi_{n_C,\mathbf{k}}(\mathbf{r}). \quad (4.30)$$

Here the core wave functions $\psi_{n_C,\mathbf{k}}(\mathbf{r})$ are given by

$$\psi_{n_C,\mathbf{k}}(\mathbf{r}) = \frac{1}{\sqrt{V}} e^{i\mathbf{k}\cdot\mathbf{r}} \mu_{n_C,\mathbf{k}}(\mathbf{r}), \quad \text{satisfying} \quad \langle \psi_{n_C,\mathbf{k}} | \psi_{n'_C,\mathbf{k}'} \rangle = \delta_{n_C n'_C} \delta_{\mathbf{k},\mathbf{k}'}, \quad (4.31)$$

which are also represented as a Bloch wave, with the periodic function

$$\mu_{n_C,\mathbf{k}}(\mathbf{r}) = \sqrt{\Omega} \sum_I e^{-i\mathbf{k}\cdot(\mathbf{r}-\mathbf{R}_{I,n_C})} \phi_{n_C}(\mathbf{r} - \mathbf{R}_{I,n_C}). \quad (4.32)$$

Note that $\mu_{n,\mathbf{k}}$ and $\mu_{n_C,\mathbf{k}}$ are normalized to Ω with respect to the unit cell Ω .

4.B Accelerating SCF convergence

In this appendix, we will elaborate on a new scheme for improving SCF convergence, which proved very successful for our computational framework.

The convergence of the SCF method is generally rather slow. Therefore, much effort has been invested into methods improving it [160]. A simple example of such a method is *linear mixing*, described in Ref. [160]. In an attempt to steer the convergence, one uses the information from the previous iterations, i.e., instead of using the potential $V_i(r)$ in the i th SCF iteration, one uses $V_i^M(r) = \alpha V_i(r) + (1 - \alpha) V_{i-1}^M(r)$ with a free parameter $\alpha \in [0, 1]$. We distinguish here between the potential $V_i(r)$ obtained from the electronic density using Eq. (4.19), and the "mixed" potential $V_i^M(r)$ obtained from performing the linear mixing. A different quantity, such as the electron density ρ , may also be used in the mixing [160]. Building on this notion of steering convergence, we have developed a method that adjusts the α parameter per iteration, using the information from all previous iterations. In this way, we are working with $\alpha \rightarrow \alpha_i$.

Using the information from previous iterations, we impose for the i th SCF iteration that

$$V_i^M(r) = \sum_{m=1}^i w_m V_m(r), \quad (4.33)$$

with weights $\{w_m\}$, which are normalized to 1, i.e., $\sum_{m=1}^i w_m = 1$. It is intuitively understandable that we expect the weight w_i associated with the i th iteration to be larger if the error associated with that iteration is

smaller. With that in mind, we define $c_i = \|\mathbf{e}_i\|^{-1}$, for some suitably defined error vector \mathbf{e}_i . It is related to w_i through the normalization condition $\sum_{m=1}^i w_m = 1$:

$$w_i = \frac{c_i}{\sum_{m=1}^i c_m} \equiv c_i k_i. \quad (4.34)$$

Note that as more SCF iterations are being considered, a specific c_m will remain unchanged, whereas k_m , and therefore w_m , will be updated for every iteration. We can easily combine this into the following adaptive linear mixing scheme:

$$\begin{aligned} V_i^M(r) &= \sum_{m=1}^i w_m V_m(r) = k_i \sum_{m=1}^i c_m V_m(r) \\ &= k_i c_i V_i(r) + k_i \sum_{m=1}^{i-1} c_m V_m(r) \\ &= k_i c_i V_i(r) + \frac{k_i}{k_{i-1}} V_{i-1}^M(r). \end{aligned} \quad (4.35)$$

From this, we can identify $\alpha_i = k_i c_i = w_i$. We can also easily show that $k_i/k_{i-1} = 1 - \alpha_i$, by using $(k_{i-1})^{-1} + c_i = (k_i)^{-1}$. Multiplying both sides of this equation by k_i , we get $\alpha_i + (1 - \alpha_i) = 1$, as expected. In the implementation of XCRYSTAL, we defined the error vector to be $\mathbf{e}_i = |V_i(r) - V_{i-1}(r)|/V_{i-1}(r)$. For the first iteration, no mixing is done as the error vector cannot be defined yet. To demonstrate how the new adaptive linear mixing scheme works for our particular framework, we compare the performance of the adaptive linear mixing to static linear mixing, with two different mixing parameters α , in Fig. 4.8. It illustrates not only that the adaptive linear mixing is useful for speeding up the convergence, but that its application is necessary for high-temperature cases to achieve convergence. The static linear mixing shown in Fig. 4.8 exhibits an exponential behavior with increasing temperatures and eventually fails to converge within a convergence criterion of 10^{-6} % for $T > 35$ eV ($\alpha = 0.6$) and $T > 15$ eV ($\alpha = 1.0$). We used a relative difference of the total, Fermi-Dirac-weighted energy of the system $\sum_{n,\mathbf{k}} E_{n,\mathbf{k}} \bar{n}_{n,\mathbf{k}}$ between iterations as the SCF-convergence parameter, achieving convergence if this relative difference was smaller than 10^{-6} %.

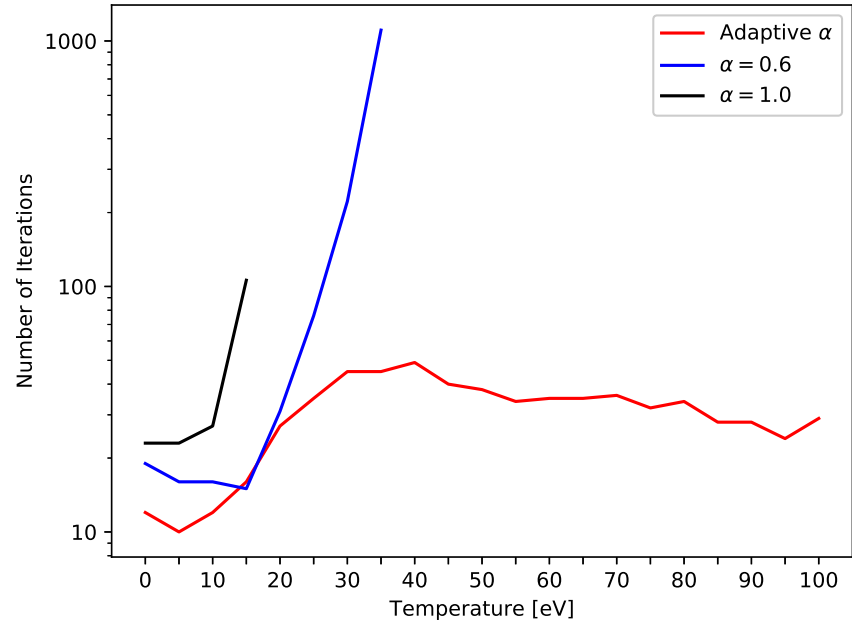


Figure 4.8: The number of SCF iterations necessary to reach convergence (with a convergence criterion of 10^{-6} %) using static linear mixing with $\alpha = 1$ and $\alpha = 0.6$ as well as our adaptive linear mixing for Al plasma calculations at various electronic temperatures. For this plot, $|\mathbf{K}|_{\max} = 4.0 \text{ } a_0^{-1}$ ($N_{\mathbf{K}} = 461$) is used.

Chapter 5

Electron-impact-ionization cross section for nonisothermal warm dense matter

In Chapter 3, we investigated the effect of the electronic configuration of an ion on the electron-impact-ionization cross section. In Chapter 4, we developed a computationally efficient way of computing the electronic states for a transient nonisothermal state of warm dense matter. In this Chapter, we combine these two topics by deriving the theoretical framework needed to calculate the electron-impact-ionization cross section within transient nonisothermal warm dense matter.

5.1 Theoretical derivation

To calculate the electron-impact-ionization cross section within WDM, we follow the derivation of the DDCS up to Eq. (2.120), or equivalently up to Eq. (3.7). However, instead of filling in the representation of the spin orbitals with respect to spherical harmonics, as was done in Eq. (2.82), or equivalently in Eq. (3.3), we fill in the XCRYSTAL ansatz for the spin orbitals [Eq. (4.5)]. Specifically filling in

$$\varphi_{n,\mathbf{k}}(\mathbf{r}) = \frac{1}{\sqrt{V}} \sum_m v_{n,\mathbf{k}}(\mathbf{K}_m) e^{i(\mathbf{k}+\mathbf{K}_m)\cdot\mathbf{r}} + \sum_{n_C} w_{n,\mathbf{k}}(n_C) \psi_{n_C,\mathbf{k}}(\mathbf{r}), \quad (5.1)$$

as φ_I and φ_F into

$$\begin{aligned} \frac{d^2\sigma}{d\Omega dE_{\text{out}}} &= \frac{4}{Q^4} \frac{q_{\text{out}}}{q_{\text{in}}} \sum_{I,F} \bar{n}_I(1 - \bar{n}_F) \left| \langle \varphi_F | e^{i\mathbf{Q}\cdot\mathbf{x}} | \varphi_I \rangle \right|^2 \delta(\varepsilon_F - \varepsilon_I - \omega) \\ &= \frac{4}{Q^4} \frac{q_{\text{out}}}{q_{\text{in}}} S(\mathbf{Q}, \omega), \end{aligned} \quad (5.2)$$

where the *structure factor* $S(\mathbf{Q}, \omega)$ was factored out:

$$S(\mathbf{Q}, \omega) = \sum_{I,F} \bar{n}_I(1 - \bar{n}_F) \left| \langle \varphi_F | e^{i\mathbf{Q}\cdot\mathbf{x}} | \varphi_I \rangle \right|^2 \delta(\varepsilon_F - \varepsilon_I - \omega). \quad (5.3)$$

This term is useful to factor out, because it is not specific to Coulomb scattering. It encapsulates the response of a many-electron system (described using spin orbitals) to an interaction Hamiltonian proportional to the electron density $\hat{n}(\mathbf{x})$, or, more accurately, the Fourier transform thereof.

Note that this implies that we are still treating the incoming and outgoing electron as a plane wave, as was done in Chapter 3. However, directly filling in Eq. (5.1) into Eq. (5.3) would result in taking the square of a three-dimensional integral of four terms. It is much easier to express $\varphi_{n,\mathbf{k}}(\mathbf{r})$ in terms of plane waves alone, but in a way to not exclude the updated core orbitals. We may achieve this as follows:

$$\begin{aligned} \varphi_{n,\mathbf{k}}(\mathbf{r}) &= \frac{1}{\sqrt{V}} \sum_i v_{n,\mathbf{k}}(\mathbf{K}_i) e^{i(\mathbf{k}+\mathbf{K}_i)\cdot\mathbf{r}} + \sum_{n_C} w_{n,\mathbf{k}}(n_C) \psi_{n_C,\mathbf{k}} \\ &= \frac{1}{\sqrt{V}} \sum_i \left(v_{n,\mathbf{k}}(\mathbf{K}_i) + \sum_{n_C} w_{n,\mathbf{k}}(n_C) v_{n_C,\mathbf{k}}^{\text{core}}(\mathbf{K}_i) \right) e^{i(\mathbf{k}+\mathbf{K}_i)\cdot\mathbf{r}} \\ &\equiv \frac{1}{\sqrt{V}} \sum_i \bar{v}_{n,\mathbf{k}}(\mathbf{K}_i) e^{i(\mathbf{k}+\mathbf{K}_i)\cdot\mathbf{r}}, \end{aligned} \quad (5.4)$$

where Eq. (4.31) was used to expand $\psi_{n_C,\mathbf{k}}$ as a Bloch wave, which was subsequently Fourier decomposed, i.e.,

$$\psi_{n_C,\mathbf{k}}(\mathbf{r}) = \frac{1}{\sqrt{V}} e^{i\mathbf{k}\cdot\mathbf{r}} \mu_{n_C,\mathbf{k}}(\mathbf{r}) = \frac{1}{\sqrt{V}} \sum_i v_{n_C,\mathbf{k}}^{\text{core}}(\mathbf{K}_i) e^{i(\mathbf{k}+\mathbf{K}_i)\cdot\mathbf{r}}. \quad (5.5)$$

In order to work in terms of the pure plane-wave coefficient $\bar{v}_{n,\mathbf{k}}(\mathbf{K}_i)$, we must find $v_{n_C,\mathbf{k}}^{\text{core}}(\mathbf{K}_i)$. We emphasize that, in spite of the fact that Eq (5.4) seems to suggest we are working in a pure plane-wave basis, as was done in Sec. 4.2.1, the information regarding the core orbitals and the hybrid basis is not lost. It has simply been absorbed into the new Fourier coefficient, $\bar{v}_{n,\mathbf{k}}(\mathbf{K}_i)$, with respect to plane waves. Therefore, the cutoff $N_{\mathbf{K}}$ involved in the sum over reciprocal lattice vectors in Eq (5.4) will be the same as the from the original ansatz [Eq. (5.1)], used in Chapter 4. In order to

find $v_{n_C, \mathbf{k}}^{\text{core}}(\mathbf{K}_i)$, we can simply equate the Fourier decomposition of $\mu_{n_C, \mathbf{k}}(\mathbf{r})$ with the expression we found for it in terms of the core orbitals [Eq. (4.32)]. Being restricted to a single unit cell, this yields:

$$\sum_j v_{n_C, \mathbf{k}}^{\text{core}}(\mathbf{K}_j) e^{i\mathbf{K}_j \cdot \mathbf{r}} = \sqrt{\Omega} e^{-i\mathbf{k} \cdot (\mathbf{r} - \mathbf{r}_a)} \phi_{n_C}(\mathbf{r} - \mathbf{r}_a). \quad (5.6)$$

Taking an inverse Fourier transformation reveals that $v_{n_C, \mathbf{k}}^{\text{core}}(\mathbf{K}_j) = \langle \mathbf{k} + \mathbf{K}_j | \psi_{n_C, \mathbf{k}} \rangle$, such that

$$\bar{v}_{n, \mathbf{k}}(\mathbf{K}_i) = v_{n, \mathbf{k}}(\mathbf{K}_i) + \sum_{n_C} w_{n, \mathbf{k}}(n_C) \langle \mathbf{k} + \mathbf{K}_i | \psi_{n_C, \mathbf{k}} \rangle, \quad (5.7)$$

which shows that $\bar{v}_{n, \mathbf{k}}(\mathbf{K}_i)$ can be calculated using quantities readily at our disposal after an XCRYSTAL run.

We proceed by utilizing the ansatz for $\varphi_{n, \mathbf{k}}(\mathbf{r})$ [Eq. (5.4)] in order to calculate the structure factor $S(\mathbf{Q}, \omega)$ [Eq. (5.3)]. The subscripts I and F are now turned into $\{n_i, \mathbf{k}_i, s_i\}$ and $\{n_f, \mathbf{k}_f, s_f\}$, respectively. The matrix element can be expressed simply as:

$$\begin{aligned} \langle \varphi_F | e^{i\mathbf{Q} \cdot \mathbf{x}} | \varphi_I \rangle &= \int_V d^3r \varphi_F^\dagger(\mathbf{r}) e^{i\mathbf{Q} \cdot \mathbf{r}} \varphi_I(\mathbf{r}) \\ &= \frac{\delta_{s_i, s_f}}{V} \sum_{a, b} \bar{v}_{n_f, \mathbf{k}_f}^*(\mathbf{K}_b) \bar{v}_{n_i, \mathbf{k}_i}(\mathbf{K}_a) \\ &\quad \times \int_V d^3r e^{i(\mathbf{k}_i + \mathbf{K}_a + \mathbf{Q} - \mathbf{k}_f - \mathbf{K}_b) \cdot \mathbf{r}}. \end{aligned} \quad (5.8)$$

This turns $S(\mathbf{Q}, \omega)$ into:

$$\begin{aligned} S(\mathbf{Q}, \omega) &= \sum_{n_i, n_f} \sum_{\mathbf{k}_i, \mathbf{k}_f} \sum_{s_i, s_f} \bar{n}_{n_i, \mathbf{k}_i} (1 - \bar{n}_{n_f, \mathbf{k}_f}) \frac{(\delta_{s_i, s_f})^2}{V^2} \\ &\quad \times \delta(E_{n_i, \mathbf{k}_i} - E_{n_f, \mathbf{k}_f} + \omega) \\ &\quad \times \left| \sum_{a, b} \bar{v}_{n_f, \mathbf{k}_f}^*(\mathbf{K}_b) \bar{v}_{n_i, \mathbf{k}_i}(\mathbf{K}_a) \int_V d^3r e^{i(\mathbf{k}_i + \mathbf{K}_a + \mathbf{Q} - \mathbf{k}_f - \mathbf{K}_b) \cdot \mathbf{r}} \right|^2, \end{aligned} \quad (5.9)$$

where $\omega = E_{\text{in}} - E_{\text{out}}$ and $\bar{n}_{n, \mathbf{k}} = 1/(e^{\beta(E_{n, \mathbf{k}} - \mu)} + 1)$. Also denoted are $\mathbf{k}_{if} = \mathbf{k}_i - \mathbf{k}_f$ and $\mathbf{K}_{ab} = \mathbf{K}_a - \mathbf{K}_b$. We can proceed by performing the sums

over s_i and s_f , resulting in an overall factor of 2,

$$\begin{aligned}
S(\mathbf{Q}, \omega) &= \frac{2}{V^2} \sum_{n_i, n_f} \sum_{\mathbf{k}_i, \mathbf{k}_f} \bar{n}_{n_i, \mathbf{k}_i} (1 - \bar{n}_{n_f, \mathbf{k}_f}) \\
&\quad \times \delta(E_{n_i, \mathbf{k}_i} - E_{n_f, \mathbf{k}_f} + \omega) \\
&\quad \times \left| \sum_{a, b} \bar{v}_{n_f, \mathbf{k}_f}^*(\mathbf{K}_b) \bar{v}_{n_i, \mathbf{k}_i}(\mathbf{K}_a) \int_V d^3 r e^{i(\mathbf{k}_{if} + \mathbf{K}_{ab} + \mathbf{Q}) \cdot \mathbf{r}} \right|^2 \\
&= 2 \left(\frac{(2\pi)^3}{V} \right)^2 \sum_{n_i, n_f} \sum_{\mathbf{k}_i, \mathbf{k}_f} \bar{n}_{n_i, \mathbf{k}_i} (1 - \bar{n}_{n_f, \mathbf{k}_f}) \\
&\quad \times \delta(E_{n_i, \mathbf{k}_i} - E_{n_f, \mathbf{k}_f} + \omega) \\
&\quad \times \left| \sum_{a, b} \bar{v}_{n_f, \mathbf{k}_f}^*(\mathbf{K}_b) \bar{v}_{n_i, \mathbf{k}_i}(\mathbf{K}_a) \delta^{(3)}(\mathbf{k}_{if} + \mathbf{K}_{ab} + \mathbf{Q}) \right|^2.
\end{aligned} \tag{5.10}$$

Let us concern ourselves with the last term, which we may expand as follows:

$$\begin{aligned}
&\left| \sum_{a, b} \bar{v}_{n_f, \mathbf{k}_f}^*(\mathbf{K}_b) \bar{v}_{n_i, \mathbf{k}_i}(\mathbf{K}_a) \delta^{(3)}(\mathbf{k}_{if} + \mathbf{K}_{ab} + \mathbf{Q}) \right|^2 \\
&= \sum_{a, b} \sum_{A, B} \bar{v}_{n_i, \mathbf{k}_i}^*(\mathbf{K}_a) \bar{v}_{n_f, \mathbf{k}_f}(\mathbf{K}_b) \bar{v}_{n_f, \mathbf{k}_f}^*(\mathbf{K}_B) \bar{v}_{n_i, \mathbf{k}_i}(\mathbf{K}_A) \\
&\quad \times \delta^{(3)}(\mathbf{k}_{if} + \mathbf{K}_{ab} + \mathbf{Q}) \delta^{(3)}(\mathbf{k}_{if} + \mathbf{K}_{AB} + \mathbf{Q})
\end{aligned} \tag{5.11}$$

The two delta functions imply that each term is zero, unless $\mathbf{K}_{ab} = \mathbf{K}_{AB}$. Therefore, we may rewrite this as:

$$\begin{aligned}
&\delta^{(3)}(\mathbf{k}_{if} + \mathbf{K}_{ab} + \mathbf{Q}) \delta^{(3)}(\mathbf{k}_{if} + \mathbf{K}_{AB} + \mathbf{Q}) \\
&= [\delta^{(3)}(\mathbf{k}_{if} + \mathbf{K}_{ab} + \mathbf{Q})]^2 \delta_{\mathbf{K}_{ab}, \mathbf{K}_{AB}}.
\end{aligned} \tag{5.12}$$

We evaluate the squared delta function using the expression

$$\begin{aligned}
[\delta^{(3)}(\mathbf{Q})]^2 &= \lim_{V \rightarrow \infty} \frac{1}{(2\pi)^3} \int_V d^3 x e^{i\mathbf{Q} \cdot \mathbf{x}} \delta^{(3)}(\mathbf{Q}) \\
&= \lim_{V \rightarrow \infty} \frac{V}{(2\pi)^3} \delta^{(3)}(\mathbf{Q}).
\end{aligned} \tag{5.13}$$

for some vector \mathbf{Q} . This reduces Eq. (5.11) to:

$$\begin{aligned}
&\left| \sum_{a, b} \bar{v}_{n_f, \mathbf{k}_f}^*(\mathbf{K}_b) \bar{v}_{n_i, \mathbf{k}_i}(\mathbf{K}_a) \delta^{(3)}(\mathbf{k}_{if} + \mathbf{K}_{ab} + \mathbf{Q}) \right|^2 \\
&= \frac{V}{(2\pi)^3} \sum_{a, b} \delta^{(3)}(\mathbf{k}_{if} + \mathbf{K}_{ab} + \mathbf{Q}) \bar{v}_{n_i, \mathbf{k}_i}^*(\mathbf{K}_a) \bar{v}_{n_f, \mathbf{k}_f}(\mathbf{K}_b) \\
&\quad \times \sum_{A, B} \bar{v}_{n_f, \mathbf{k}_f}^*(\mathbf{K}_B) \bar{v}_{n_i, \mathbf{k}_i}(\mathbf{K}_A) \delta_{\mathbf{K}_{ab}, \mathbf{K}_{AB}},
\end{aligned} \tag{5.14}$$

which gives a final result of for the DDCS:

$$\frac{d^2\sigma}{d\Omega dE_{\text{out}}} = \frac{4}{Q^4} \frac{q_{\text{out}}}{q_{\text{in}}} S(\mathbf{Q}, \omega), \quad (5.15)$$

where

$$\begin{aligned} S(\mathbf{Q}, \omega) = & 2 \frac{(2\pi)^3}{V} \sum_{n_i, n_f} \sum_{\mathbf{k}_i, \mathbf{k}_f} \bar{n}_{n_i, \mathbf{k}_i} (1 - \bar{n}_{n_f, \mathbf{k}_f}) \delta(E_{n_i, \mathbf{k}_i} - E_{n_f, \mathbf{k}_f} + \omega) \\ & \times \sum_{a, b} \delta^{(3)}(\mathbf{k}_{if} + \mathbf{K}_{ab} + \mathbf{Q}) \bar{v}_{n_i, \mathbf{k}_i}^*(\mathbf{K}_a) \bar{v}_{n_f, \mathbf{k}_f}(\mathbf{K}_b) \\ & \times \sum_{A, B} \bar{v}_{n_f, \mathbf{k}_f}^*(\mathbf{K}_B) \bar{v}_{n_i, \mathbf{k}_i}(\mathbf{K}_A) \delta_{\mathbf{K}_{ab}, \mathbf{K}_{AB}}. \end{aligned} \quad (5.16)$$

Expressing the sums over \mathbf{k} as $\sum_{\mathbf{k}} = (V/(2\pi)^3) \int d^3k$ gives

$$\begin{aligned} S(\mathbf{Q}, \omega) = & 2 \frac{V}{(2\pi)^3} \sum_{n_i, n_f} \int_{BZ} d^3k_i d^3k_f \bar{n}_{n_i, \mathbf{k}_i} (1 - \bar{n}_{n_f, \mathbf{k}_f}) \delta(E_{n_i, \mathbf{k}_i} - E_{n_f, \mathbf{k}_f} + \omega) \\ & \times \sum_{a, b} \delta^{(3)}(\mathbf{k}_{if} + \mathbf{K}_{ab} + \mathbf{Q}) \bar{v}_{n_i, \mathbf{k}_i}^*(\mathbf{K}_a) \bar{v}_{n_f, \mathbf{k}_f}(\mathbf{K}_b) \\ & \times \sum_{A, B} \bar{v}_{n_f, \mathbf{k}_f}^*(\mathbf{K}_B) \bar{v}_{n_i, \mathbf{k}_i}(\mathbf{K}_A) \delta_{\mathbf{K}_{ab}, \mathbf{K}_{AB}}. \end{aligned} \quad (5.17)$$

Note that the fact that the DDCS is proportional to V makes physical sense. After all, it describes how probable it is for an incoming electron to undergo Coulomb scattering with a lattice of a volume V , which we consider in the limit $V \rightarrow \infty$. It makes sense that in this limit, this probability also approaches ∞ . In light of this, it is more physically justified to consider the DDCS per unit volume and omit the factor V in $S(\mathbf{Q}, \omega)$.

5.2 Towards practical implementation

The goal of this section is to provide a detailed analysis on how to practically implement the structure factor $S(\mathbf{Q}, \omega)$ in Eq. (5.17) into the XCRYSTAL code, so as to determine the DDCS, and, by extension, the total cross section for electron-impact ionization in WDM. The starting point for the calculation of the structure factor $S(\mathbf{Q}, \omega)$ in Eq. (5.17) is a converged XCRYSTAL run, that provides us with energies $E_{n, \mathbf{k}}$, occupation numbers $\bar{n}_{n, \mathbf{k}}$, and Fourier coefficients $v_{n, \mathbf{k}}(\mathbf{K})$ and $w_{n, \mathbf{k}}(n_C)$, from which we can construct $\bar{v}_{n, \mathbf{k}}(\mathbf{K})$. All of these quantities will be defined on predetermined, finite grids for \mathbf{k} and \mathbf{K} , and with them, we have everything needed to calculate $S(\mathbf{Q}, \omega)$. Let us begin by considering how the continuum states being ionized into are treated as a pseudocontinuum in XCRYSTAL.

5.2.1 Pseudocontinuum in xcrystal

Before delving into a discussion on the implementation of a pseudocontinuum in XCRYSTAL, let us be reminded of the need for a *pseudocontinuum* by considering its implementation in XATOM.

Recall from Sec. 3.2.2 that, in principle, XATOM does have the ability to treat *true* continuum wave functions, $u_{\varepsilon,l_f}(r)$. Picking an energy value $\varepsilon > 0$ in the continuum, the radial Schrödinger equation [Eq. (2.83)] can be numerically integrated outward from $r = 0$, without imposing any sort of spatial confinement on the corresponding wave function. Conversely, discretized orbitals $u_{n_f,l_f}(r)$ (along with a discretized set of eigenvalues ε_{n_f,l_f}) were obtained through the diagonalization of the Hamiltonian in a sphere. This implied that the radial wave function, $u(r)$, was confined within the space between $r = 0$ and $r = R_{\max}$, i.e., $u(0) = u(R_{\max}) = 0$. As we considered transitions between bound and free orbitals, and both methods are calculated on different kinds of radial grids, we avoided computationally costly interpolations between both grids by describing the continuum states as part of the discretized spectrum. The fact that we confined the wave functions to a sphere of radius R_{\max} led to the discretization of the continuum. Thereby, the continuum states were treated using a discretized pseudocontinuum. In contrast, we never imposed spatial restrictions on the Bloch wave functions of XCRYSTAL. The hybrid basis used in XCRYSTAL is a continuum basis, because of the incorporation of the \mathbf{k} -space plane waves. Therefore, when we diagonalize the Hamiltonian in \mathbf{k} -space, we work with a true continuum, because, in principle, we can pick any point in \mathbf{k} -space and solve for the eigenvalues and eigenfunctions. Practically, however, we cannot perform this diagonalization for *all* \mathbf{k} -points, and thus, a discretization of the grid in \mathbf{k} -space is necessary. This discretization imposes periodic boundary conditions on the wave functions in real space within the volume V and therefore leads to the implementation of a pseudocontinuum in XCRYSTAL. Note that this diagonalization-based method of obtaining eigenvalues and eigenfunctions, for both bound and continuum wave functions, is a key element of the methodology which is shared by both XATOM and XCRYSTAL.

The requirement for a pseudocontinuum arises in XCRYSTAL when we consider the two delta-distribution functions that guarantee energy- and momentum-conservation in Eq. (5.17). In principle, the (\mathbf{Q}, ω) -grid, on which $S(\mathbf{Q}, \omega)$ is defined, forms an infinite and uncountable set. The delta functions will impose the restrictions $\omega = E_{n_f,k_f} - E_{n_i,k_i}$ and $\mathbf{Q} = -\mathbf{k}_{if} - \mathbf{K}_{ab}$. Even after implementing these restrictions, the resulting (\mathbf{Q}, ω) -grid is in principle still infinite and uncountable, because the wave vectors \mathbf{k} also constitute an infinite and uncountable set. In practice, however, this (\mathbf{Q}, ω) -grid will actually be finite, and therefore countable, because the numerically implemented \mathbf{k} -grid is finite, as was mentioned earlier in this section. Therefore, a (\mathbf{Q}, ω) -point that denotes a transition to (or from) a free continuum

state will be handled using a discrete pseudocontinuum. This scenario is very similar to what we encountered in Eq. (3.8), where we also dealt with the implementation of a pseudocontinuum in an energy-conserving delta function in XATOM, which was treated with the histogram method explained in Sec. 3.2.3. Fortunately, we will not have to invoke this method here, on account of the different normalization imposed on the electronic wave functions in XATOM and XCRYSTAL, for the following reason.

Recall from Sec. 3.2.2 that we worked with final-energy states, $u_{\varepsilon,l_f}(r)$, that are part of the continuum, which, for brevity, we will denote here as $|\varepsilon\rangle$. Continuum wave functions are not L^2 normalizable, because, in order to define a continuum, there can be no spatial confinement. Instead, continuum wave functions are delta-orthonormalized, which implies $\langle\varepsilon|\varepsilon'\rangle = \delta(\varepsilon - \varepsilon')$. However, in XATOM we approximated the continuum by means of a pseudocontinuum, using a finite and countable set of final-energy states $u_{n_f,l_f}(r)$. These were calculated by XATOM within a sphere of radius R_{\max} , and normalized therein. Therefore, the continuum states, which are not L^2 -integrable and have instead been delta-function normalized, and the pseudocontinuum states, which are ordinarily L^2 normalized with respect to a sphere, have been normalized in different fashions. The histogram method detailed in Sec. 3.2.3 was invoked to ensure that the numerical integration over the pseudocontinuum was equivalent to the integration over the continuum, keeping the different normalizations in mind. In contrast, the wave functions employed in XCRYSTAL, $\varphi_{n,\mathbf{k}}(\mathbf{r})$ [Eq. (4.5)], are normalized in a total volume V , for which we take the implicit limit $V \rightarrow \infty$. Therefore, despite the fact that we are also discretizing the continuum in XCRYSTAL, which was solely a consequence from having need for a discretized \mathbf{k} -grid so as to practically implement integrations over \mathbf{k} , the normalization of the continuum states and the pseudocontinuum states is one and the same. Therefore, there is no need to invoke the histogram method in XCRYSTAL.

5.2.2 Structure factor on the coarse-grained (\mathbf{Q}, ω) -grid

In principle, it is possible with XCRYSTAL to calculate $S(\mathbf{Q}, \omega)$ directly. The delta-functions in Eq. (5.17) impose that a specific set of reciprocal lattice vectors $\{(\mathbf{K}_a, \mathbf{K}_b, \mathbf{K}_A, \mathbf{K}_B)\}$ and a specific set of quantum numbers $\{(n, \mathbf{k})\}$ will yield nonzero contributions to the structure factor. With the converged electronic density $\rho(r)$ from a run with XCRYSTAL, it is possible to obtain the values of $E_{n,\mathbf{k}}$, $\bar{n}_{n,\mathbf{k}}$, and $\bar{v}_{n,\mathbf{k}}(\mathbf{K})$ for any such sets from a single diagonalization of the Hamiltonian in XCRYSTAL. In fact, a similar scheme was used to obtain the band structure plots in Sec. 4.3.2. However, due to the many summations present in the expression for $S(\mathbf{Q}, \omega)$ [Eq. (5.17)], it will be more computationally efficient to use the predetermined \mathbf{k} - and \mathbf{K} -grids from the XCRYSTAL run. In order to reconcile the use of these predetermined grids with the restrictions that are imposed by the delta functions

in Eq. (5.17), we will eliminate these delta-functions, by working with a coarse-grained, binned (\mathbf{Q}, ω) -grid, as follows.

Let us define the m -th bin as corresponding to some range $(\mathbf{Q}^{(m)} \pm \Delta\mathbf{Q}^{(m)}/2, \omega^{(m)} \pm \Delta\omega^{(m)}/2)$ to which we associate a single value of $S(\mathbf{Q}^{(m)}, \omega^{(m)})$. This coarse-graining allows us to integrate over a single bin, thereby removing the delta functions, and resulting in an overall factor of $\Delta\mathbf{Q}^{(m)}\Delta\omega^{(m)} \equiv \Delta^{(m)}$. The integration over the m -th bin is performed by integrating over those values of (\mathbf{Q}, ω) in the range $(\mathbf{Q}^{(m)} \pm \Delta\mathbf{Q}^{(m)}/2, \omega^{(m)} \pm \Delta\omega^{(m)}/2)$ such that they belong to the m -th bin. If we introduce the notation for the bin integration over the m -th bin as

$$\int_{(m)} d^3Q d\omega = \int_{\mathbf{Q}^{(m)} - \Delta\mathbf{Q}^{(m)}/2}^{\mathbf{Q}^{(m)} + \Delta\mathbf{Q}^{(m)}/2} d^3Q \int_{\omega^{(m)} - \Delta\omega^{(m)}/2}^{\omega^{(m)} + \Delta\omega^{(m)}/2} d\omega, \quad (5.18)$$

then we have:

$$\int_{(m)} d^3Q d\omega S(\mathbf{Q}, \omega) = \Delta^{(m)} S(\mathbf{Q}^{(m)}, \omega^{(m)}). \quad (5.19)$$

Therefore we may assign a bin-averaged value of $S(\mathbf{Q}, \omega)$ for each bin. For the m -th bin, the averaged value, $S(\mathbf{Q}^{(m)}, \omega^{(m)})$ takes on the form

$$\begin{aligned} S(\mathbf{Q}^{(m)}, \omega^{(m)}) &= \frac{2}{(2\pi)^3} \frac{1}{\Delta^{(m)}} \sum_{n_i, n_f} \int_{BZ} d^3k_i d^3k_f \bar{n}_{n_i, \mathbf{k}_i} (1 - \bar{n}_{n_f, \mathbf{k}_f}) \\ &\quad \times \int_{\omega^{(m)} - \Delta\omega^{(m)}/2}^{\omega^{(m)} + \Delta\omega^{(m)}/2} d\omega \delta(E_{n_i, \mathbf{k}_i} - E_{n_f, \mathbf{k}_f} + \omega) \\ &\quad \times \sum_{a, b} \int_{\mathbf{Q}^{(m)} - \Delta\mathbf{Q}^{(m)}/2}^{\mathbf{Q}^{(m)} + \Delta\mathbf{Q}^{(m)}/2} d^3Q \delta^{(3)}(\mathbf{k}_{if} + \mathbf{K}_{ab} + \mathbf{Q}) \\ &\quad \times \bar{v}_{n_i, \mathbf{k}_i}^*(\mathbf{K}_a) \bar{v}_{n_f, \mathbf{k}_f}(\mathbf{K}_b) \\ &\quad \times \sum_{A, B} \bar{v}_{n_f, \mathbf{k}_f}^*(\mathbf{K}_B) \bar{v}_{n_i, \mathbf{k}_i}(\mathbf{K}_A) \delta_{\mathbf{K}_{ab}, \mathbf{K}_{AB}}. \end{aligned} \quad (5.20)$$

The (\mathbf{Q}, ω) -integrations may be performed explicitly, resulting in

$$\begin{aligned} S(\mathbf{Q}^{(m)}, \omega^{(m)}) &= \frac{2}{(2\pi)^3} \frac{1}{\Delta^{(m)}} \sum_{n_i, n_f} \int_{BZ} d^3k_i d^3k_f \bar{n}_{n_i, \mathbf{k}_i} (1 - \bar{n}_{n_f, \mathbf{k}_f}) \\ &\quad \times \text{rect} \left(\frac{E_{n_f, \mathbf{k}_f} - E_{n_i, \mathbf{k}_i} - \omega^{(m)}}{\Delta\omega^{(m)}} \right) \\ &\quad \times \sum_{a, b} \text{rect}^{(3)} \left(\frac{-\mathbf{k}_{if} - \mathbf{K}_{ab} - \mathbf{Q}^{(m)}}{\Delta\mathbf{Q}^{(m)}} \right) \\ &\quad \times \bar{v}_{n_i, \mathbf{k}_i}^*(\mathbf{K}_a) \bar{v}_{n_f, \mathbf{k}_f}(\mathbf{K}_b) \\ &\quad \times \sum_{A, B} \bar{v}_{n_f, \mathbf{k}_f}^*(\mathbf{K}_B) \bar{v}_{n_i, \mathbf{k}_i}(\mathbf{K}_A) \delta_{\mathbf{K}_{ab}, \mathbf{K}_{AB}}, \end{aligned} \quad (5.21)$$

where the rectangular function is defined as

$$\text{rect}(t) = \begin{cases} 0, & \text{if } |t| > 1/2 \\ 1/2, & \text{if } |t| = 1/2 \\ 1, & \text{if } |t| < 1/2. \end{cases} \quad (5.22)$$

This value of S is assigned to all (\mathbf{Q}, ω) values that belong to the m -th bin. In this way, we have done away with the explicit implementation of delta functions in a pseudocontinuum by effectively averaging over any given bin m referring to the range $(\mathbf{Q}^{(m)} \pm \Delta\mathbf{Q}^{(m)}/2, \omega^{(m)} \pm \Delta\omega^{(m)}/2)$, to which a value of $S(\mathbf{Q}^{(m)}, \omega^{(m)})$ is assigned.

The binned grid for (\mathbf{Q}, ω) is practically constructed as follows. The energy- and momentum-conserving delta functions in Eq. (5.17) imply that for any given n_i, k_i, n_f , and k_f , the energy transfer is $\omega = E_{n_f, k_f} - E_{n_i, k_i}$ and given an additional a and b , the momentum transfer is $\mathbf{Q} = -(\mathbf{k}_{if} + \mathbf{K}_{ab})$. Therefore, we may extract the extent of the binned ω -grid by calculating

$$\begin{aligned} M(\omega) &\equiv \max(\omega) = \max(E_{n, \mathbf{k}}) - \min(E_{n, \mathbf{k}}) \\ m(\omega) &\equiv \min(\omega) = \min(E_{n, \mathbf{k}}) - \max(E_{n, \mathbf{k}}), \end{aligned} \quad (5.23)$$

and similarly, we may obtain the extent of the vector components of \mathbf{Q} , $M(Q_i)$ and $m(Q_i)$ for $i \in \{x, y, z\}$

$$\begin{aligned} M(Q_i) &\equiv \max(Q_i) = \max(k_i) - \min(k_i) + \max(K_i) - \min(K_i) \\ m(Q_i) &\equiv \min(Q_i) = \min(k_i) - \max(k_i) + \min(K_i) - \max(K_i). \end{aligned} \quad (5.24)$$

Knowing the extent of our (\mathbf{Q}, ω) -grid in each of its four dimensions, we subdivide each of these into N_{Qx} , N_{Qy} , N_{Qz} , and N_ω bins. We are free to choose this subdivision as we see fit. For instance, we can define linear grids with increments $\Delta(\mathbf{Q}, \omega) = (M(\mathbf{Q}, \omega) - m(\mathbf{Q}, \omega))/N(\mathbf{Q}, \omega)$, where all bins per dimension are of equal size. However, inspired by Fig. 3.1 for the DDCS at zero temperature, we anticipate that the contributions to the structure factor from small energy transfers ω will dominate. It will therefore be imperative to have a higher density of grid points near smaller values of ω . A similar behavior is expected for each of the vector components of \mathbf{Q} . Therefore, we will continue with the general assumption that each dimension has its own increment per bin m : $\Delta Q_x^{(m)}$, $\Delta Q_y^{(m)}$, $\Delta Q_z^{(m)}$, and $\Delta\omega^{(m)}$. As mentioned previously, this m -th bin corresponds to the range $(\mathbf{Q}^{(m)} \pm \Delta\mathbf{Q}^{(m)}/2, \omega^{(m)} \pm \Delta\omega^{(m)}/2)$, where $\Delta\mathbf{Q}^{(m)} = \Delta Q_x^{(m)} \Delta Q_y^{(m)} \Delta Q_z^{(m)}$.

Having access to all quantities needed for calculating $S(\mathbf{Q}, \omega)$ and having defined our binned coarse-grained (\mathbf{Q}, ω) -grid, we may proceed by calculating $S(\mathbf{Q}^{(m)}, \omega^{(m)})$, by looping over $n_i, k_i, n_f, k_f, a, b, A$ and B . In the inner-most loop we know which $\omega (= E_{n_f, k_f} - E_{n_i, k_i})$ and $\mathbf{Q} (= -\mathbf{k}_{if} - \mathbf{K}_{ab})$

we are considering, and therefore, to which bin the current contribution belongs to. That contribution is given explicitly by

$$A^{(m)} w(\mathbf{k}_i) w(\mathbf{k}_f) \bar{n}_{n_i, \mathbf{k}_i} (1 - \bar{n}_{n_f, \mathbf{k}_f}) \times \bar{v}_{n_i, \mathbf{k}_i}^*(\mathbf{K}_a) \bar{v}_{n_f, \mathbf{k}_f}(\mathbf{K}_b) \bar{v}_{n_f, \mathbf{k}_f}^*(\mathbf{K}_B) \bar{v}_{n_i, \mathbf{k}_i}(\mathbf{K}_A), \quad (5.25)$$

where $w(\mathbf{k})$ is $1/8$, $1/4$, $1/2$, 1 if \mathbf{k} is a corner, edge, boundary, or interior point of the first BZ, respectively, and

$$A^{(m)} = \frac{2}{(2\pi)^3} \frac{1}{\Delta^{(m)}} \Delta \mathbf{k}_i \Delta \mathbf{k}_f, \quad (5.26)$$

with $\Delta \mathbf{k}_i = \Delta \mathbf{k}_f$ being the increment of the \mathbf{k} -grid. The inclusion of the weights $w(\mathbf{k})$ accounts for the numerical integrations over \mathbf{k} , in this case using the trapezoidal method. The final result will be the structure factor from Eq. (5.21) on the coarse-grained (\mathbf{Q}, ω) -grid. However, similar to conventional solid-state calculations, this implementation has a high computational cost. In the following section we propose and discuss methods towards achieving realistic computations times for calculating the structure factor.

5.2.3 Optimization of the algorithm

Despite the previous section providing a relatively straightforward recipe for the calculation of the binned structure factor from Eq. (5.21), note that this calculation involves a heavily-nested loop structure of the following kind:

```

do ni = 1, N_hyb
  do nf = 1, N_hyb
    do ki = 1, N_k
      do kf = 1, N_k
        do a = 1, N_K
          do b = 1, N_K
            do A = 1, N_K
              do B = 1, N_K

```

where $N_{\text{hyb}} = N_{\mathbf{K}} + \sum_a N_C(a)$ was defined. This loop structure implies $N_{\mathbf{K}}^4 N_{\mathbf{k}}^2 N_{\text{hyb}}^2$ iterations. As a hands-on example, we will consistently use the example of the Al system, with the parameters used in Chapter 4 ($N_{\mathbf{K}} = 1647$, $N_{\mathbf{k}} = 7^3$, and $\sum_a N_C(a) = 20$) throughout this section. For this set of parameters, the loop structure amounts to $\sim 2.41 \times 10^{24}$ iterations. In order to relate the number of iterations to an estimate for the elapsed CPU time, the calculation of the structure factor with the aforementioned brute-force loop structure was implemented into XCRYSTAL. It was found that 1 second corresponds to $\sim 2.5 \times 10^8$ iterations. Therefore, the calculation of the structure factor for the Al system considered in Chapter 4 would take

$\sim 3 \times 10^8$ years. For practical purposes, this calculation must be refined and optimized extensively. To get the realistic computation time to the order of about a month or less, the number of iterations must be decreased by a factor of $\sim 10^9 - 10^{10}$.

The first thing we can do to reduce the computational effort is to use the restriction imposed by $\delta_{\mathbf{K}_{ab}, \mathbf{K}_{AB}}$ in Eq. (5.21) to our advantage. The reciprocal lattice vectors that satisfy this restriction will not change for different values of n_i , n_f , k_i and k_f and can therefore be precalculated. Going over the quadruple (a, b, A, B) loop and determining which vectors satisfy $\mathbf{K}_a - \mathbf{K}_b = \mathbf{K}_A - \mathbf{K}_B$ will result in $N_{abAB}^{(0)} \ll N_{\mathbf{K}}^4$ values of (a, b, A, B) that will yield a nonzero contribution to Eq. (5.21). The superscript (0) is introduced, because we can further reduce this number by making a few refinements. The first refinement, resulting in the number $N_{abAB}^{(1)} < N_{abAB}^{(0)}$, comes from the realization that if we know that $\mathbf{K}_a - \mathbf{K}_b = \mathbf{K}_A - \mathbf{K}_B$, then we also know that $\mathbf{K}_b - \mathbf{K}_a = \mathbf{K}_B - \mathbf{K}_A$, which therefore does not have to be explicitly considered in the loops. Naively, this would mean that $N_{abAB}^{(1)} \approx N_{abAB}^{(0)}/2$. However, this accounts for the cases $a = b = A = B$ twice. One could simply remove the overcounting by a few well-placed if-statements and continue working with $N_{abAB}^{(1)}$. However, an overuse of if-statements may be computationally costly, especially when placed in multiply-nested loops. Therefore, a further refinement can be made that remedies this overcounting without the use of if-statements. Define $N_{abAB} \equiv N_{abAB}^{(2)} < N_{abAB}^{(1)}$ by simply removing the contributions of $a = b = A = B$. The contributions for these cases may be added through a separate, double loop over $N_{\mathbf{K}}$. Thus, the quadruple loop over a , b , A , and B can be carried out by one loop over N_{abAB} and one double loop over $N_{\mathbf{K}}$. Explicitly, the loop structure involved in the determination of N_{abAB} takes on the form

```

do a = 1, N_K - 1
  do b = a + 1, N_K
    do A = 1, N_K - 1
      do B = A + 1, N_K

```

which takes $(\sum_{i=1}^{N_{\mathbf{K}}-1} (N_{\mathbf{K}}-i))^2 = (N_{\mathbf{K}}(N_{\mathbf{K}}-1)/2)^2$ iterations and the double loop over $N_{\mathbf{K}}$ is done as

```

do i = 1, N_K - 1
  do j = i + 1, N_K

```

where the contributions from $i = j$ and from $i = N_{\mathbf{K}}$ ($a = b = A = B = N_{\mathbf{K}}$) must be added explicitly after performing these loops, thus resulting in $N_{\mathbf{K}}(N_{\mathbf{K}}-1)/2 + N_{\mathbf{K}} = N_{\mathbf{K}}(N_{\mathbf{K}}+1)/2$ operations. This restricts the initial $N_{\mathbf{K}}^4 N_{\mathbf{k}}^2 N_{\text{hyb}}^2$ iterations to

$$\#iter = \frac{N_{\mathbf{K}}^2 (N_{\mathbf{K}} - 1)^2}{4} + \left(N_{abAB} + \frac{N_{\mathbf{K}}(N_{\mathbf{K}} + 1)}{2} \right) N_{\mathbf{k}}^2 N_{\text{hyb}}^2, \quad (5.27)$$

where the first term accounts for the precalculation of N_{abAB} . For the parameters used in Chapter 4, yielding $N_{abAB} = 360,614,455$, this scheme reduces the number of iterations by a factor of $\sim 20,000$, from $\sim 2.41 \times 10^{24}$ to $\sim 1.21 \times 10^{20}$, and the computation time from $\sim 3 \times 10^8$ years to $\sim 15,000$ years. Despite being a dramatic reduction, it is not enough for practical implementation.

The second way to reduce the time-costly loop structure of Eq. (5.21) is by removing redundant iterations in the loops over n_i , n_f , k_i and k_f . For practical purposes, it makes sense to alter the hierarchy of these loops such that the first two address initial states, and the latter two final states, i.e., n_i , k_i , n_f , and k_f . In the inner-most of these four loops, we have access to the quantities labeled by both (n_i, k_i) and (n_f, k_f) . However, we need not go over all possible values for (n, k) twice, for if we know the contribution from $\{I = (n_i, k_i); F = (n_f, k_f)\}$, we immediately have access to the contribution from $\{I = (n_f, k_f); F = (n_i, k_i)\}$. Additionally, we may skip the case when $n_i = n_f$ and $k_i = k_f$, as in this case there is no transition. Explicitly, this behavior is captured by the following loop structure

```

do I = 1, N_hyb * N_k
  if (I .eq. N_hyb * N_k) cycle
  ni = mod( I - 1, N_hyb ) + 1
  ki = ( I - ni ) / N_hyb + 1
  do J = I + 1, N_hyb * N_k
    nf = mod( J - 1, N_hyb ) + 1
    kf = ( J - nf ) / N_hyb + 1

```

and contains $N_{\text{hyb}}N_{\mathbf{k}}(N_{\text{hyb}}N_{\mathbf{k}} - 1)/2$ operations, thus only resulting in a decrease of a factor of 2. The number of iteration is nonetheless reduced to

$$\begin{aligned} \#iter = \frac{N_{\mathbf{K}}^2(N_{\mathbf{K}} - 1)^2}{4} + \left(N_{abAB} + \frac{N_{\mathbf{K}}(N_{\mathbf{K}} + 1)}{2} \right) \\ \times \frac{N_{\mathbf{k}}N_{\text{hyb}}(N_{\mathbf{k}}N_{\text{hyb}} - 1)}{2}. \end{aligned} \quad (5.28)$$

The third way to reduce the runtime of the calculation of Eq. (5.21) is by limiting ourselves only to electron-impact *ionization*. Thus far, Eq. (5.21) describes a transition occurring between an electron in a state (n_i, k_i) and an electron in a state (n_f, k_f) , e.g., excitation, or ionization. Limiting ourselves to ionization alone allows us to consider only those scenarios subject to the simple restriction $E_{n_i, \mathbf{k}_i} \leq \mu < E_{n_f, \mathbf{k}_f}$. The obvious drawback is, of course, the fact that we lose all information on, for instance, the process of excitation. Another complication is that the most efficient implementation of this restriction is incompatible with the previous runtime reduction of swapping $\{I = (n_i, k_i); F = (n_f, k_f)\}$ and $\{I = (n_f, k_f); F = (n_i, k_i)\}$ in the same loop. This is because it would be best to place the restrictions $E_{n_i, \mathbf{k}_i} \leq \mu$ and $\mu < E_{n_f, \mathbf{k}_f}$ separately in the (n_i, k_i) and the (n_f, k_f) loops,

respectively. So, if we choose to limit ourselves to ionization alone, we must omit the previous restriction, and regain a factor of two in the number of iterations. However, the second term in Eq. (5.27) would be multiplied by a factor of $\Delta E(1 - \Delta E)$, where ΔE is the amount of states that satisfy $E_{n_i, \mathbf{k}_i} \leq \mu$ divided by the total number of energy states. So

$$\begin{aligned} \#iter = \frac{N_{\mathbf{K}}^2(N_{\mathbf{K}} - 1)^2}{4} + \left(N_{abAB} + \frac{N_{\mathbf{K}}(N_{\mathbf{K}} + 1)}{2} \right) \\ \times N_{\mathbf{K}}^2 N_{\text{hyb}}^2 \Delta E(1 - \Delta E). \end{aligned} \quad (5.29)$$

As the temperature increases, ΔE will inevitably decrease as the chemical potential decreases and thermal excitations cause fewer electrons to be considered as bound. Therefore, ΔE will be largest at $T = 0$ eV. For the parameters used in Chapter 4, $\Delta E \sim 0.012$ at $T = 0$ eV, which brings the number of iterations down to $\sim 1.40 \times 10^{18}$, giving an estimated runtime of ~ 178 years, which is a factor of ~ 2000 shy from our goal of a computational time of 1 month.

Finally, the loop structure is perfectly compatible with the implementation of parallelization. For parallelization, the best case scenario exhibits a linear scaling between the runtime and the number of processors used. Having access to around 50 processors, we can reduce the runtime by another factor of ~ 50 , to the result of ~ 3.5 years. To obtain our aspired goal, another speed-up by another factor of ~ 40 would be needed. However, we would like to emphasize that the methods outlined in this section do result in a factor of $\sim 10^7$ in speed-up for the parameters used for Al from Chapter 4.

All methods outlined above are generally applicable. We may proceed with further optimization for specific cases. For example, if a system exhibits a high level of symmetry in its first Brillouin zone, we may exploit those symmetries to reduce the \mathbf{k} -grid needed in numerical integrations. Further optimization is a currently ongoing process and the author is confident the computation time for the structure factor can be brought well within reach of our aspired goal. Let us conclude with a discussion on the practical implementation of calculating the electron-impact ionization cross section using the binned structure factor.

5.2.4 Cross section

Recall that the DDCS is given in terms of the structure factor as

$$\frac{d^2\sigma}{d\Omega dE_{\text{out}}} = \frac{4}{|\mathbf{Q}|^4} \frac{q_{\text{out}}}{q_{\text{in}}} S(\mathbf{Q}, \omega), \quad (5.30)$$

from which the cross section can be obtained as [Eq. (2.103)]:

$$\sigma = \int dE_{\text{out}} \int_0^{2\pi} d\phi \int_{-1}^{+1} d(\cos \theta) \frac{d^2\sigma}{d\Omega dE_{\text{out}}}. \quad (5.31)$$

Recall also that in Chapter 3, we considered σ as a function of the incoming electron energy E_{in} and that there was no explicit dependence on the direction of \mathbf{Q} , as we were free to orient our reference system such that $\hat{\mathbf{Q}} = \hat{\mathbf{q}}_{\text{out}}$. In XCRYSTAL, we no longer have this freedom as we are working with a pre-determined \mathbf{k} -grid. Therefore, the cross section calculated by XCRYSTAL contains more information than the cross section calculated by XATOM, as directional dependencies of the cross section can be calculated and examined. However, in order to compare with the cross-section results obtained in Chapter 3, this directional dependence must be removed. To do so, the structure factor $S(\mathbf{Q}, \omega)$ will be averaged over the incoming directions, $\hat{\mathbf{q}}_{\text{in}}$.

The angular averaging is relatively straightforward. Starting with a chosen value of E_{in} , we start by defining an angular grid for $\mathbf{q}_{\text{in}} = (\sqrt{2E_{\text{in}}}, \theta_{\text{in}}, \phi_{\text{in}})$. Energy- and momentum-conservation impose that $E_{\text{out}} = E_{\text{in}} - \omega$, and $\mathbf{q}_{\text{out}} = \mathbf{q}_{\text{in}} - \mathbf{Q}$. Therefore, for every value in the $(\theta_{\text{in}}, \phi_{\text{in}})$ -grid, we can determine those values of \mathbf{Q} and ω on the binned grid that will provide a contribution to the cross section from the corresponding $S(\mathbf{Q}, \omega)$. Subsequently, a numerical averaging can be performed to obtain a value for the DDCCS as a function of E_{in} , E_{out} , and \mathbf{q}_{out} , which we may numerically integrate, as per Eq. (5.31) to obtain $\sigma(E_{\text{in}})$. Moreover, the calculation of $S(\mathbf{Q}, \omega)$ does not have to be repeated for a new value of E_{in} . Choosing a value for E_{in} , the binned (\mathbf{Q}, ω) -grid determines which energy- and momentum-transfers are available, and the calculation of $S(\mathbf{Q}, \omega)$ needs to be completed only once.

Chapter 6

Summary and outlook

In this dissertation, I have developed a new framework that allows for the calculation of the electron-impact ionization cross section in transient states of nonisothermal warm dense matter.

Electron-impact ionization

In Chapter 3, I calculated the doubly-differential cross section for electron-impact ionization of single ions at zero temperature from first principles, in a Hartree-Fock-Slater (HFS) framework. This expression was subsequently implemented in a computationally efficient way into the pre-existing simulation toolkit XATOM.

Applying this formula to a single C^{2+} ion, the observation was made that the electron-impact ionization favors small energy transfers between the incoming electron and the ejected electron, as well as small scattering angles for the incoming electron. From the doubly-differential cross section I subsequently calculated the singly-differential cross sections, both energy- and angle-resolved, as well as the total electron-impact ionization cross section. The expression for the latter was applied to the ions C^+ , C^{2+} , and S^{8+} . For the ground-state variations of these ions, where the holes find themselves in the outer-most electronic shells, a comparison could be made between these predictions for the cross section with experiments, as well as with the frequently used Lotz and BEB methods. The comparison with experiment revealed that the result calculated with XATOM adequately reproduced the trends observed in the cross section as a function of incoming electron energy. The calculated cross section was particularly accurate for high incoming energies, consistent with the description of the incoming electron as a plane wave. This approximation however led to an overestimate of the predicted cross section for lower incoming energies.

The ability of XATOM to specify an explicit electronic configuration for an ion of a given charge state allowed me to subsequently calculate the

electron-impact ionization cross section at different electronic configurations for the same ions C^+ , C^{2+} , and S^{8+} . These exotic electronic configurations are expected to be prevalent during the ultrafast interaction between samples and XFEL pulses. The dense electron environment in these experiments allows for the possibility of electron-impact ionization to occur before the exotic ion relaxes to the ground-state configuration. Therefore, the question arises whether or not the electronic configuration matters for the calculation of the electron-impact ionization cross section. It is found that this does indeed matter by comparing ground-state ion configurations to the configurations with holes in the inner-most shells. Specifically, the cross sections for the exotic ions were found to be larger than their ground-state counterparts, which becomes a less pronounced effect for higher incoming electron energies. The relative difference becomes more prevalent both for lower incoming energies as well as in the cases where the exotic ion and ground-state ion differ in configuration more significantly. The physical reasoning behind this observation was argued to lie in the fact that the contribution of the valence electrons to the electron-impact ionization cross section dominates, which could be justified by analyzing the derived theoretical formula. This effect is somewhat diminished due to an increased screening the electrons in the exotic ion undergo from the nucleus. Additionally, since everything was consistently calculated within the same framework of XATOM, the argument was made that the observed trends are accurate, even if the exact calculation for the cross section can be expected to be at most as good as the prediction for the ground-state ions. In view of this, the applicability of the frequently used, semi-empirical Lotz method was scrutinized for these exotic ions. The Lotz method did not provide a general trend with regards to the difference in cross sections for both kinds of ions, in part due to the absence of experimental data for exotic ions. Finally, it was concluded that the BEB method *did* contain some predictability in the calculation of the cross section for exotic ions, despite an absence of the explicit calculation of electronic structure, as it mimics the general trends predicted by XATOM, which was justified through an inspection of the BEB formula.

Warm dense matter

In Chapter 4, I have developed a novel theoretical framework that allows for the description of electrons present in a transient state of nonisothermal warm dense matter (WDM), which was implemented in a new toolkit called XCRYSTAL. This transient state of matter is expected to be present up to 100 fs after the irradiation of a solid sample by an XFEL, whereby the electrons are characterized by temperatures within the WDM regime, assumed to be in thermal equilibrium, and the ions form a cold static lattice. The purpose of XCRYSTAL was to explicitly provide the electronic wave functions and

energies in these systems, so that they could be used for the calculation of matrix elements, such as the one present in the expression for the electron-impact ionization cross section.

To exploit the periodicity of our system, the Bloch-wave formalism was employed, which conventionally calculates electronic wave functions in reciprocal (or \mathbf{k} -) space using plane waves as a basis. The drawback of this implementation is the necessity to use many contributions in \mathbf{k} -space in order to accurately describe localized atomic orbitals. There are numerous ways to remedy this complication, the most relevant for this work being the augmented plane-wave method. In this method, the system is modeled by spheres centered around nuclei in which real-space atomic wave functions are continuously matched to plane waves outside of the spheres. The method used in XCRYSTAL is inspired by the augmented plane-wave method. However, XCRYSTAL does away with the requirement for matching and assumes the electronic wave function to be a linear combination of plane waves and atomic orbitals *everywhere*, effectively employing a hybrid basis. Subsequently, the systems considered in this work were modeled using a muffin-tin potential, though this assumption is not a necessary restriction for XCRYSTAL, and the electronic structure was modeled using a HFS-framework, much like in XATOM. Emphasis must be put on the fact that XCRYSTAL allows for the atomic orbitals that have been added to this hybrid basis to be updated to the response of the delocalized electrons during the optimization of these wave functions. Note that the strategy whereby *all* electronic states of interest, be it occupied, bound, delocalized, or (pseudo)continuum states, are calculated through the diagonalization of the Hamiltonian is a key characteristic shared between the methodologies used in both XATOM and XCRYSTAL in this work.

To benchmark the framework of XCRYSTAL, Al at WDM conditions was considered, which could be compared to experiment. An accurate prediction of the K -threshold energy of Al at these conditions could be made using XCRYSTAL, and, in addition, predictions for the orbital-dependent ionization potential depression were provided. From comparing the results from XCRYSTAL with the average-atom model and the two-step HFS model, the conclusion was made that the explicit implementation of a crystallic structure did not have a large effect on the predicted results, and the most important contribution to the accuracy of predicted results was argued to come from the interwoven optimization of the atomic orbitals in the hybrid basis. In addition, I could justify the use of the average-atom method in this WDM-context, which had previously been thought to be insufficiently accurate for this regime, by providing a discussion on the definition of charge for systems that include delocalized electrons.

Finally, using the implementation of a crystal structure in XCRYSTAL, the first predictions for the electronic band structure as a function of temperature, for temperatures characteristic for the WDM regime, were provided.

As the temperature increased, the observation could be made that all energies were dragged down to more negative values, band gaps started to form, and bands were becoming less pronounced. This was justified by the intuitive explanation that at higher temperatures, the potential seen by the delocalized electrons becomes more attractive, as larger thermal excitations of core orbitals led to a reduced screening effect seen from the nucleus. The more attractive potential drags down the energies of the delocalized electrons, and gave them more of a localized nature. This, in turn, explains the formation of band gaps as these electrons start to exhibit atomic-like behavior.

Electron-impact ionization in WDM

In Chapter 5, I combined the theoretical expression for the doubly-differential cross section of electron-impact ionization from Chapter 3 with the ansatz employed for the wave function of the electron used in XCRYSTAL from Chapter 4. In this way, I derived the expression for the doubly-differential cross section of electron-impact ionization in the transient states of nonisothermal warm dense matter that were discussed in Chapter 4.

Despite the derivation being relatively straightforward, and the resulting expression being intuitively understandable, the computational implementation of this expression is anything but trivial, due to the complicated loop structure it requires. From the doubly-differential cross section, the structure factor was factored out, as it is where all the important physics, and also all the complications, reside. I presented an in-depth analysis on the practical implementation of the structure factor using a coarse-grained binned-grid method. An analysis is provided regarding the estimated CPU runtime for the calculation of the structure factor, and it is found that without extensive optimization, this time vastly exceeds the amount for practical applications. Therefore, several approaches are outlined which can improve the estimated runtime considerably. Further optimization, as well as the practical implementation, of the structure factor is an ongoing process

Outlook

Having the new toolkit XCRYSTAL at our disposal, there are many different avenues that may be considered to continue the work presented in this dissertation.

An obvious first step in the continuation of this work is to complete the optimization of the calculation of the structure factor $S(\mathbf{Q}, \omega)$, and to calculate the electron-impact ionization cross section in the states of WDM that were considered in this dissertation. An ab-initio prediction of this cross section as a function of temperature would be the first of its kind.

The calculation of the structure factor $S(\mathbf{Q}, \omega)$ will, however, not only have merit in the study of electron-impact ionization. The cross section for photoionization to first order is proportional to the same quantity $S(\mathbf{Q}, \omega)$. The prefactor of $(4/Q^4)$ (incidentally the expression for the Rutherford scattering cross section, i.e., elastic electron-electron scattering) in Eq. (5.2) is then replaced by the Thomson scattering (elastic photon-electron scattering) cross section, which is given in atomic units by (see Refs. [84, 101]) $\alpha^4 \sum_{\lambda_{\text{out}}} |\epsilon_{\mathbf{q}_{\text{out}}, \lambda_{\text{out}}}^* \cdot \epsilon_{\mathbf{q}_{\text{in}}, \lambda_{\text{in}}}|^2$. Here, $\epsilon_{\mathbf{q}, \lambda}$ are the polarization vectors of the photon with momentum \mathbf{q} , $\lambda \in \{1, 2\}$, and the photonic momenta $\mathbf{q}_{\text{in/out}}$ are related to the photonic frequencies $\omega_{\text{in/out}}$ by $\mathbf{q}_{\text{in/out}} = \hbar\omega_{\text{in/out}}$. In fact, the calculation of the photoionization cross section in WDM by using the structure factor $S(\mathbf{Q}, \omega)$ derived in chapter 5 is expected to be more accurate than the calculation of the electron-impact ionization cross section, because the structure factor was derived under the assumption that the incoming and outgoing projectile is modeled by a plane wave only. For electrons, this will only be a decent approximation if the initial electron has a high incoming energy and the energy transfer during scattering is rather small. For a photon, using plane waves in its description is much less of a restrictive approximation to make. In addition, considering solely the measurability of these cross sections in the context of XFEL experiments, the photoionization process is much more easy to distinguish. This is because the electrons will undergo various cascading events after an ionization. Therefore, even if an electron manages to escape the system in order to be measured, and if one can discern that this electron is the product of the specific event of impact ionization (as opposed to, e.g., Auger-Meitner decay), the energy of this electron is still expected to be too low in order to be described accurately as a plane wave. An ionizing photon will not suffer from this difficulty and will be much more easy to identify. The calculation of the structure factor $S(\mathbf{Q}, \omega)$ will therefore not only be applicable to the calculation of electron-impact ionization cross sections, but to the calculation of photoionization cross sections as well.

Furthermore, in this dissertation, only the effects of increasing the electronic temperature were considered on the electronic states. However, WDM is not only characterized by its temperature, but also by its density. It would therefore be interesting to simulate the trend the ionization potential depression would follow as the density is increased at a fixed temperature with XCRYSTAL, which may be compared to the results in Ref. [133], for instance. To incorporate a change in density, one would simply scale the lattice parameter that defines the unit cell. This option has already been implemented in XCRYSTAL, but has not yet been explored.

Finally, there is the possibility of not only considering one-electron energies, such as the ones that were shown in the band structure plots, but also total energies. By defining $E_{\text{tot}} = \sum_{n, \mathbf{k}} E_{n, \mathbf{k}} \bar{n}_{n, \mathbf{k}}$, where $E_{n, \mathbf{k}}$ and $\bar{n}_{n, \mathbf{k}}$ denote the energy and thermal occupation number of the orbital denoted by

the quantum numbers (n, \mathbf{k}) , we gain access to a zeroth-order calculation of the total energy as a function of temperature, which can immediately reveal information on the heat capacity of the system.

Acknowledgements

First and foremost, an immense amount of my sincerest gratitude must be expressed towards my supervisors Prof. Robin Santra and Prof. Beata Ziaja-Motyka. Obviously for the guidance they have provided with regards to the direction and ideas of my doctoral work, but also for simply for being there. For being available, and approachable. Time was always made for questions and uncertainties, and, more importantly, for answers and clarifications. Never has a discussion not been fruitful in one way or another.

Next I would like to appreciate Sang-Kil Son. Working with him has been one of the easiest aspects of my work during my time at CFEL, and I can honestly say it's just simply been a pleasure. I must also add that his input has been an invaluable aid in the construction of this thesis. Additionally, I would like to thank Ludger Inhester for his help regarding German translations.

I would like to thank Berit Heiser for making administrative work look easy, which I never imagined to be possible by anyone. Her patience and helpfulness is a not-to-be-underestimated part in the completion of any doctorate in the group.

I would like to thank Otfried Geffert and Zoltan Jurek for their ready availability regarding anything and everything related to computers, which was particularly useful for someone like me who started their doctoral work on simulations and code development, while being largely computer illiterate. Otfried told me in the beginning that coding is like swimming, in the sense that, it can be learned through careful practice, or by being chucked into the ocean, and just not drowning. Thanks to him and Zoltan, I didn't drown, and I feel I can comfortably swim now.

I would like to thank the "coffee people"; those who engaged in friendly discussion regarding all things scientific, and all things less so, over a cup of coffee after lunch. The regulars that spring to mind being Sang-Kil Son, Ludger Inhester, Caroline Arnold, Ralph Welsh, Otfried Geffert, Daria Kolbasova, Murali Krishna Ganesa Subramanian, Julia Schäfer, Koudai Toyota, Michael Obermeyer, Niels Breckwolt, and Benoît Richard. For some reason, the most recurring discussion I was a part of was the definition of, and distinctions between, a sandwich, a hamburger, and a hot dog. Ralph and I had staggeringly different opinions I recall, and we never did quite reach a consensus. Furthermore, a thank you goes out to all other people not previously mentioned from the CFEL Theory group.

At this point I have to single out Murali Krishna Ganesa Subramanian, Malik Muhammad Abdullah, Gourab Chatterjee, and Pedram Mehrabi. These are four names I can no longer read by themselves without thinking of them as part of a whole, and I wouldn't want it any other way.

I would like to thank my family—my sister, and mother and father—for being there for me.

Last, and certainly not least, I thank Rebecca Nyman for being my rock, my foundation, and everything I hold dear.

Bibliography

- [1] J.J. Beks, S.-K. Son, R. Santra, and B. Ziaja, *Ab initio calculation of electron-impact-ionization cross sections for ions in exotic electron configurations*, Phys. Rev. A **98**, 022701 (2018).
- [2] K. Mecseki, H. Höppner, M. Büscher, V. Tkachenko, N. Medvedev, J.J. Beks, V. Lipp, P. Piekarz, M. Windeler, J.W.G. Tisch, *et al.*, *Hard X-ray induced fast secondary electron cascading processes in solids*, Appl. Phys. Lett. **113**, 114102 (2018).
- [3] J.J. Beks, S.-K. Son, B. Ziaja, and R. Santra, *Electronic-structure calculations for nonisothermal warm dense matter*, Phys. Rev. Res. **2**, 033061 (2020).
- [4] B.W.J. McNeil and N.R. Thompson, *X-ray free-electron lasers*, Nat. Photon. **4**, 814–821 (2010).
- [5] C. Pellegrini, *X-ray free-electron lasers: from dreams to reality*, Phys. Scr. **T169**, 014004 (2016).
- [6] E.A. Seddon, J.A. Clarke, D.J. Dunning, C. Masciovecchio, C.J. Milne, F. Parmigiani, D. Rugg, J.C.H. Spence, N.R. Thompson, K. Ueda, *et al.*, *Short-wavelength free-electron laser sources and science: a review*, Rep. Prog. Phys. **80**, 115901 (2017).
- [7] C. Pellegrini, *The development of XFELs*, Nat. Rev. Phys. **2**, 330–331 (2020).
- [8] J.P. Marangos, *Accessing the quantum spatial and temporal scales with XFELs*, Nat. Rev. Phys. **2**, 332–334 (2020).
- [9] C. Pellegrini, A. Marinelli, and S. Reiche, *The physics of x-ray free-electron lasers*, Rev. Mod. Phys. **88**, 015006 (2016).
- [10] P. Emma, R. Akre, J. Arthur, R. Bionta, C. Bostedt, J. Bozek, A. Brachmann, P. Bucksbaum, R. Coffee, F.-J. Decker, *et al.*, *First lasing and operation of an ångström-wavelength free-electron laser*, Nat. Photon. **4**, 641 (2010).

- [11] T. Ishikawa, H. Aoyagi, T. Asaka, Y. Asano, N. Azumi, T. Bizen, H. Ego, K. Fukami, T. Fukui, Y. Furukawa, *et al.*, *A compact X-ray free-electron laser emitting in the sub-ångström region*, Nat. Photon. **6**, 540 (2012).
- [12] T. Tschentscher, C. Bressler, J. Grünert, A. Madsen, A.P. Mancuso, M. Meyer, A. Scherz, H. Sinn, and Ulf Zastrau, *Photon Beam Transport and Scientific Instruments at the European XFEL*, Appl. Sci. **7**, 592 (2017).
- [13] W. Decking, S. Abeghyan, P. Abramian, A. Abramsky, A. Aguirre, C. Albrecht, P. Alou, M. Altarelli, P. Altmann, K. Amyan, *et al.*, *A MHz-repetition-rate hard X-ray free-electron laser driven by a superconducting linear accelerator*, Nat. Photon. **14**, 391–397 (2020).
- [14] H.-S. Kang, C.-K. Min, H. Heo, C. Kim, H. Yang, G. Kim, I. Nam, S.Y. Baek, H.-J. Choi, G. Mun, *et al.*, *Hard X-ray free-electron laser with femtosecond-scale timing jitter*, Nat. Photon. **11**, 708 (2017).
- [15] C.J. Milne, T. Schietinger, M. Aiba, A. Alarcon, J. Alex, A. Anghel, V. Arsov, C. Beard, P. Beaud, S. Bettoni, *et al.*, *SwissFEL: The Swiss X-ray Free Electron Laser*, Appl. Sci. **7**, 720 (2017).
- [16] W. Ackermann, G. Asova, V. Ayvazyan, A. Azima, N. Baboi, J. Bähr, V. Balandin, B. Beutner, A. Brandt, A. Bolzmann, *et al.*, *Operation of a free-electron laser from the extreme ultraviolet to the water window*, Nat. Photon. **1**, 336 (2007).
- [17] L. Young, E.P. Kanter, B. Krässig, Y. Li, A.M. March, S.T. Pratt, R. Santra, S.H. Southworth, N. Rohringer, L.F. DiMauro, *et al.*, *Femtosecond electronic response of atoms to ultra-intense X-rays*, Nature (London) **466**, 56 (2010).
- [18] M. Hoener, L. Fang, O. Kornilov, O. Gessner, S.T. Pratt, M. Guhr, E.P. Kanter, C. Blaga, C. Bostedt, J.D. Bozek, *et al.*, *Ultraintense X-Ray Induced Ionization, Dissociation, and Frustrated Absorption in Molecular Nitrogen*, Phys. Rev. Lett. **104**, 253002 (2010).
- [19] B. Rudek, S.-K. Son, L. Foucar, S.W. Epp, B. Erk, R. Hartmann, M. Adolph, R. Andritschke, A. Aquila, N. Berrah, *et al.*, *Ultra-efficient ionization of heavy atoms by intense x-ray free-electron laser pulses*, Nat. Photon. **6**, 858 (2012).
- [20] A. Rudenko, L. Inhester, K. Hanasaki, X. Li, S.J. Robatjazi, B. Erk, R. Boll, K. Toyota, Y. Hao, O. Vendrell, *et al.*, *Femtosecond response of polyatomic molecules to ultra-intense hard x-rays*, Nature (London) **546**, 129 (2017).

- [21] R. Neutze, R. Wouts, D. van der Spoel, E. Weckert, and J. Hajdu, *Potential for biomolecular imaging with femtosecond x-ray pulses*, Nature (London) **406**, 752 (2000).
- [22] H.N. Chapman, P. Fromme, A. Barty, T.A. White, R.A. Kirian, A. Aquila, M.S. Hunter, J. Schulz, D.P. DePonte, U. Weierstall, *et al.*, *Femtosecond x-ray protein nanocrystallography*, Nature (London) **470**, 73 (2011).
- [23] M.M. Seibert, T. Ekeberg, F.R.N.C. Maia, M. Svenda, J. Andreasson, O. Jónsson, D. Odić, B. Iwan, A. Rocker, D. Westphal, *et al.*, *Single mimivirus particles intercepted and imaged with an x-ray laser*, Nature (London) **470**, 78 (2011).
- [24] S. Boutet, L. Lomb, G.J. Williams, T.R.M. Barends, A. Aquila, R.B. Doak, U. Weierstall, D.P. DePonte, J. Steinbrener, R.L. Shoeman, *et al.*, *High-resolution protein structure determination by serial femtosecond crystallography*, Science **337**, 362 (2012).
- [25] L. Redecke, K. Nass, D.P. DePonte, T.A. White, D. Rehders, A. Barty, F. Stellato, M. Liang, T.R.M. Barends, S. Boutet, *et al.*, *Natively inhibited Trypanosoma brucei cathepsin B structure determined by using an x-ray laser*, Science **339**, 227 (2013).
- [26] M. Malvestuto, A. Caretta, B. Casarin, R. Ciprian, M. Dell'Angela, S. Laterza, Y.-D. Chuang, W. Wurth, A. Revcolevschi, L.A. Wray, and F. Parmigiani, *Direct observation of spin-orbit-induced 3d hybridization via resonant inelastic extreme ultraviolet scattering on an edge-sharing cuprate*, Phys. Rev. B **99**, 115120 (2019).
- [27] G. Mercurio, I.A. Makhotkin, I. Milov, Y.Y. Kim, I.A. Zaluzhnyy, S. Dziarzhyski, L. Wenthaus, I.A. Vartanyants, and W. Wurth, *Surface structure determination by x-ray standing waves at a free-electron laser*, New J. Phys. **21**, 033031 (2019).
- [28] D. Kutnyakhov, R.P. Xian, M. Dendzik, M. Heber, F. Pressacco, S.Y. Agustsson, L. Wenthaus, H. Meyer, S. Gieschen, G. Mercurion, *et al.*, *Time- and momentum-resolved photoemission studies using time-of-flight momentum microscopy at a free-electron laser*, Rev. Sci. Instrum. **91**, 013109 (2020).
- [29] J.W. McIver, B. Schulte, F.-U. Stein, T. Matsuyama, G. Jotzu, G. Meier and A. Cavalleri, *Light-induced anomalous Hall effect in graphene*, Nat. Phys. **16**, 3841 (2020).
- [30] S. Bernitt, G.V. Brown, J.K. Rudolph, R. Steinbrügge, A. Graf, M. Leutenegger, S.W. Epp, S. Eberle, K. Kubiček, V. Mäkel, *et al.*,

An unexpectedly low oscillator strength as the origin of the Fe XVII emission problem, Nature (London) **492**, 225 (2012).

- [31] B.D. Patterson, *Crystallography using an x-ray free-electron laser*, Crystallogr. Rev. **20**, 242 (2014).
- [32] I. Schlichting, *Serial femtosecond crystallography: The first five years*, IUCrJ **2**, 246 (2015).
- [33] J.C.H. Spence, *XFELs for structure and dynamics in biology*, IUCrJ, **4**, 322–339 (2017).
- [34] S.M. Vinko, O. Ciricosta, B.I. Cho, K. Engelhorn, H.-K. Chung, C.R.D. Brown, T. Burian, J. Chalupský, R.W. Falcone, C. Graves, *et al.*, *Creation and diagnosis of a solid-density plasma with an x-ray free-electron laser*, Nature (London) **482**, 59 (2012).
- [35] S.H. Glenzer, L.B. Fletcher, E. Galtier, B. Nagler, R. Alonso-Mori, B. Barbrel, S.B. Brown and D.A. Chapman, and Z. Chen, C.B. Curry, *et al.*, *Matter under extreme conditions experiments at the Linac Coherent Light Source*, J. Phys. B: At. Mol. Opt. Phys. **49**, 092001 (2016).
- [36] R. Neutze, *Opportunities and challenges for time-resolved studies of protein structural dynamics at X-ray free-electron lasers*, Phil. Trans. R. Soc. B **369**, 20130318 (2014).
- [37] H.N. Chapman, C. Caleman, and N. Timneanu, *Diffraction before destruction*, Phil. Trans. R. Soc. B **369**, 20130313 (2014).
- [38] B. Ziaja, Z. Jurek, N. Medvedev, V. Saxena, S.-K. Son, and R. Santra, *Towards realistic simulations of macromolecules irradiated under the conditions of coherent diffraction imaging with an x-ray free-electron laser*, Photonics **2**, 256 (2015).
- [39] H.M. Quiney and K.A. Nugent, *Biomolecular imaging and electronic damage using x-ray free-electron lasers*, Nat. Phys. **7**, 142 (2011).
- [40] B. Ziaja, H.N. Chapman, R. Fäustlin, S. Hau-Riege, Z. Jurek, A.V. Martin, S. Toleikis, F. Wang, E. Weckert, and R. Santra, *Limitations of coherent diffractive imaging of single objects due to their damage by intense x-ray radiation*, New J. Phys. **14**, 115015 (2012).
- [41] U. Lorenz, N.M. Kabachnik, E. Weckert, and I.A. Vartanyants, *Impact of ultrafast electronic damage in single-particle x-ray imaging experiment*, Phys. Rev. E **86**, 051911 (2012).
- [42] M.M. Abdullah, Z. Jurek, S.-K. Son, and R. Santra, *Calculation of x-ray scattering patterns from nanocrystals at high x-ray intensity*, Struct. Dyn. **3**, 054101 (2016).

- [43] S.-K. Son, L. Young, and R. Santra, *Impact of hollow-atom formation on coherent x-ray scattering at high intensity*, Phys. Rev. A **83**, 033402 (2011).
- [44] I.-J. Kang and W.D. Foland, *Theory of electron impact excitation and ionization of atoms and ions*, Phys. Rev. **164**, 122 (1967).
- [45] M.R.H. Rudge, *Theory of the ionization of atoms by electron impact*, Rev. Mod. Phys. **40**, 564 (1968).
- [46] P.L. Bartlett and A.T. Stelbovics, *Calculation of electron-impact total-ionization cross sections*, Phys. Rev. A **66**, 012707 (2002).
- [47] J. Berakdara, A. Lahmam-Bennani, and C.D. Cappello, *The electron-impact double ionization of atoms: An insight into the four-body Coulomb scattering dynamics*, Phys. Rep. **2**, 91 (2003).
- [48] O. Al-Hagan, *Theoretical study of electron impact-ionization of molecules*, Doctoral Dissertation, Missouri University of Science and Technology, Rolla Missouri, 2010.
- [49] H. Erhardt, K. Jung, G. Knoth, and P. Schlemmer, *Differential cross sections of direct single electron impact ionization*, Z. Phys. D Atoms, Molecules and Clusters **1**, 3 (1985).
- [50] F. Graziani, M.P. Desjarlais, R. Redmer, and S.B. Trickey, editors, *Frontiers and Challenges in Warm Dense Matter*, Lecture Notes in Computational Science and Engineering, Vol. 96 (Springer, Cham, 2014).
- [51] R.J. Taylor, *The Stars: Their Structure and Evolution*, 2nd ed. (Cambridge University Press, Cambridge, 1994).
- [52] F.J. Rogers and C.A. Iglesias, *Astrophysical Opacity*, Science **263**, 50 (1994).
- [53] T. Guillot, *Interiors of Giant Planets Inside and Outside the Solar System*, Science **286**, 72 (1999).
- [54] G. Chabrier, *Plasma physics and planetary astrophysics*, Plasma Phys. Control. Fusion **51**, 124014 (2009).
- [55] R. Helled, J.D. Anderson, M. Podlak, and G. Schubert, *Interior Models of Uranus and Neptune*, Astrophys. J. **726** 15 (2011).
- [56] J. Lindl, *Development of the indirect-drive approach to inertial confinement fusion and the target physics basis for ignition and gain*, Phys. Plasmas **2**, 3933 (1995).

- [57] J.D. Lindl, P. Amendt, R.L. Berger, S.G. Glendinning, S.H. Glenzer, S.W. Haan, R.L. Kauffman, O.L. Landen, and L.J. Suter, *The physics basis for ignition using indirect-drive targets on the National Ignition Facility*, Phys. Plasmas **11**, 339 (2004).
- [58] S.X. Hu, B. Militzer, V.N. Goncharov, and S. Skupsky, *Strong Coupling and Degeneracy Effects in Inertial Confinement Fusion Implosions*, Phys. Rev. Lett. **104**, 235003 (2010).
- [59] S.H. Glenzer, B.J. MacGowan, P. Michel, N.B. Meezan, L.J. Suter, S.N. Dixit, J.L. Kline, G.A. Kyrala, D.K. Bradley, D.A. Callahan, *et al.*, *Symmetric Inertial Confinement Fusion Implosions at Ultra-High Laser Energies*, Science **327**, 1228 (2010).
- [60] R.W. Lee, S.J. Moon, H.-K. Chung, W. Rozmus, H.A. Baldis, G. Gregori, R.C. Cauble, O.L. Landen, J.S. Wark, A. Ng, *et al.*, *Finite temperature dense matter studies on next-generation light sources*, J. Opt. Soc. Am. B **20**, 770 (2003).
- [61] O. Ciricosta, S.M. Vinko, H.-K. Chung, B.-I. Cho, C.R.D. Brown, T. Burian, J. Chalupský, K. Engelhorn, R.W. Falcone, C. Graves, *et al.*, *Direct Measurements of the Ionization Potential Depression in a Dense Plasma*, Phys. Rev. Lett. **109**, 065002 (2012).
- [62] B.I. Cho, K. Engelhorn, S.M. Vinko, H.-K. Chung, O. Ciricosta, D.S. Rackstraw, R.W. Falcone, C.R.D. Brown, T. Burian, J. Chalupský, *et al.*, *Resonant $K\alpha$ Spectroscopy of Solid-Density Aluminum Plasmas*, Phys. Rev. Lett. **109**, 245003 (2012).
- [63] S.M. Vinko, V. Vozda, J. Andreasson, S. Bajt, J. Bielecki, T. Burian, J. Chalupsky, O. Ciricosta, M.P. Desjarlais, H. Fleckenstein, *et al.*, *Time-Resolved XUV Opacity Measurements of Warm Dense Aluminum*, Phys. Rev. Lett. **124**, 225002 (2020).
- [64] W.S. Fann, R. Storz, H.W.K. Tom, and J. Bokor, *Electron thermalization in gold*, Phys. Rev. B **46**, 13592 (1992).
- [65] W.S. Fann, R. Storz, H.W.K. Tom, and J. Bokor, *Direct measurement of nonequilibrium electron-energy distributions in subpicosecond laser-heated gold films*, Phys. Rev. Lett. **68**, 2834 (1992).
- [66] J. Hohlfeld, S.-S. Wellershoff, J. Güdde, U. Conrad, V. Jähnke, and E. Matthias, *Electron and lattice dynamics following optical excitation of metals*, Chem. Phys. **251**, 237 (2000).
- [67] M. Bonn, D.N. Denzler, S. Funk, M. Wolf, S.-S. Wellershoff, and J. Hohlfeld, *Ultrafast electron dynamics at metal surfaces: Competition*

- between electron-phonon coupling and hot-electron transport*, Phys. Rev. B **61**, 1101 (2000).
- [68] J. Hohlfeld, J. Müller, S.-S. Wellershoff, and E. Matthias, *Time-resolved thermorefectivity of thin gold films and its dependence on film thickness*, Appl. Phys. B. **64**, 387 (1997).
- [69] C. Suárez, W.E. Bron, and T. Juhasz, *Dynamics and Transport of Electronic Carriers in Thin Gold Films*, Phys. Rev. Lett. **75**, 4536 (1995).
- [70] T. Juhasz, H.E. Elsayed-Ali, G.O. Smith, C. Suárez, and W.E. Bron, *Direct measurements of the transport of nonequilibrium electrons in gold films with different crystal structures*, Phys. Rev. B **48**, 15488 (1993).
- [71] L. Susskind and G. Hrabovsky, *Classical Mechanics: The Theoretical Minimum*, (Penguin Group, Clays Ltd, St Ives, Great Britain 2014).
- [72] D.J. Griffiths, *Introduction to Quantum Mechanics*, (Pearson Education Inc., Upper Saddle River, New Jersey 07458, USA, 2005), 2nd Edition.
- [73] T. Lancaster and S.J. Blundell, *Quantum Field Theory for the Gifted Amateur*, (Oxford University Press, Oxford, UK, 2014), 1st Edition.
- [74] A. Szabo and N.S. Ostlund, *Modern Quantum Chemistry: Introduction to Advanced Electronic Structure Theory*, (Dover Publications, Dover, UK, 1996).
- [75] R. Santra, *Theory of Photon-Matter Interactions*, lecture notes, (66-382) Universität Hamburg, delivered October 2018-February 2019.
- [76] C. Kittel, *Introduction to Solid State Physics*, (Wiley, USA, 2005).
- [77] N.W. Ashcroft and N.D. Mermin, *Solid State Physics*, (Holt, Rinehart and Winston, New York, 1976).
- [78] B. Rupp, *Biomolecular Crystallography: Principles, Practice, and Application to Structural Biology* (Garland Science, New York, 2009).
- [79] Z. Jurek, S.-K. Son, B. Ziaja, and R. Santra, *xMDYN and xATOM: Versatile simulation tools for quantitative modeling of x-ray free-electron laser induced dynamics of matter*, J. Appl. Crystallogr. **49**, 1048 (2016).
- [80] B.F. Murphy, T. Osipov, Z. Jurek, L. Fang, S.-K. Son, M. Mucke, J.H.D. Eland, V. Zhaunerchyk, R. Feifel, L. Avaldi, *et al.*, *Femtosecond*

- x-ray-induced explosion of C_{60} at extreme intensity*, Nat. Commun. **5**, 4281 (2014).
- [81] T. Tachibana, Z. Jurek, H. Fukuzawa, K. Motomura, K. Nagaya, S. Wada, P. Johnsson, M. Siano, S. Mondal, Y. Ito, *et al.*, *Nanoplasma formation by high intensity hard x-rays*, Sci. Rep. **5**, 10977 (2015).
- [82] M.M. Abdullah, Anurag Z. Jurek, S. K. Son, and R. Santra, *Molecular-dynamics approach for studying the nonequilibrium behavior of x-ray-heated solid-density matter*, Phys. Rev. E **96**, 023205 (2017).
- [83] C.H. Yoon, M.V. Yurkov, E.A. Schneidmiller, L. Samoylova, A. Buzmakov, Z. Jurek, B. Ziaja, R. Santra, N.D. Loh, T. Tschentscher, *et al.*, *A comprehensive simulation framework for imaging single particles and biomolecules at the European x-ray free-electron laser*, Sci. Rep. **6**, 24791 (2016).
- [84] R. Santra, *Concepts in x-ray physics*, J. Phys. B: At. Mol. Opt. Phys. **42**, 023001 (2009).
- [85] R. Henderson, *Cryo-protection of protein crystals against radiation damage in electron and x-ray diffraction*, Proc. R. Soc. Lond. B **241**, 6 (1990).
- [86] R.F. Egerton, *Control of radiation damage in the TEM*, Ultramicroscopy **127**, 100 (2013).
- [87] S.M. Vinko, O. Ciricosta, T.R. Preston, D.S. Rackstraw, C.R.D. Brown, T. Burian, J. Chalupský, B.I. Cho, H.-K. Chung, K. Engelhorn, *et al.*, *Investigation of femtosecond collisional ionization rates in a solid-density aluminium plasma*, Nat. Commun. **6**, 6397 (2015).
- [88] W. Lotz, *Ionization potentials of atoms and ions from hydrogen to zinc*, J. Opt. Soc. Am. **57**, 873 (1967).
- [89] W. Lotz, *An empirical formula for the electron-impact ionization cross-section*, Z. Phys. **206**, 205 (1967).
- [90] W. Lotz, *Electron-impact ionization cross-sections and ionization rate coefficients for atoms and ions from hydrogen to calcium*, Z. Phys. **216**, 241 (1968).
- [91] W. Lotz, *Electron-impact ionization cross-sections for atoms up to $Z = 108$* , Z. Phys. **232**, 101 (1970).
- [92] Y.-K. Kim and M.E. Rudd, *Binary-encounter-dipole model for electron-impact ionization*, Phys. Rev. A **50**, 3954 (1994).

- [93] Y.-K. Kim, J.P. Santos, and F. Parente, *Extension of the binary-encounter-dipole model to relativistic incident electrons*, Phys. Rev. A **62**, 052710 (2000).
- [94] M. Guerra, F. Parente, P. Indelicato, and J.P. Santos, *Modified binary encounter Bethe model for electron-impact ionization*, Int. J. Mass Spectrom. **313**, 1 (2012).
- [95] S.-K. Son, J.J. Bekx, K. Toyota, O. Geffert, J.M. Slowik, and R. Santra, XATOM—*An Integrated Toolkit for X-Ray and Atomic Physics*, rev. 2885 CFEL, DESY, Hamburg, Germany, 2017.
- [96] J.M. Slowik, S.-K. Son, G. Dixit, Z. Jurek, and R. Santra, *Incoherent x-ray scattering in single molecule imaging*, New J. Phys. **16**, 073042 (2014).
- [97] S.-K. Son, O. Geffert, and R. Santra, *Compton spectra of atoms at high x-ray intensity*, J. Phys. B: At. Mol. Opt. Phys. **50**, 064003 (2017).
- [98] J.C. Slater, *A simplification of the Hartree-Fock method*, Phys. Rev. **81**, 385 (1951).
- [99] R. Latter, *Atomic energy levels for the Thomas-Fermi and Thomas-Fermi-Dirac potential*, Phys. Rev. **99**, 510 (1955).
- [100] G. Yao and S.I. Chu, *Generalized pseudospectral methods with mappings for bound and resonance state problems*, Chem. Phys. Lett. **204**, 381 (1993).
- [101] K. Sturm, *Dynamic structure factor: An introduction*, Z. Naturforsch. **48a**, 233-242 (1993).
- [102] J.W. Cooper, *Photoionization from outer atomic subshells, A model study*, Phys. Rev. **128**, 681 (1962).
- [103] R. Santra and L.S. Cederbaum, *Non-Hermitian electronic theory and applications to clusters*, Phys. Rep. **368**, 1 (2002).
- [104] P.W. Langhoff, in *Electron-Molecule and Photon-Molecule Collisions*, edited by T. Rescigno, V. McKoy, and B. Schneider (Plenum Press, New York, 1979).
- [105] Available at <https://physics.nist.gov/PhysRefData/Ionization/intro.html>
- [106] Z. Jurek, G. Faigel, and M. Tegze, *Dynamics in a cluster under the influence of intense femtosecond hard x-ray pulses*, Eur. Phys. J. D **29**, 217 (2004).

- [107] A. Burgess and M.C. Chidichimo, *Electron impact ionization of complex ions*, Mon. Not. R. Astr. Soc. **203**, 1269 (1983).
- [108] M.A. Lennon, K.L. Bell, H.B. Gilbody, J.G. Hughes, A.E. Kingston, M.J. Murray, and F.J. Smith, *Recommended data on the electron impact ionization of atoms and ions: Fluorine to Nickel*, J. Phys. Chem. Ref. Data **17**, 1285 (1988).
- [109] H. Suno and T. Kato, *Cross section database for carbon atoms and ions: Electron-impact ionization, excitation, and charge exchange in collisions with hydrogen atoms*, At. Data Nucl. Data Tables, **92** 407 (2006)
- [110] K.L. Aitken, M.F.A. Harrison, and R.D. Rundel, *Measurement of the cross section for electron impact ionization of multi-electron ions, II. N^{2+} to N^{3+} and C^+ to C^{2+}* , J. Phys. B: At. Mol. Phys. **4**, 1189 (1971).
- [111] P.R. Woodruff, M.-C. Hublet, M.F.A. Harrison, and E. Brook, *A measurement of the cross section for electron impact ionisation of C^{2+}* , J. Phys. B: At. Mol. Phys. **11**, L679 (1978).
- [112] E.I. Moses, R.N. Boyd, B.A. Remington, C.J. Keane, and R. Al-Ayat, *The National Ignition Facility: Ushering in a New Age for High Energy Density Science*, Phys. Plasmas **16**, 041006 (2009).
- [113] D.J. Hoarty, P. Allan, S.F. James, C.R.D. Brown, L.M.R. Hobbs, M.P. Hill, J.W.O. Harris, J. Morton, M.G. Brookes, R. Shepherd, *et al.*, *Observations of the Effect of Ionization-Potential Depression in Hot Dense Plasma*, Phys. Rev. Lett. **110**, 265003 (2013).
- [114] D.J. Hoarty, P. Allan, S.F. James, C.R.D. Brown, L.M.R. Hobbs, M.P. Hill, J.W.O. Harris, J. Morton, M.G. Brookes, R. Shepherd, *et al.*, *The First Data from the Orion Laser: Measurements of the Spectrum of Hot, Dense Aluminium*, High Energy Density Phys. **9**, 661 (2013).
- [115] G. Ecker and W. Kröll, *Lowering of the Ionization Energy for a Plasma in Thermodynamic Equilibrium*, Phys. Fluids **6**, 62 (1963).
- [116] J.C. Stewart and K.D. Pyatt, Jr., *Lowering of Ionization Potentials in Plasmas*, Astrophys. J. **144**, 1203 (1966).
- [117] S. Sahoo, G.F. Gribakin, G. Shabbir Naz, J. Kohanoff, and D. Riley, *Compton Scatter Profiles for Warm Dense Matter*, Phys. Rev. E **77**, 046402 (2008).
- [118] R. Piron and T. Blenski, *Variational-average-atom-in-quantum-plasmas (VAAQP) code and virial theorem: Equation-of-state and shock-Hugoniot calculations for warm dense Al, Fe, Cu, and Pb*, Phys. Rev. E **83**, 026403 (2011).

- [119] C.E. Starrett and D. Saumon, *Electronic and ionic structures of warm and hot dense matter*, Phys. Rev. E **87**, 013104 (2013).
- [120] W.R. Johnson and J. Nilsen, *Average-atom treatment of relaxation time in x-ray Thomson scattering from warm dense matter*, Phys. Rev. E **93**, 033205 (2016).
- [121] S.-K. Son, R. Thiele, Z. Jurek, B. Ziaja, and R. Santra, *Quantum-Mechanical Calculation of Ionization-Potential Lowering in Dense Plasma*, Phys. Rev. X **4**, 031004 (2014).
- [122] V. Recoules, J. Cl  rouin, G. Z  rah, P.M. Anglade, and S. Mazevet, *Effect of Intense Laser Irradiation on the Lattice Stability of Semiconductors and Metals*, Phys. Rev. Lett. **96**, 055503 (2006).
- [123] N.S. Grigoryan, E.S. Zijlstra, and M.E. Garcia, *Electronic origin of bond softening and hardening in femtosecond-laser-excited magnesium*, New J. Phys. **16**, 013002 (2014).
- [124] A. Pribram-Jones, S. Pittalis, E.K.U. Gross, and K. Burke, *Thermal Density Functional Theory in Context* in *Frontiers and Challenges in Warm Dense Matter*, Lecture Notes in Computational Science and Engineering, Vol. 96, edited by F. Graziani, M.P. Desjarlais, R. Redmer, and S.B. Trickey (Springer, Cham, 2014) pp. 25-60, DOI: 10.1007/978-3-319-04912-0_2.
- [125] L. Collins, I. Kwon, J. Kress, N. Troullier, and D. Lynch, *Quantum molecular dynamics simulations of hot, dense hydrogen*, Phys. Rev. E **52**, 6202 (1995).
- [126] J.G. Cl  rouin and S. Bernard, *Dense hydrogen plasma: Comparison between models*, Phys. Rev. E **56**, 3534 (1997).
- [127] L.A. Collins, S.R. Bickham, J.D. Kress, S. Mazevet, T.J. Lenosky, N.J. Troullier, and W. Windl, *Dynamical and optical properties of warm dense hydrogen*, Phys. Rev. B **63**, 184110 (2001).
- [128] M.P. Desjarlais, *Density-functional calculations of the liquid deuterium Hugoniot, reshock, and reverberation timing*, Phys. Rev. B **68**, 064204 (2003).
- [129] B. Holst, R. Redmer, and M.P. Desjarlais, *Thermophysical properties of warm dense hydrogen using quantum molecular dynamics simulations*, Phys. Rev. B **77**, 184201 (2008).
- [130] V. Recoules, F. Lambert, A. Decoster, B. Canaud, and J. Cl  rouin, *Ab Initio Determination of Thermal Conductivity of Dense Hydrogen Plasmas*, Phys. Rev. Lett. **102**, 075002 (2009).

- [131] S.M. Vinko, O. Ciricosta, and J.S. Wark, *Density functional theory calculations of continuum lowering in strongly coupled plasmas*, Nat. Commun. **5**, 3533 (2014).
- [132] B. Holst, V. Recoules, S. Mazevet, M. Torrent, A. Ng, Z. Chen, S.E. Kirkwood, V. Sametoglu, M. Reid, and Y.Y. Tsui, *Ab initio model of optical properties of two-temperature warm dense matter*, Phys. Rev. B **90**, 035121 (2014).
- [133] S.X. Hu, *Continuum Lowering and Fermi-Surface Rising in Strongly Coupled and Degenerate Plasmas*, Phys. Rev. Lett. **119**, 065001 (2017).
- [134] A.D. Baczewski, L. Shulenburger, M.P. Desjarlais, S.B. Hansen, and R.J. Magyar, *X-ray Thomson Scattering in Warm Dense Matter without the Chihara Decomposition*, Phys. Rev. Lett. **116**, 115004 (2016).
- [135] M. Bonitz, *Quantum Kinetic Theory*, 2nd ed. (Springer International Publishing, Cham, 2016).
- [136] K. Balzer and M. Bonitz, *Nonequilibrium Green's Functions Approach to Inhomogeneous Systems* (Springer-Verlag Berlin Heidelberg, 2013).
- [137] T. Dornheim, S. Groth, F.D. Malone, T. Schoof, T. Sjostrom, W.M.C. Foulkes, and M. Bonitz, *Ab initio quantum Monte Carlo simulation of the warm dense electron gas*, Phys. Plasmas **24**, 056303 (2017).
- [138] T. Dornheim, S. Groth, and M. Bonitz, *The uniform electron gas at warm dense matter conditions*, Phys. Rep. **744**, 1 (2018).
- [139] M. Bonitz, T. Dornheim, Zh.A. Moldabekov, S. Zhang, P. Hamann, A. Filinov, K. Ramakrishna, and J. Vorberger, *Ab initio simulation of warm dense matter*, arXiv:1912.09884 (2019).
- [140] R.R. Fäustlin, Th. Bornath, T. Döppner, S. Düsterer, E. Förster, C. Fortmann, S.H. Glenzer, S. Göde, G. Gregori, R. Irsig, *et al.*, *Observation of Ultrafast Nonequilibrium Collective Dynamics in Warm Dense Hydrogen*, Phys. Rev. Lett. **104**, 125002 (2010).
- [141] C. Kittel, *Introduction to Solid State Physics*, 8th ed. (Wiley, New York, 2004) 8th edition.
- [142] T.R. Preston, S.M. Vinko, O. Ciricosta, H.-K. Chung, R.W. Lee, and J.S. Wark, *The Effects of Ionization Potential Depression on the Spectra Emitted by Hot Dense Aluminium Plasmas*, High Energy Density Phys. **9**, 258 (2013).
- [143] P.B. Allen and V. Heine, *Theory of the temperature dependence of electronic band structures*, J. Phys. C **9**, 2305 (1976).

- [144] S.G. Titova, A.V. Lukoyanov, S.V. Pryanichnikov, L.A. Cherepanova, and A.N. Titov, *Crystal and electronic structure of high temperature superconducting compound $Y_{1-x}Ca_xBa_2Cu_3O_y$ in the temperature interval 80-300 K*, J. Alloys Compd. **658**, 891 (2016).
- [145] G.H. Wannier, *The Structure of Electronic Excitation Levels in Insulating Crystals*, Phys. Rev. **52**, 191 (1937).
- [146] G.H. Wannier, *Dynamics of Band Electrons in Electric and Magnetic Fields*, Rev. Mod. Phys. **34**, 645 (1962).
- [147] N. Marzari, A.A. Mostofi, J.R. Yates, I. Souza, and D. Vanderbilt, *Maximally localized Wannier functions: Theory and applications*, Rev. Mod. Phys. **84**, 1419 (2012).
- [148] W.E. Pickett, *Pseudopotential methods in condensed matter applications*, Comput. Phys. Rep. **9**, 115 (1989).
- [149] K. Lejaeghere, G. Bihlmayer, T. Bjorkman, P. Blaha, S. Blugel, V. Blum, D. Caliste, I.E. Castelli, S.J. Clark, A. Dal Corso, *et al.*, *Reproducibility in density functional theory calculations of solids*, Science **351**, 6280 (2016).
- [150] J.C. Slater, *Wave Functions in a Periodic Potential*, Phys. Rev. **51**, 846 (1937).
- [151] J.C. Slater, *An Augmented Plane Wave Method for the Periodic Potential Problem*, Phys. Rev. **92**, 603 (1953).
- [152] D.J. Singh and L. Nordstrom, *Planewaves, Pseudopotentials, and the LAPW Method*, 2nd ed. (Springer, New York, 2006).
- [153] C.C.J. Roothaan, *New Developments in Molecular Orbital Theory*, Rev. Mod. Phys. **23**, 69 (1951).
- [154] G.G. Hall, *The Molecular Orbital Theory of Chemical Valency VIII. A Method of Calculating Ionization Potentials*, Proc. R. Soc. Lond. A **205**, 541 (1951).
- [155] T. Blenski and K. Ishikawa, *Pressure Ionization in the Spherical Ion-Cell Model of Dense Plasmas and a Pressure Formula in the Relativistic Pauli Approximation*, Phys. Rev. E **51**, 4869 (1995).
- [156] W.R. Johnson, C. Guet, and G.F. Bertsch, *Optical Properties of Plasmas Based on an Average-Atom Model*, J. Quant. Spectrosc. Radiat. Transfer **99**, 327 (2006).
- [157] W.R. Johnson, J. Nilsen, and K.T. Cheng, *Thomson Scattering in the Average-Atom Approximation*, Phys. Rev. E **86**, 036410 (2012).

- [158] N.D. Mermin, *Stability of the Thermal Hartree-Fock Approximation*, Ann. Phys. (N.Y.) **21**, 99 (1963).
- [159] B. Segall, *Energy Bands of Aluminum*, Phys. Rev. **124**, 1797 (1961).
- [160] R.M. Martin, *Electronic Structure: Basic Theory and Practical Methods*, (Cambridge University Press, Cambridge, 2004).
- [161] A.C. Thompson and D. Vaughan, *X-Ray Data Booklet*, Center for X-Ray Optics and Advanced Light Source (Lawrence Berkeley National Laboratory, Berkeley, CA, 2001), <http://xdb.lbl.gov/>.
- [162] Y. Hao, L. Inhester, K. Hanasaki, S.-K. Son, and R. Santra, *Efficient electronic structure calculation for molecular ionization dynamics at high x-ray intensity*, Struct. Dyn. **2**, 041707 (2015).
- [163] L. Inhester, K. Hanasaki, Y. Hao, S.-K. Son, and R. Santra, *X-ray multiphoton ionization dynamics of a water molecule irradiated by an x-ray free-electron laser pulse*, Phys. Rev. A **94**, 023422 (2016).
- [164] D. Lai, *Matter in strong magnetic fields*, Rev. Mod. Phys. **73**, 629 (2001).